Department
Chemie und Pharmazie

FAU
FRIEDRICH-
ALEXANDER
UNIVERSITÄT
NATURWISSENSCHAFTLICHE
FAKULTÄT

Investigation of organometallic precursors for electron-/ion-induced processing in UHV

Untersuchung von metallorganischen Precursors für Elektronen-/Ionen-induzierte Prozessierung im UHV

Der Naturwissenschaftlichen Fakultät der
Friedrich-Alexander-Universität Erlangen-Nürnberg

zur Erlangung des Doktorgrades Dr. rer. nat.

vorgelegt von

Elif Bilgilisoy

Izmir, Turkey

Als Dissertation genehmigt von der Naturwissenschaftlichen Fakultät
der Friedrich-Alexander-Universität Erlangen-Nürnberg

Tag der mündlichen Prüfung: 07.11.2022

Vorsitzender des Promotionsorgans: Prof. Dr. Wolfgang Achtziger
Gutachter: PD. Dr. Hubertus Marbach
Prof. Dr. Jörg Libuda

Table of Contents

1 Introduction ... 1

2 Experimental Techniques and Fundamentals ... 5

2.1 Experimental Techniques ... 5

2.1.1 Scanning Electron Microscopy (SEM) ... 5

2.1.2 Auger Electron Spectroscopy (AES) ... 7

2.1.3 X-ray Photoelectron Spectroscopy (XPS) ... 10

2.1.4 Quadrupole Mass Spectrometry (QMS) ... 11

2.1.5 Atomic Force Microscopy (AFM) ... 11

2.1.6 Argon Sputter Gun ... 12

2.1.7 Electron Flood Gun ... 12

2.2 Instrumentation ... 13

2.2.1 UHV FEBIP Instrument ... 13

2.2.2 UHV Surface Science Instrument ... 14

2.3 Samples and Precursors ... 15

2.3.1 Substrates ... 15

2.3.2 $Fe(CO)_5$ ... 16

2.3.3 $Ru(CO)_4I_2$ ... 17

2.3.4 $(CH_3)AuP(CH_3)_3$ ... 18

2.4 Lithographic Parameters ... 19

2.5 Fundamentals ... 20

2.5.1 Electron Beam Induced Deposition (EBID/FEBID) ... 20

2.5.2 Electron Beam Induced Etching (EBIE/FEBIE) ... 23

2.5.3 Electron Beam Induced Interactions ... 25

2.5.4 Ion Beam Induced Interactions ... 27

3 Results ... 29

3.1 Surface Reactions of Low-Energy Argon Ions with $Ru(CO)_4I_2$ Precursors [P1] 29

3.2 Low Energy Electron- and Ion-Induced Reactions of $Fe(CO)_5$ [P2] 35

3.3 Nanoscale Ruthenium-Containing Deposits from $Ru(CO)_4I_2$ via Simultaneous Focused Electron Beam-Induced Deposition and Etching in Ultrahigh Vacuum: Mask Repair in Extreme Ultraviolet Lithography and Beyond [P3] 41

3.4 On the electron-induced reactions of $(CH_3)AuP(CH_3)_3$: A combined UHV surface science and gas-phase study [P4] 48

4 Summary 52

5 Zusammenfassung 55

6 Literature 58

7 Abbreviations 70

8 Acknowledgement 72

9 Appendix 74

9.1 Publications [P1] – [P4] 78

9.1.1 Publication [P1] 80

9.1.2 Publication [P2] 101

9.1.3 Publication [P3] 125

9.1.4 Publication [P4] 144

Published Papers

[P1] **Surface Reactions of Low-Energy Argon Ions with Organometallic Precursors**

E. Bilgilisoy, R. M. Thorman, J. C. Yu, T. B. Dunn, H. Marbach, L. McElwee-White, D. H. Fairbrother

J. Phys. Chem. C, **2020,** *124*, 24795-24808

The author´s contribution is the performance and interpretation of the MS and XPS experiments with $Ru(CO)_4I_2$, and $Co(CO)_3NO$ precursors. The experiments were performed together with Dr. Rachel M. Thorman during a four-month research stay at Johns Hopkins University. The manuscript was prepared in close cooperation by the author, Dr. Rachel M. Thorman, and Prof. Dr. Howard Fairbrother.

[P2] **Low Energy Electron- and Ion-Induced Reactions of $Fe(CO)_5$**

E. Bilgilisoy, R. M. Thorman, M. S. Barclay, H. Marbach, D. H. Fairbrother

J. Phys. Chem. C, **2021,** *125*, 17749-17760

The author´s contribution is the performance and interpretation of the MS and XPS experiments. The experiments were performed together with Dr. Rachel M. Thorman during a four-month research stay at Johns Hopkins University. The manuscript was prepared in close cooperation by the author and Prof. Dr. Howard Fairbrother.

[P3] **Nanoscale Ruthenium-Containing Deposits from $Ru(CO)_4I_2$ via Simultaneous Focused Electron Beam-Induced Deposition and Etching in Ultrahigh Vacuum: Mask Repair in Extreme Ultraviolet Lithography and Beyond**

E. Bilgilisoy, J. C. Yu, C. Preischl, L. McElwee-White, H.P. Steinrück, H. Marbach

ACS Appl. Nano Mater., **2022**, *5*, 3855-3865

The author´s contribution is the performance and interpretation of the EBID, AES, and AFM experiments. The manuscript was prepared by the author.

[P4] **On the Electron-Induced Reactions of $(CH_3)AuP(CH_3)_3$: A Combined UHV Surface Science and Gas-Phase Study**

A. Kamali*, E. Bilgilisoy*, A. Wolfram, T. Gentner, G. Ballmann, S. Harder, H. Marbach, O. Ingólfsson

Nanomaterials, **2022**, *12*, 2727

The author´s contribution is the performance and interpretation of the EBID, MS, and AES experiments. The manuscript was prepared equally by the author and Ali Kamali.

1 Introduction

The idea of nanotechnology arose with the talk given by Richard P. Feynman,[1] entitled "there is plenty of room at the bottom" where he addressed how to create and manipulate small-scaled structures and impose them on our daily life. Since then, with the significant impact of the development of different microscopy techniques (i.e., improvement in the scanning electron microscopy (SEM),[2, 3] invention of scanning tunneling microscopy (STM[4]), nanotechnology has offered a wide range of applications from engineering to medicine such as nano-sensors,[5, 6] solar cells,[7] nanojunctions,[8] nanomedicine,[9] or nanofood.[10] Nanostructures of varying dimensions (0D-3D), sizes (1-100 nm), and shapes with unique properties are determined by different fabrication ways.[11]

Lithography is one of the well-known methods for fabrication of nanostructures. The fundamental concept behind conventional lithography is transferring the designed pattern from a mask onto a sample surface. The process of conventional lithography involves several steps on a bulk substrate:[12] coating the resist material (e.g.: a light-, or electron-sensitive polymer) on the surface, developing the pattern from the mask to the resist material by exposing the resist to the energy source (i.e.: light, electron, or ion), and revealing the positive or negative resist image using a solvent (developer). Lithography is mainly used in the fields of integrated circuits[13, 14] and micro-/nano-electronic devices.[15, 16] The photomasks used in traditional lithography are generally produced by a maskless lithography technique, that is Electron Beam Lithography (EBL).[17] In EBL, nano-scaled structures are created on the substrate surface coated with electron-sensitive resist material using the focused electron beam of a SEM.[18] Although structures created with this technique are expected to be in sub 10 nm scaled size due to the relatively short wavelength of the accelerated electrons,[19, 20] the interaction between the resist material and the accelerated electrons leads to the proximity effect.[21-23] In addition, it should be noted that after EBL, the substrate needs to be exposed to a chemical substance to remove the resist material from the surface.[18] Thus, EBL requires several production steps, which makes the process complicated, and is significantly restricted with 2D structures.[24]

In particular, application fields such as light-emitting-diodes,[25, 26] Li-ion batteries,[27] or supercapacitors[28] demand flexibility in the dimension, size, and form of nanostructures. This required flexibility can be achieved using alternative fabrication techniques, for instance; chemical vapor deposition (CVD) (i.e., graphene,[29] nanotubes,[30] or aligned nano-walls/wires[31]), self-

assembly (i.e., self-assembled monolayers[32]), or molecular beam epitaxy (MBE) (i.e., heterostructured quantum dots; CdSe/ZnSe/GaAs, or CdTe/ZnTe/GaAs,[33] or nanowires[34]). Though these exemplary techniques aim to deposit/grow the material on the substrate surface with size and dimensionality control, they cannot meet the need for a localized deposition with a precise position and shape control on planar or non-planar surfaces. In this regard, focused charged beam-induced deposition is gaining more and more importance as it enables deposition by a direct writing approach using tightly focused charged particle beams to form localized nanostructures on flat or non-flat surfaces, avoiding the use of masks or resists.[35, 36] Depending on the type of used charged particles (electrons or ions), the focused charged beam-induced deposition is known as focused electron beam-induced deposition (FEBID) or focused ion beam-induced deposition (FIBID).[35-38] In FEBID and FIBID, typically, an organometallic precursor is injected using a gas-injection/inlet system (GIS) in close vicinity to the substrate surface into a high vacuum (HV) or ultra-high vacuum (UHV) chamber, where interactions between the charged particles and adsorbed precursor lead to decomposition of the molecule. While non-volatile fragments of the precursor create a deposit, the volatile fragments ideally desorb from the surface. It has been shown in the literature that it is possible to fabricate a wide range of nanostructures such as magnetic nanowires,[39, 40] nanodots,[41] or nanoarchitectures[42-44] using FEBID and FIBID.

The major drawback for FEBID and FIBID applications is that unwanted organic impurities are always present in the deposited nanostructures. There are two primary reasons for this bottleneck. One of them might be the precursor molecules used in both FEBID and FIBID. In conventional CVD, metalorganic precursors have been widely used and are designed to be activated by high temperatures (thermally driven).[45] The metalorganic precursors designed for CVD also have been mostly preferred in FEBID and FIBID.[36, 46] However, the difference between the decomposition pathways of synthesized metalorganic precursors considering the thermal-induced dissociation with the presence of co-reactive gases in CVD and electron-/ion-induced dissociation in FEBID/FIBID should not be ignored.[47-49] The low metal content in the deposits can be explained by the selected precursors that are actually unsuitable for FEBID/FIBID, where they display incomplete decomposition and/or desorption. The second reason for the low metallic content in FEBID/FIBID deposits arises from the lack of understanding of the fundamentals of each technique. Although the basic working principles of these two approaches appear quite similar, the molecular level mechanisms may be quite different considering the differences in the

interactions of electrons and ions with surfaces and precursor molecules.[36, 40, 50] The underlying mechanism of FEBID, which has been widely studied, can be defined by an electron-induced decomposition reaction, which results in partial ligand loss, and is followed by further ligand loss or ligand decomposition reactions.[36, 38, 51-55] In contrast to FEBID, to the best of our knowledge, fewer studies have focused on understanding the molecular-level events that contribute to deposition in FIBID.[56, 57] In order to overcome or minimize the side effect of low metallic content in FEBID/FIBID, either new improved organometallic precursors need to be designed and synthesized or a deeper understanding of the fundamentals of both techniques is required, which allows for optimizing the process parameters.

In this context, this thesis aims to identify and compare the sequence of bond-breaking steps that accompany ion- and electron-induced reactions with different physisorbed precursors, and to test the new precursors for UHV compatible FEBID device. The experimental and fundamental aspects of the techniques used in this thesis will be introduced in Chapter 2.

In the first and second parts of the results section (Chapters 3.1 and 3.2), the reactions triggered by low-energetic argon ions (860 and 1200 eV) and electrons (500 eV) with different thin adsorbed organometallic precursors on a cooled Au substrate are investigated using X-ray photoelectron spectroscopy (XPS) and mass spectrometry (MS) under UHV conditions. The results gathered for $Ru(CO)_4I_2$, which will be presented in Chapter 3.1, are also compared with a kinetic model developed to quantify the sequential reaction steps and reaction rates. In Chapter 3.2, in order to extend the knowledge obtained from Chapter 3.1, *in situ* XPS is used to compare the 500 eV electron- and 1200 eV Ar^+-induced reactions with adsorbed $Fe(CO)_5$ thin films.

In the third and fourth chapters of the result section, two promising organometallic precursors ($Ru(CO)_4I_2$ and $(CH_3)AuP(CH_3)_3$), which have never been tested in the UHV-based FEBID devices before, are analyzed for the deposition experiments using SEM, MS, and Auger electron spectroscopy (AES). In Chapter 3.3, the competing etching and deposition processes with $Ru(CO)_4I_2$, rather than the solely intended deposition, are observed step by step by combining the complementary techniques; AES and atomic force microscopy (AFM). Finally, Chapter 3.4 compares the FEBID results with the results from a gas phase study performed by our collaborative partners in order to find a fundamental electron-induced reaction mechanism for the $(CH_3)AuP(CH_3)_3$ precursor.

2 Experimental Techniques and Fundamentals

2.1 Experimental Techniques

The thesis at hand was conducted as a part of Horizon 2020; Marie Sklodowska-Curie Action (MSCA) Innovative Training Network (ITN) project named as "Low energy **ELE**ctron driven chemistry for the advantage of emerging **NA**no- fabrication methods (ELENA)". Due to the highly interactive and collaborative nature of MSCA-ITN research projects, several studies were performed by the author in different laboratories in Europe and the USA. Therefore, the sections below clearly state which device or which material is used in which laboratory and for what purpose.

2.1.1 Scanning Electron Microscopy (SEM)

Scanning electron microscopy (SEM) uses a highly focused electron beam that scans over the materials surface and generates secondary and backscattered electrons to form a corresponding image at high magnification, resulting in high resolution micrographs. The resolution limit or critical dimension (CD) of the examined sample is fundamentally limited by the wavelength (λ) of the signal source. The limit can be easily understood with the Abbe equation (Abbe limit), $d = \frac{\lambda}{2(NA)}$,[58] where NA is the numerical aperture (n.sinα) of the lens, and d is the resolution. Light microscopes mostly use tungsten/halogen bulbs as a light source, in the wavelength range of 400 – 800 nm. Therefore, according to the Abbe equation, the smallest structures around 200 nm can be observed with light microscopy. To overcome this resolution limit, one might use different sources with smaller wavelengths, such as X-rays or electrons. The resolution limit of electron microscopes can be estimated by using the de Broglie equation, $\lambda = \frac{h}{m_e v}$, where h is Planck's constant, m_e is the mass of an electron, and v is the velocity of the electron. The velocity can be obtained from the kinetic energy, $E(eV) = \frac{1}{2} m_e v^2 \rightarrow v = \sqrt{2(E(eV))/m_e}$ for non-relativistic particles. After substitution the corresponding wavelength relation into the Abbe equation, one obtains the resolution limit for electrons; $d = \frac{h}{2NA\sqrt{2(m_e)eV}}$. Theoretically, considering that the NA is around 1.4 and using a 15 keV electron beam, the fundamental resolution limit with the

corresponding electrons is ~ 0.004 nm. Thus, SEM is a high potential technique with the capability of providing images of high resolution with a great depth of field.

The electrons scattered off the sample surface are classified into two different scattering types: elastic and inelastic scattering. Elastic scattering occurs between the atomic nuclei and includes minimal energy exchange (almost negligible). Backscattered electrons (BSEs) are generated from the elastic collision between PEs and the specimen, and thus the kinetic energy of BSEs are very close to those of PEs. However, inelastic scattering causes a loss of energy, and the generation of secondary electrons (SEs).The kinetic energies of SEs in the range below 50 eV. Consequently, they have a low escape depth and thus are highly surface sensitive.

As depicted in Figure 1, the cross-section of SEs strongly relies on the kinetic energy of the PEs, and the atomic number of the specimen. The escape depth of scattered electrons according to the interaction of PEs with the sample defines the interaction volume. The dependence of the cross-section of emitted electrons on the kinetic energy and the atomic number determines the size of the interaction volume. Smaller interaction volumes can be observed for lower energy of PEs and higher atomic numbers of the specimen. Besides SEs and BSEs, the signal from the interaction volume also includes Auger electrons (AEs) and emitted X-ray (including characteristic X-rays and X-ray continuum). The detection of Auger electrons and X-ray emissions with particular energy-resolving detectors (i.e., energy dispersive (EDX) spectrometer for X-rays, or hemispherical energy analyzer for Auger electrons) enables to gain insight into surface properties like the chemical composition of a sample; notably, Auger electrons are more surface sensitive than X-rays.

In this dissertation, a highly focused electron beam from an electron microscope was used not only to obtain SEM images as a characterization tool but also to dissociate the volatile ligands of organometallic precursors and thus to write FEBIP structures.

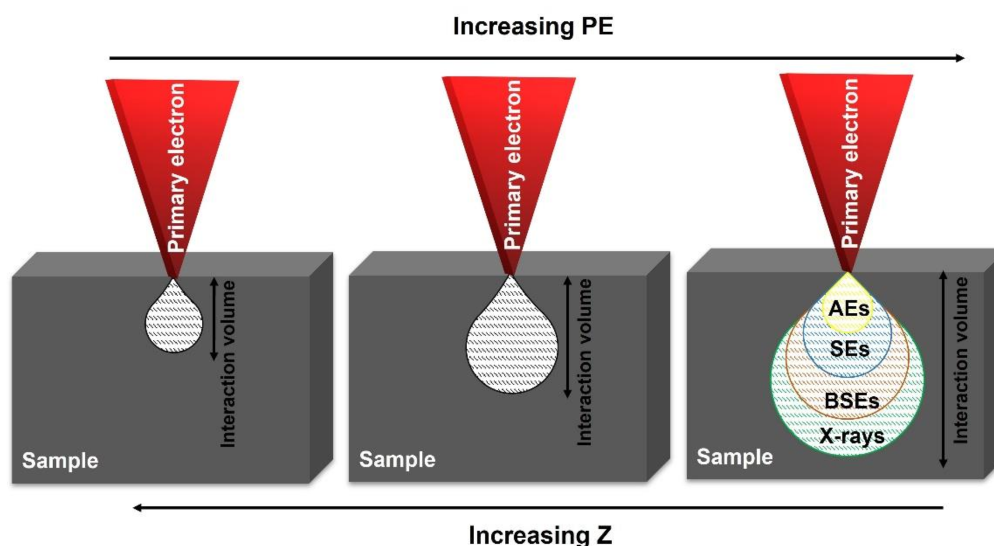

Figure 1. *Scheme showing the change in interaction volume according to the energy of primary electron (PE) and atomic number (Z) of substrate as well as the escape depths of SEs, BSEs, AEs, and X-rays.*

2.1.2 Auger Electron Spectroscopy (AES)

When studying the photoemission process, it was discovered that in addition to photoelectrons also, Auger electrons are emitted at discrete energy levels. Soon, it was realized Auger electrons could be used as a practical spectroscopic tool for the analysis of surfaces. Today, AES is a standard surface-sensitive analysis technique with the bombardment of high-energy electrons on a surface to obtain compositional and thickness information.

The kinetic energy of the impinging beam should be high enough to eject a core-level electron. Thus, electron beams with high energy values (> 3 keV) are applied. As depicted in Figure 2, the process of AES starts after the ejection of an inner shell electron; another electron from an outer shell level fills the vacancy left behind by the ejected one. Thereby, the energy difference between the involved levels is then released, e.g., by the ejection of a third electron, called the Auger electron. The corresponding Auger transition is labeled by the name of the level for the first core hole, followed by the names of all involved levels in terms of decreasing binding energies. Thus, the Auger transition in Figure 2 is labeled as $KL_1L_{2,3}$.

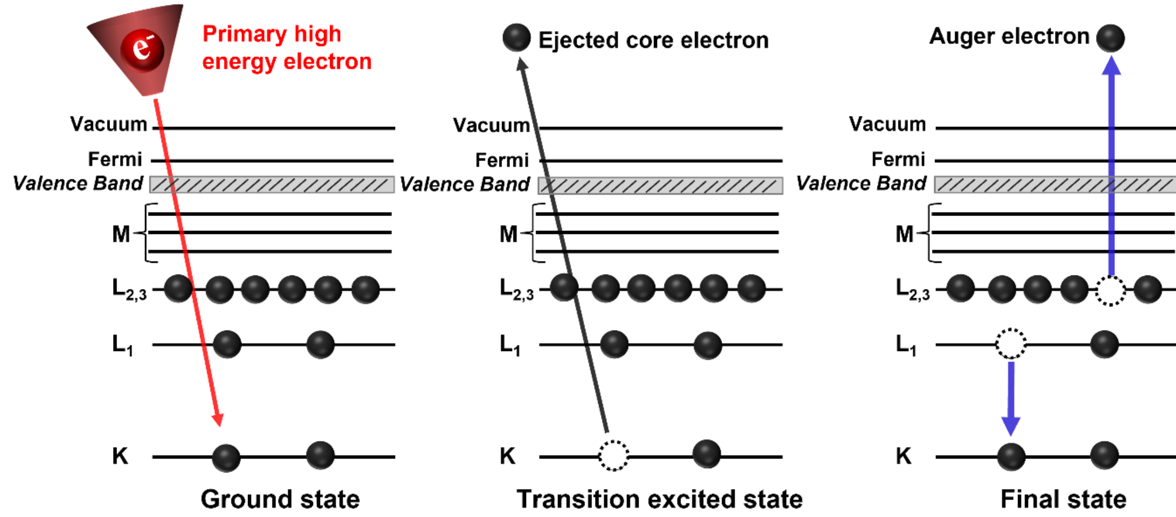

Figure 2. *Schematic representation of AES transition process (adapted from[59])*

The kinetic energy of Auger electron ($E_{KL_1L_{2,3}}$) is defined with the following equation:

$$E_{KL_1L_{2,3}} = E_K - E_{L1} - E^*_{L2,3} - \varphi_M \tag{1}$$

where E_K is the binding energy of the first core hole, E_{L1} is the binding energy of the electron, which fills the hole, $E^*_{L2,3}$ is the binding energy of the emitted electron, and to account for the relaxation process, and φ_M is the work function of the material ($\varphi_M = E_{vacuum} - E_{Fermi}$).[59]

The ejected electrons might experience inelastic scattering on their way to the surface of the sample. Elastically scattered electrons are neglected as they have a minimal contribution to the intensities of the detected signals. Therefore, ejected electrons originate from a position close enough to the surface of the sample, so that they can reach the energy analyzer before losing energy because of inelastic collisions. The probing depth depends on the attenuation length (λ_{AL}), which accounts for the probability of inelastic scattering of electrons in the substrate. The value of λ_{AL} can be calculated[60] in [nm] as:

$$\lambda_{AL} = 0.316a^{3/2}\left\{\frac{E}{Z^{0.45}[ln\,(E/27)+3]} + 4\right\} \tag{2}$$

where a is the lattice parameter of the deposit, E is the peak energy of the damped peak, and Z the atomic number of the deposit.

The value obtained from λ_{AL} for a specified element can later be used to calculate the thickness of the deposit on top of a substrate by using the damping of the Auger electron signal from the substrate.[60]

$$I_s = I_s^{\infty} exp\left[-\frac{d}{\lambda_{AL}(E_s)\cos\theta}\right] \quad (3)$$

In the above equation, I_s is the intensity of the damped signal from the substrate after deposition, I_s^{∞} is the intensity of the clean substrate, d is the thickness of the deposit, $\lambda_{AL}(E_s)$ is the inelastic mean free path of electrons of the energy E_s for the deposited layer, and θ is the angle of emission relative to the surface normal. In this thesis, the emission angle θ is always 35°.

As the energies of each orbital are quantized and elemental specific, the AES can also be used to determine the elemental composition of the substrate material.[61]

$$C_x = \left(\frac{I_x}{S_x d_x}\right) / \sum_i \left(\frac{I_i}{S_i d_i}\right) \quad (4)$$

For the equation of elemental composition, C_x is the atomic concentration of element X, I is the peak area, S is the sensitivity factor of the specific element, and d is the scale factor. In this thesis, peak areas are compared within one spectrum. Therefore, the scale factor 'd' is the same for one spectrum, and it is thus neglected.

AES analyses were performed using the beam parameters of 15 keV and 3 nA for all results presented in this thesis to characterize the chemical compound of FEBIP structures, due to the high kinetic energy, the attenuation of the primary electrons by the deposits can be neglected (λ_{AL} = 22 nm). Furthermore, it is worth noting that our AES setup allows for directly measuring I(E) (I: intensity, E: kinetic energy) with a reasonable signal-to-noise ratio and energy resolution, similar to X-ray photoelectron spectroscopy, which allows for separating overlapping peaks by peak fitting.

2.1.3 X-ray Photoelectron Spectroscopy (XPS)

X-ray photoelectron spectroscopy (XPS) or electron spectroscopy for chemical analysis (ESCA) is a quantitative technique for analyzing surface chemistry. The XPS technique is based on the photoelectric effect, which causes the emission of electrons from the surface upon exposure to electromagnetic radiation.[62] The photoemission process is sketched in Figure 3, and can be divided in three main steps: 1) a surface is irradiated by a known photon energy (monochromatic) X-ray source; 2) as a result of irradiation, core level electrons are emitted from the surface; 3) the emitted photoelectrons are collected and characterized by an electron energy analyzer. The emitted photoelectrons have specific binding energies based on the elements in the penetrating volume. If the electrons are close enough to the sample surface, they can be collected by the analyzer, and characteristic information such as the elemental composition of the surface, thickness of the top layer, and binding states of the elements can be detected. To obtain spectroscopic data, preferably monochromatic X-ray sources are used. Widely used X-ray sources are Mg Kα X-rays (hν: 1253.6 nm) and Al Kα X-rays (hν: 1486.6 nm). The electron analyzer measures the intensities of ejected photoelectrons versus their kinetic energy. To acquire the value of binding energy, the modified photoelectric effect equation considering the conservation of energy ($BE = h\nu - KE - \varphi, \varphi\text{: work function}$) can be used.[62] XPS is a very surface-sensitive method (~ 10 nm) as the ejected electrons from deeper surface layers cannot reach the detector as they lose their energies due to the inelastic collisions, given the generally very small inelastic mean free path (IMFP) of electrons.

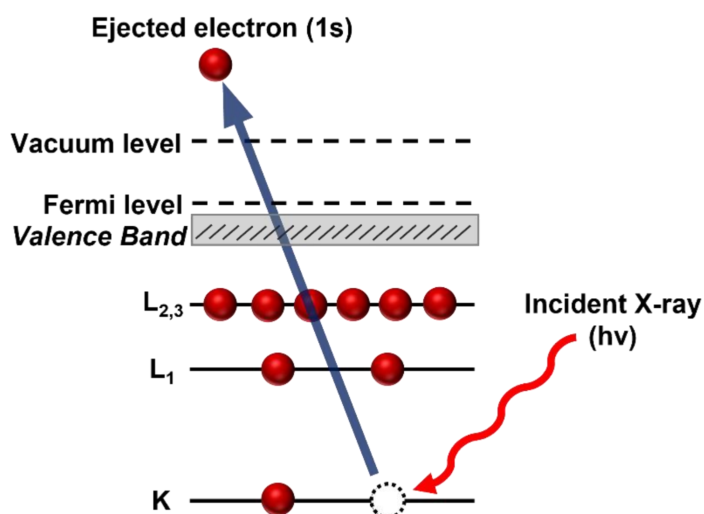

Figure 3. *Schematic illustration of XPS photoemission process.*

To calculate the thickness of the overlayer on the substrate from XPS based on Beer's Law, the following equation is used:

$$d = ln\left(\frac{I}{I_0}\right) \times \lambda \times cos\theta \qquad (5)$$

where d is thickness, I is the area of XPS peak with the adsorbate on the surface, I_0 is the XPS peak area of the substrate without any adsorbate (clean surface), λ is the IMFP of the electrons, and θ is the emission angle between the substrate surface normal and the energy analyzer. In this thesis, the XPS tool was used to elucidate and analyze the dissociation behavior of various adsorbate precursors initiated by the interaction of low energetic electrons and argon ions.

2.1.4 Quadrupole Mass Spectrometry (QMS)

In this thesis, a quadrupole mass spectrometer (QMS) was used to analyze the quality/purity of applied precursors, the residual gas compounds in the chambers, and the reaction products of adsorbed precursors upon the bombardment with low energetic electrons and argon ions in combination with XPS. A QMS includes four parallel rods, alternatingly (+) and (-) molecules. Superimposing direct current (DC) voltage is applied to the oppositely charged rods with radiofrequency (RF) voltage and thus separation of ions according to their mass-to-charge (*m/z*) ratios.[63] The specific *m/z* ratio oscillates through the filter and reaches the ion detector, where the remaining *m/z* values are inconsistent and hence reflected.[64] Finally, the filtered *m/z* signals are generated and screened by the amplifier in a mass spectrum.

2.1.5 Atomic Force Microscopy (AFM)

Atomic force microscopy (AFM) is an imaging technique based on the interaction forces that occur between a very sharp tip attached at the free end of a small cantilever and a substrate.[65] When the cantilever gets too close to the sample surface, an interaction occurs between the atoms on the surface and the tip, e.g., due to the van der Waals forces.[66] The corresponding interaction yields a bending or shift on the cantilever. For simplicity, only the detection of the cantilever bending by means of a laser combined with a position-sensitive photodetector is discussed. Thus, the laser source focuses on the cantilever and is reflected onto the photodetector. A change of the cantilever

position leads to a change in the reflected laser signal on the photodetector. Thereby the photodetector translates the information coming from the cantilever into electrical signals and transfers these signals to the feedback system or uses them directly (contact mode). There is a variety of different modes for AFM measurements, e.g.: contact mode, noncontact mode, and tapping (intermittent contact / semi-contact) mode.[67] In this thesis, noncontact AFM was used to obtain complementary information such as 2D AFM images, height profiles, and 3D AFM images on the FEBIP processes. It is important to note that in the latter mode, the measured topography is very accurate.

2.1.6 Argon Sputter Gun

A commercially available argon (Ar^+) sputter gun was used for substrate sputtering as well as to observe low energetic ion beam stimulated desorption of adsorbed precursor molecules in the laboratory of Prof. Howard Fairbrother at JHU. Ion bombardment was performed using a Perkin-Elmer PHI model 04-303 ion sputter gun with a primary argon beam energy of 880 V, and a substrate bias of +20 V, yielding a total beam energy of 860 V. The ion beam was located at approximately 45° relative to the surface normal. Along the surface normal, a beam energy was calculated around 600 V. The primary ion current density for the experiments performed on $Ru(CO)_4I_2$ was calculated to be ~ 40 nA/cm^2.[68]

2.1.7 Electron Flood Gun

A commercial electron flood gun (Specs 15/40) was used as a part of UHV-surface science experiments in the laboratory of Prof. Howard Fairbrother at JHU. The energy range of the flood gun source could be changed from 0 to 500 eV. However, in the surface science experiments, the energy value used from the electron source was set to 480 eV. A positive bias voltage with a value of +20 V was also applied to the surface to attract the secondary electrons during the experiment. In this case, the total energy that affected the surface throughout the experiments was ensured as 500 eV. Before starting the broad electron irradiation, the flood gun was always degassed. The sample position was changed during electron irradiation, so that the electron beam was incident along the surface normal, and a uniform electron flux was confirmed using a Faraday cup.[54, 69] For all surface science experiments, the unit of electron irradiation was given in mC/cm^2.

2.2 Instrumentation

2.2.1 UHV FEBIP Instrument

The device at the University of Erlangen-Nürnberg (FAU) for testing novel precursor molecules and producing nano-scaled deposits is a commercial UHV system (Multiscanlab, Omicron Nanotechnology, Germany) consisting of two main chambers (Analysis and Preparation chambers), and two small supplementary chambers for precursor gas handling and analysis (gas dosing chamber), and for fast sample loading (fast entry lock). Samples can be transferred between preparation, analysis, and rapid entry lock chambers using linear transfer arms and a series of gate valves (Figure 4).

The analysis chamber with a base pressure of $p < 2 \times 10^{-10}$ mbar is equipped with an UHV compatible electron column (Leo Gemini) for scanning electron microscopy (SmartSEM/Zeiss, nominal resolution < 3 nm) and for the fabrication of nano-scaled structures using the FEBIP approaches. The best resolution can be obtained with 15 keV accelerating voltage and 400 pA applied current. Thus, these parameters (15 keV, 400 pA) were used for SEM imaging. Furthermore, the highly focused electron beam combined with a hemispherical electron energy analyzer (EA 125, Omicron Nanotechnology, NanoSAM) offers the possibility of obtaining spectroscopic information from the surface via Auger electron spectroscopy and scanning Auger microscopy (SAM). Prior to the FEBIP experiments, the precursors are introduced into the analysis chamber via leak valves. Thereby the precursor gases are supplied through stainless-steel tubing with an inner diameter (capillary) of about 3 mm outside and inside the chamber till a distance substrate surface of around 12 mm. Precursor gas quality can be recorded using a QMS (Pfeiffer / Prisma QMS 200M). Considering the molecular flow, simulations from the Monte Carlo-based approach (GIS Simulator) have provided insight into the effective local vapor pressure at the sample surface level.[70] It was found to be 30 times higher due to the background pressure in the chamber for highly volatile precursors. Therefore, the background pressure of 3.0×10^{-7} mbar yields a local pressure of ~ 9.0×10^{-6} mbar at the sample surface. A more detailed explanation of the UHV system can be found in the doctoral thesis of Thomas Lukasczyk.[71]

The sputter gun (Omicron Nanotechnology/ISE10) in the preparation chamber (base pressure ~10^{-9} mbar) is used to clean the various sample surfaces such as SiO_x (nat.)/Si(111) or SiO_2 (200 nm)/Si(111) which were used as substrates for FEBIP experiments.

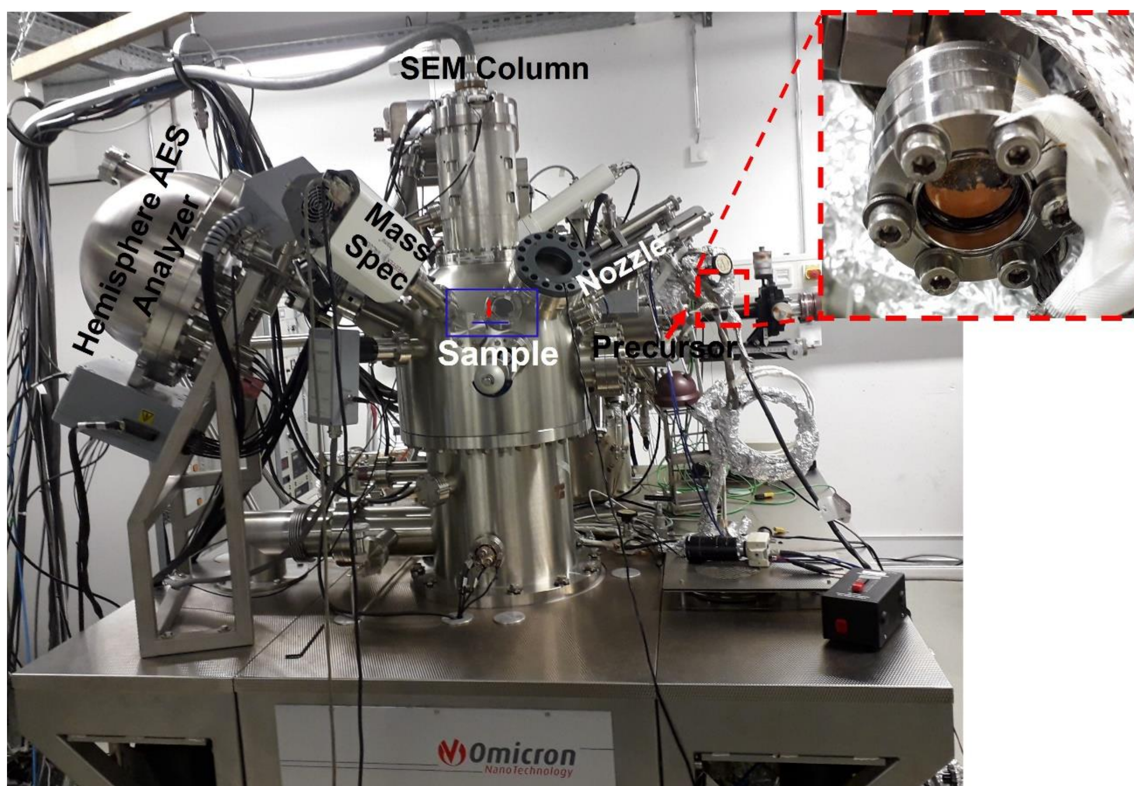

Figure 4. *The main chamber used in this thesis for FEBIP, SEM, AES, and QMS at FAU.*

2.2.2 UHV Surface Science Instrument

Specific UHV surface science experiments were conducted under the supervision of Prof. Howard Fairbrother in Johns Hopkins University-USA within the framework of the ELENA-ITN Project. The UHV surface science system includes one chamber equipped with XPS (PHI 5400), QMS (Balzers Prisma QMS200), electron gun (Specs FG 15/40), and sputter gun (Perkin-Elmer PHI 04-303). The chamber is pumped with a combination of turbomolecular, rotary, and ion-getter pumps to keep the base pressure of the system in the range of 10^{-9} mbar (Figure 5). Before experiments, precursors are attached to the system via leak valves. During and after purging the compounds, the purity of the attached chemicals is checked with QMS. As the surface quality is crucial for surface science experiments, the surface of the inserted substrate is sputtered by a sputter gun setting the parameters to 4 kV and 20 mA under 20 mPa of Ar^+ gas. The analysis tools mentioned above require specific sample positioning. The manipulator can rotate and move the sample in *X*, *Y*, *Z*,

and θ directions. The manipulator has one arm consisting of two copper rods holding a tantalum foil. Increasing the sample temperature is possible using resistive heating of the tantalum foil. The tantalum foil was sandwiched between metal blocks and substrate, and it is electrically connected to the two copper rods, which makes the current flow possible from the copper rods to the tantalum foil (depicted as red-colored dashed square in Figure 5). For the cooling of the substrate, a flow of liquid nitrogen (LN_2) through the copper rods was used. During heating or cooling, the substrate temperature can be directly measured by using K-type thermocouples.

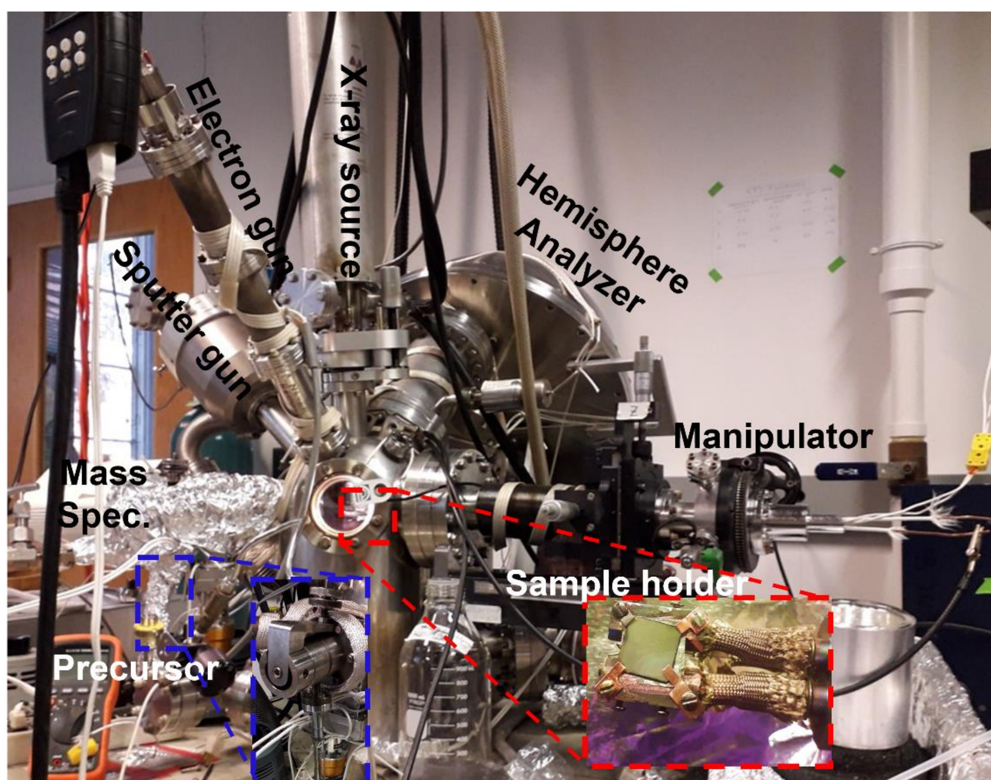

Figure 5. *The device used in this thesis for XPS, MS, electron, and ion irradiations at JHU.*

2.3 Samples and Precursors

2.3.1 Substrates

The choice of suitable substrates is vital in the UHV-surface science and UHV-FEBIP experiments performed in this thesis. A polycrystalline gold (Au) substrate was used during the surface science experiments performed at JHU due to the ease of cleaning with sputtering cycles and lack of spectral overlapping with the desired elemental spectra.

FEBIP experiments carried out at FAU were performed on a commercially available SiO_2 (200 nm) / Si(111) and sputtered clean Si(111) substrates for testing of different precursor molecules. Considering the comparability of the obtained results with the literature, silicon substrates were preferred in this thesis as it is a widely used material in the literature within FEBIP-based research. Furthermore, thick silicon oxide films were chosen to prevent any possible reactivity towards established/tested precursor molecules. As previously reported in the literature,[72] $(CH_3)AuP(CH_3)_3$ precursor leads to spontaneous deposition of gold on the surface defect sites of a thin (~ 40 Å) silicon oxide / Si(111) surface at 298 K for CVD in UHV. In the same study, the authors also showed that a thicker silicon dioxide film (~ 5000 Å) is not reactive anymore towards the $(CH_3)AuP(CH_3)_3$ compound at room temperature.

2.3.2 $Fe(CO)_5$

Iron pentacarbonyl ($Fe(CO)_5$) was purchased from Sigma Aldrich (> 99.99%). $Fe(CO)_5$ was used to understand low-energy electron and ion-induced surface reactions using the surface-science study approach. Prior to the experiment, the precursor container was wrapped with an aluminum foil due to its light sensitivity and cleaned using several freeze-pump cycles. Afterward, the quality was screened using MS (See Figure 6). If the precursor molecules are highly volatile and attached directly to the UHV chamber, in the first step, the compound needs to be frozen with liquid nitrogen, and later on, a purging process should be applied. This process can be called the freeze-pump cycle. It needs to be noted that the experiments with $Fe(CO)_5$ were performed in the laboratory of Prof. Howard Fairbrother at JHU.

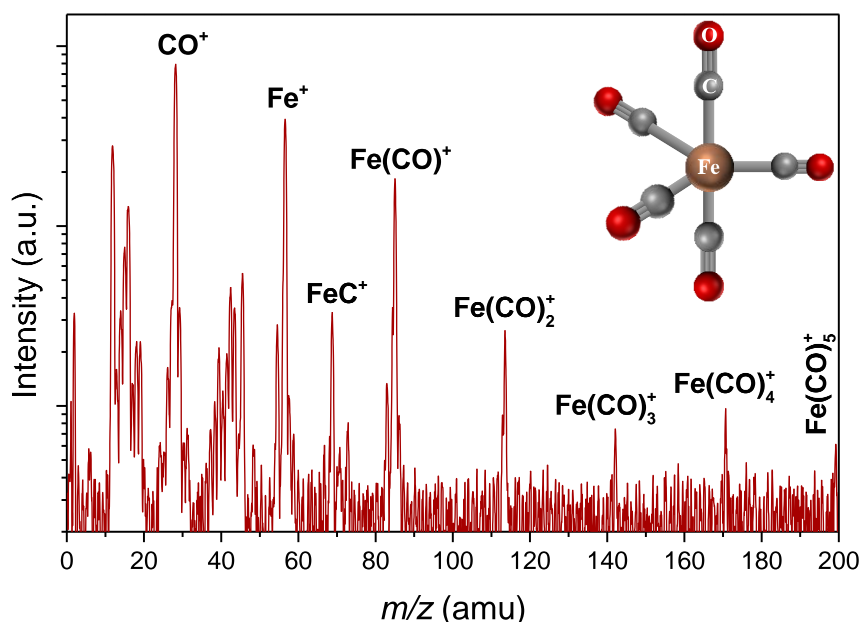

Figure 6. *Logarithmic plot of MS of $Fe(CO)_5$ at a compound temperature of 298 K, and a precursor pressure of 5×10^{-7} mbar.*

2.3.3 $Ru(CO)_4I_2$

Ruthenium tetracarbonyl diiodide ($Ru(CO)_4I_2$) compound (Figure 7) was synthesized using a modified literature procedure[73-75] by the group of Prof. Lisa McElwee-White from the University of Florida, USA. The compound was characterized by comparison to literature data:[73, 74] IR frequencies are found as 2158 (m), 2105 (vs), 2095 (s), 2066 (s) cm^{-1} (Appendix 1). The precursor was placed in glass fingers and attached to a UHV-compatible leak valve in a glove box, which was then attached to the UHV chamber. $Ru(CO)_4I_2$ was used for two different purposes. One was to understand the ligand cleavage behavior step by step using the surface science study approach described in detail in Chapter 3.1. The other was to fabricate nanostructures via FEBIP (c.f. Chapter 3.3). $Ru(CO)_4I_2$ was heated to 315 and 345 K in order to obtain sufficient vapor pressure to perform the surface science study onto the cooled substrate (173 K) and perform FEBIP onto the substrate at room temperature, respectively. Prior to each experiment, the precursor was exposed to vacuum several times via the turbopump of the UHV chamber without using liquid nitrogen (at room temperature) due to the relatively low vapor pressure of $Ru(CO)_4I_2$ compared to $Fe(CO)_5$ in order to remove residual gases present in the precursor container. During the purification step, chamber pressure and volatile fragments were observed by ion gauge and MS.

Figure 7 depicts the mass spectrum of the $Ru(CO)_4I_2$ precursor at 340 K on a logarithmic scale. The significant peaks are associated with C^+ (*m/z* = 12), O^+ (*m/z* = 16), CO^+/N_2^+ (*m/z* = 28), Ru^+ (*m/z* = 97, 100, 101, 102, 103, 105), and I^+ (*m/z* = 128, 129), indicate that at this temperature $Ru(CO)_4I_2$ is volatile enough to be detected by MS.

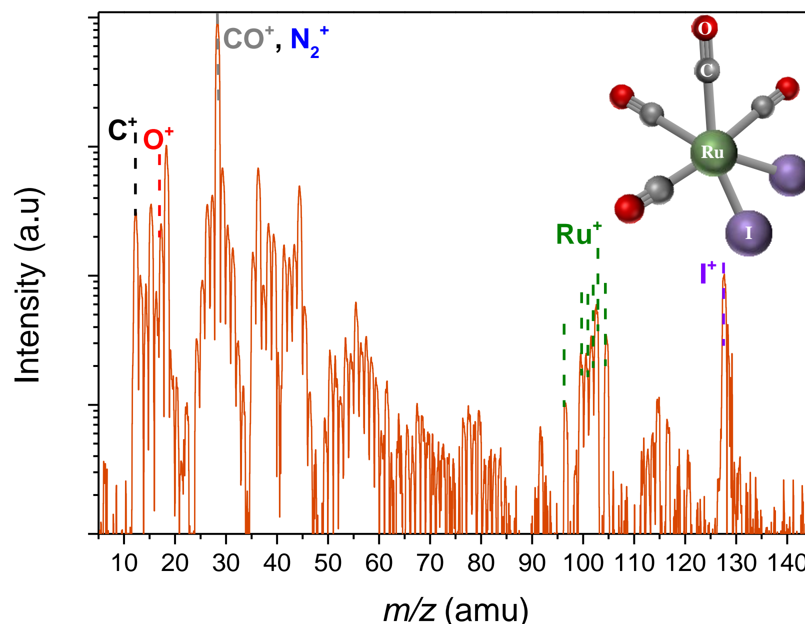

Figure 7. *Logarithmic plot of mass spectrum of $Ru(CO)_4I_2$ at a container temperature of 340 K, and a precursor pressure of 4×10^{-8} mbar.*

2.3.4 $(CH_3)AuP(CH_3)_3$

Methylgold(I) trimethylphosphane ($(CH_3)AuP(CH_3)_3$) (Figure 8) compound was synthesized by the group of Prof. Sjoerd Harder from Inorganic Chemistry at FAU. The synthesis steps were followed as described in the literature.[76] The compound quality was checked and confirmed by ^1H NMR spectra (Appendix 2-4). To understand the volatility and the quality of the precursor under UHV prior to the FEBIP experiment, the fragmentation of $(CH_3)AuP(CH_3)_3$ was monitored via MS at room temperature. In Figure 8, the detected precursor-related MS signals are assigned to CH_3^+ (*m/z* = 15), N_2^+ (*m/z* = 28), $P(CH_3)_2^+$ (*m/z* = 61), $P(CH_3)_3^+$ (*m/z* = 76) and Au^+ (*m/z* = 198). It should be noted that the MS signals for Au is shown at 197 *amu* in literature[76], whereas in this study, one strong MS peak was detected at 198 *amu*. The reason for the mass shift is the calibration error of the QMS. Deviations like this are typical for QMSs and increase with increasing mass (See the trend line data depicted in Appendix 5). The peak of the intact precursor at 288 *amu*,

which should be a good indicator for the concentration, could not be observed because it is out of range of our QMS which can only detect mass/charge ratios of up to 200. In this dissertation, the $(CH_3)AuP(CH_3)_3$ precursor was investigated in regard to fabricating FEBIP structures at FAU and compare these results with the reaction mechanisms of the isolated precursors in the gas phase by the impact of low energy electrons (< 100 eV) together with the group of Prof. Oddur Ingólfsson from University of Iceland (Chapter 3.4).

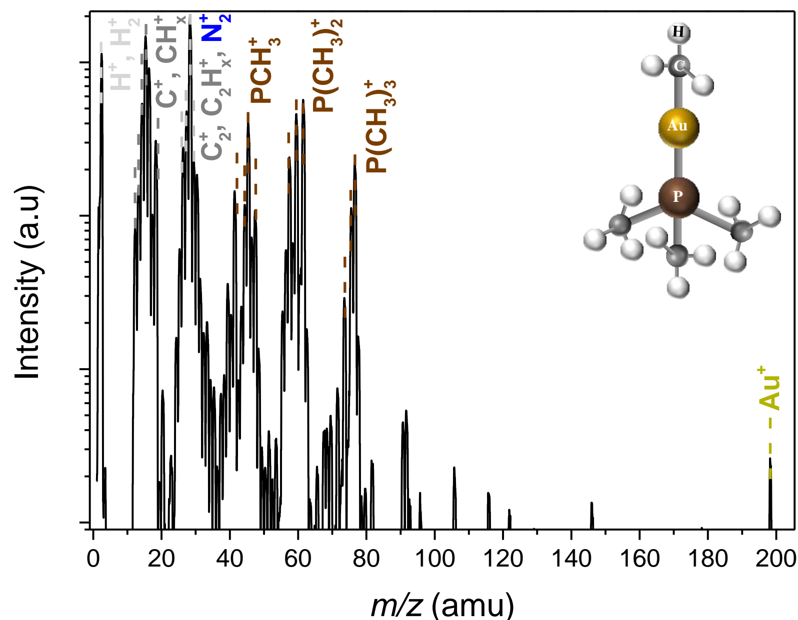

Figure 8. *Mass spectrum of $(CH_3)AuP(CH_3)_3$ at room temperature and a precursor pressure of 1.3×10^{-7} mbar in the logarithmic scale.*

2.4 Lithographic Parameters

The lithographic processes for FEBIP comprise three different techniques: Electron Beam Induced Deposition (EBID), Electron Beam Induced Surface Activation (EBISA), and Electron Beam Induced Etching (EBIE). In this thesis, the fabrication of nanostructures was obtained via EBID and EBIE.

The electron beam scans over the targeted spots on the substrate to write the FEBIP structures. The lithographic parameters such as dwell time, sweeps, and step size need to be adjusted to create nanostructures in a particular area. These lithographic parameters for FEBIP

experiments can be controlled with the custom-developed Nanoscribbler software based on LabView 8.6, as described in detail in the thesis of Florian Vollnhals.[77]

The distance between neighboring electron exposed points is denoted as step size. The electron beam has to spend a given amount of time on one point and then move to the next one. This time is referred to as dwell time ($t_{(dw)}$), and the dwell time can be varied in order to achieve the desired electron dose. The targeted area can be irradiated with the total electron dose either in one sweep or in multiple sweeps, and this parameter is consequently referred to as a number of sweeps. Some pre-requirements must be considered when setting the lithographic parameters, such as the adsorption, desorption, and dissociation rates according to the selected precursor molecule and/or the expected nanostructure morphology to be produced.

2.5 Fundamentals

2.5.1 Electron Beam Induced Deposition (EBID/FEBID)

The (focused) electron beam-induced deposition (EBID/FEBID) process is based on a combination of a highly focused electron beam from SEM with surface adsorbed precursors. Therefore, a suitable substrate is placed in a high vacuum (HV) or ultra-high vacuum (UHV) chamber which is equipped with SEM. The corresponding precursor, often metal-organic molecules, are filled inside a container, typically in a glove box, which is then attached to the Gas-Injection-System (GIS) of

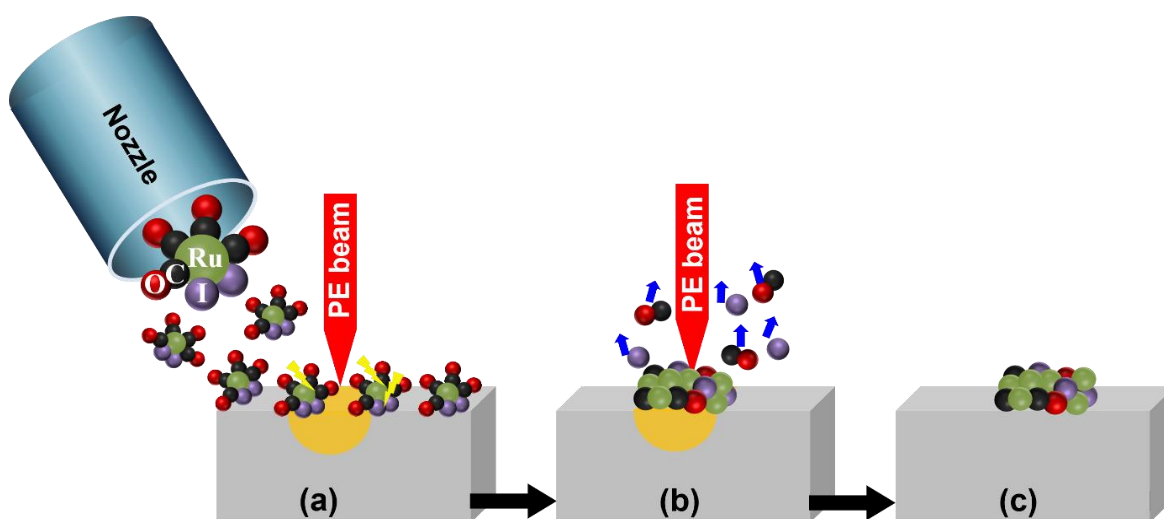

***Figure 9**. Representation of the FEBID process: (a) irradiation of adsorbed $Ru(CO)_4I_2$ with the focused electron beam; (b) dissociation of the precursor and desorption of volatile species; (c) final deposit.*[125]

the vacuum chamber. A GIS usually delivers the volatile precursor molecules into the chamber through a tube in close proximity to the substrate surface and thus enables the transport of the precursor onto the substrate.

Electron-induced reactions of the precursor lead to deposition of the non-volatile products, ideally metallic deposits from organometallic precursors. The shape of the deposits is thereby determined by the irradiation of the primary electron beam (0.5 – 50 keV), enabling the fabrication of arbitrary structures with lithographic control. Thereby the volatile reaction products, e.g., undesired organic ligands, are pumped out of the chamber. The mechanism of FEBID is sketched in Figure 9 on the example of $Ru(CO)_4I_2$ an organometallic precursor,[125] where the PE beam irradiates the adsorbed precursors on the substrate and yields the desorption of volatile fragments following the dissociation of the precursor bonds.

The main advantage of FEBID is being a direct-write technique that does not require a mask, photoresists, or developer materials during the writing process. In the literature, the widely-studied precursor molecules for FEBID have been reported as $MeCpPtMe_3$,[78] $W(CO)_6$,[79] $Fe(CO)_5$,[80] $Co_2(CO)_8$,[81] and $Co(CO)_3NO$[82] to create deposits containing platinum, tungsten, iron, and cobalt metals, respectively.

FEBID is gaining more and more interest in the industry, especially in the fields of mask repair,[83, 84] fabrication of tips for commercial AFM cantilevers,[36] single-electron resistors,[85] editing magnetic circuits,[86] and plasmonics[87] gaining from the flexibility of FEBID as a direct-write approach. Besides the discussed advantages of FEBID, there are also some drawbacks that need to be discussed, such as typically low metallic content in the deposits or proximity effects due to BSEs or FSEs.[88, 89] Previous studies reported metal contents higher than 60 at.% without applying any purification techniques for FEBID using $Fe(CO)_5$,[80, 90, 91] $Co(CO)_3NO$,[82] $Co_2(CO)_8$,[44, 92] and $W(CO)_6$,[93] $AgO_2(Me_2Bu/F_5Prop)$[94] precursor molecules. It is also possible to increase the metal content of the deposits by using pre-and/or post-purification techniques.[95] Proximity effects can be addressed, e.g., by using low-density substrates such as HKUST-1,[96] SAMs,[97] or CNMs.[98, 99] Using organic-based materials as a substrate has yielded very successful results not only by reducing the proximity effect[100, 101] to generate precisely defined nanostructures (i.e., sub 10 nm), but also in opening a new fabrication way[102] for hybrid structures. However, post-purification methods applied to increase the metallic content may also suffer from other disadvantages such as a decrease in deposition thickness[103, 104] or complete deterioration of the deposited structure.[105]

One exceptional example shows the successful purification process with the concurrent injection of precursor molecules and H_2O (oxidative enhancer) into the system, which yielded a pure gold deposit at the end.[106] Nevertheless, it would be ideal to have a precursor molecule (less sensitive, less reactive, more stable, more volatile) that can directly dissociate under the impact of an electron beam and create a deposit with a high metallic content in only one step, without any pre-/post-purification methods.

For the FEBID results presented in this thesis detailed in Chapters 3.3 and 3.4, a highly focused electron beam with the PE beam energies of 5 and 3 keV was used in combination with several organometallic precursors under UHV conditions.

2.5.2 Electron Beam Induced Etching (EBIE/FEBIE)

In general, the mechanism of (focused) electron beam-induced etching (EBIE/FEBIE) is similar to the aforementioned FEBID process. FEBIE is also referred to as a direct-write process (no photoresist, no mask) like FEBID and requires an electron beam, suitable precursors or reactive

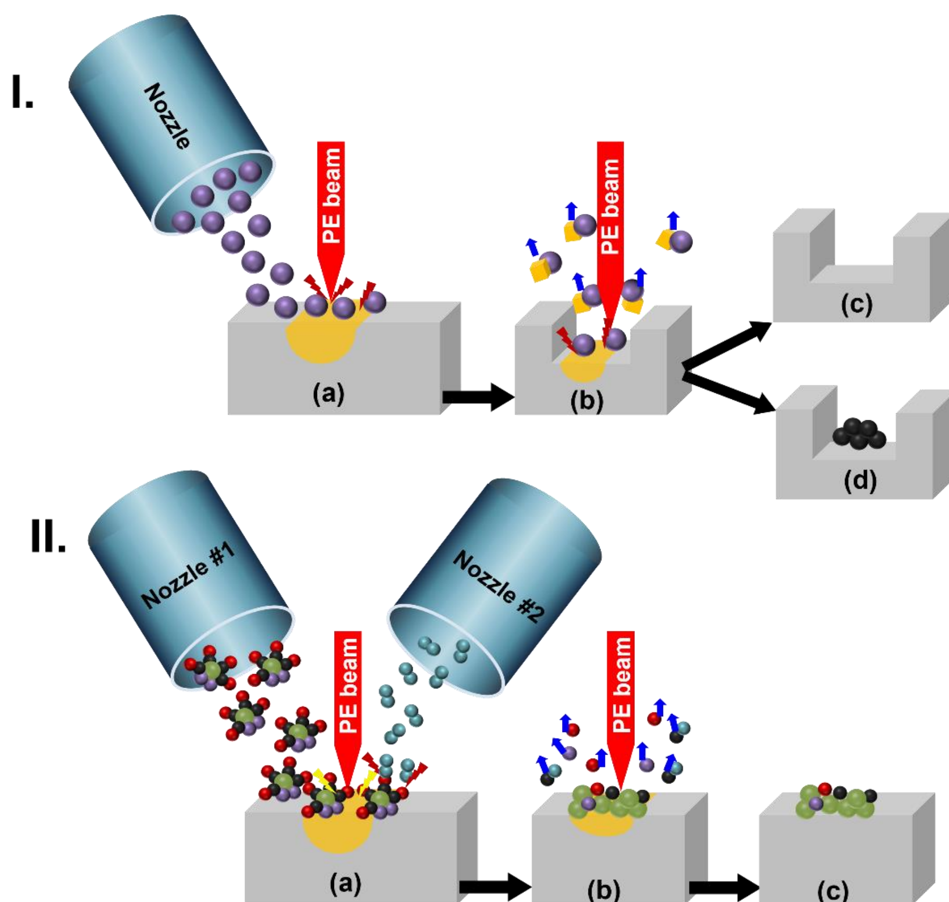

Figure 10. *Schematic representation of EBIE process using only one GIS (I.) and two GISs (II.). In I., the reactive gas is delivered from the nozzle on the substrate to start the etching process under the impact of PE beam, and results either in only etching of the substrate or simultaneous etching of the substrate and unintended deposition of impurities. In II., the metal-organic precursor is sent through the nozzle #1 concurrently with the reactive gases coming from the nozzle #2 to create EBID deposit using the etching of the deposit as a purification method such as removing carbon from deposit with the help of reactive gases.*

gases, substrate, and GIS under a HV,[70, 107] a UHV,[108] or in an environmental SEM (ESEM)[109]. The critical point where the etching process differs from the deposition process is the generation of reactive fragments after the dissociation step, which locally etches the substrate material to form a volatile compound. FEBIE has mainly developed as an alternative technique to the Focused Ion Beam (FIB) technique, in order to reduce the destructive damages created by energetic ions such as ion implementation in the deposits or material removal due to the sputtering.[110] FEBIE was a

standard technique to repair the defects on lithographic masks[83, 111] where the damage-free results are crucially important. Nowadays, it is succeeded by FEBID and FEBIE as the standard technique for mask repair due to the superior resolution and the lack of ion implementations in the material.[83, 111, 112]

In previously published papers, FEBIE has been extensively studied with the combination of halogen-containing precursors or reactive gases as source materials to trigger the etching process and subsequent formation of volatile products under the influence of an electron beam.[113] While the existing studies mainly focused on XeF_2,[114-117] also Cl_2,[108] ClF_3,[118] O_2[119], and H_2O[120] were reported as reactive gases to etch a wide range of materials such as semiconductors, oxides, or metals triggered by the impact of an electron beam. There are three different potential pathways to perform FEBIE under suitable conditions, as depicted in Figure 10. The first one includes only the etching process combining selected gaseous material and substrate; the second option is unintended simultaneous etching and deposition,[121] where the deposition of carbon impurities as a side product can be observed in mainly HV systems. The final one actually requires two GISs, where one GIS needs to be filled with the organometallic precursor to create a deposit, and the other GIS needs to deliver oxygen or H_2O into the system (i.e., two gases, precursor and reactive gas, need to be dosed simultaneously) for the purification of deposited material (i.e., to assist in removing extra carbon ligands).[106] At this point, the critical question may arise: how to control which process (etching or deposition) will dominate under which parameters? The conditions have been specified in literature only for FEBIE as follows; a low hydrocarbon level in the chamber, along with a focused low-energy high-current electron beam, and short or long dwell times depending on the systems.[108, 117] To understand and control the leading process in the case of simultaneous FEBIE and FEBID, a simple theoretical model based on a rate equation describing the precursor molecule coverage, N (cm^{-2}), on the surface has been developed in the literature.[122] This model includes three contributions: the number of molecules that adsorb from the gas phase, the number of molecules decomposed by the electron beam, and the number of molecules that desorb to the gas phase. When considering a steady-state situation for the surface coverage, when the electron current density, J ($cm^{-2}\ s^{-1}$), in the system is much higher than the gas flux arriving on the surface, F ($cm^{-2}\ s^{-1}$), the growth rate is restricted only by the precursor gas flux; this is referred to as precursor-limited regime.[122-124] In another situation, when the precursor gas flux is much higher than the applied current density, consequently the growth is then limited only by the applied

electron beam current density; this regime is referred to as the electron-limited regime.[122-124] According to the given references[122-124] and the results obtained from [P3],[125] in the precursor-limited regime, EBIE has become a dominant process due to the depletion of adsorbed precursor molecules; however, in the electron-limited regime, EBID can be obtained as a leading process. Thus, in order to switch from etching to deposition or from deposition to etching in a simultaneous system, one might consider varying some parameters such as precursor gas flux, electron flux or current density.[116, 124] Before attempting to comprehend the underlying mechanism of EBIE, it is worth mentioning that etching is probably a more complex mechanism than deposition, considering the activation of the surface site and secondary reactions induced by the etch-related products. There are only few published studies regarding the underlying mechanism of FEBIE.[70, 126] For the SiO_2 substrate for FEBIE, the etching mechanism has been explained in the literature[113, 117] as the electron-induced decomposition of SiO_2 toward Si. The electron-stimulated desorption of oxygen from the surface creates active sites such as oxygen vacancies.

In this dissertation, the FEBIE process was observed alongside the deposition in a simultaneous and competitive way using only one halogen-based precursor ($Ru(CO)_4I_2$) in the precursor-limited regime in UHV. The findings are described in detail in Chapter 3.3.

2.5.3 Electron Beam Induced Interactions

A better understanding of electron beam-induced interactions is needed, as secondary electrons significantly contribute to FEBID process. Interactions with the high energetic electron beam and the substrate surface generate both elastically and inelastically scattered electrons which were discussed in Chapter 2.1.1. The BSEs and FSEs are responsible for scattered electrons, which create unintended deposits close to the area of the impact point of the primary electron beam.[38, 88] The corresponding effects are referred to as proximity effects,[38] and the area where unintended deposits are observed can be visualized either by experimental approaches or by simulation. Electron Beam Induced Surface Activation (EBISA)[127] is another nanopatterning technique where the surface is activated without the presence of precursor molecules in the chamber, and afterward, precursors are delivered directly on these activated surface sites to dissociate there and eventually create deposits. Due to the direct interaction between substrate and primary electrons, EBISA is the perfect experimental approach to investigate the BSE-induced proximity effect. Beside EBISA, EBID can also be used to examine the BSE proximity effect; however principally expected to

overlap with the forward scattering electron (FSE) effects, especially at high electron doses.[128] Furthermore, Monte Carlo software-based CASINO simulation program[129] can be used to simulate the trajectory of the scattered electrons inside the sample. Thus, the combination of experimentally obtained proximity effects and the simulated BSE exit area knowledge allows extracting the BSE-induced proximity effects.[88] Regarding the FSE-induced proximity effect, the impact of FSE, particularly in high aspect ratio FEBID structures is prominent, and has been observed in literature several times in different forms such as Ray-like deposits in EBID + autocatalytic growth (AG),[130] or broadening in deposits on the edges of 3D structures.[131-133] In this case, the results can be explained using Monte Carlo-based simulation programs,[134] as in BSE induced proximity effect.

The second electron beam-induced interaction to be considered is the interaction between precursor molecules and the low-energy secondary electrons (LEEs, <100 eV). The interactions between LEEs and precursor molecules are essential as the primary deposition mechanism in FEBID is initiated by the low energetic secondary electrons.[51, 135-137] Accordingly, it is important to study the isolated effect of LEEs on precursor molecules to have a deep understanding of the underlying mechanism of FEBID. Hence, these interactions have been widely studied by isolated gas-phase and surface science studies.[51, 69, 138-140] These two complementary techniques have identified four primary electron-induced interactions with isolated precursor molecules: dissociative electron attachment (DEA), dissociative ionization (DI), neutral dissociative (ND), and dipolar dissociation (DD).[141-143] These four electron-induced interactions may contribute to the deposition process in FEBID. However, using a combined specific UHV-surface science and isolated gas-phase studies, only DEA and DI have been identified to play a significant role in the FEBID process so far.[51, 144, 145] In DEA, when an electron attaches to a molecule, a short-lived negative ion is formed, which afterwards transforms into a negative and one or more neutral fragments ($AB_{(molecule)} + e^- \rightarrow AB^{-*}_{(parent\ ion)} \rightarrow A^{\cdot} + B^-$).[144] In DI, unlike DEA, an electrically charged product (daughter ions) and neutral fragments are observed after the dissociation of the parent precursor ion due to the electron impact ($AB_{(molecule)} + e^- \rightarrow AB^{+*}_{(parent\ ion)} + 2e^- \rightarrow A^+ + B^{\cdot} + 2e^-$).[144] In FEBID, from the obtained results using the combined gas-phase and surface science studies, DI-induced precursor dissociation of precursor molecules is usually associated with the loss of multiple ligands and related to the initial decomposition/deposition of FEBID precursors.[51, 136, 146] While DI-induced dissociation yields more ligand desorption, neither DEA

nor DI can be shown as a reason of the complete loss of all ligands related to the precursor, as substrate-related effects cannot be ruled out for the entire FEBID process.

The last electron beam-induced interaction is the electron interaction with adsorbed precursor molecules. Here, the interaction mechanism is slightly different and more complex than in the isolated-gas phase. The dissociative mechanism on the adsorbed molecules provides more fragmentation channels due to the substrate material underneath. However, it is challenging to identify these fragmentation channels per scatter event as multiple scattering effects might occur simultaneously.[36, 147] Also, on the adsorbed film, the dissociated product might react with neighboring molecules, and this might then activate further relaxation channels.[148, 149]

In this dissertation, electron beam-induced interactions have been investigated from different perspectives, such as to study the correlation between UHV-FEBID and the gas-phase studies (Chapter 3.4), the difference between the electron- and ion-induced reactions with $Fe(CO)_5$ (Chapter 3.2), or the effect of electron beam induced interactions on simultaneous and competitive FEBIE and FEBID processes (Chapter 3.3).

2.5.4 Ion Beam Induced Interactions

Besides FEBID and FEBIE, there is another direct fabrication technique, namely Focused Ion Beam Induced Deposition (FIBID). FIBID has quite similar working conditions as FEBID, except instead of high energetic electrons, high energetic (> 0.5 keV) ions, mostly He^+ or Ga^+,[150, 151] are used to create well-defined nanostructures. Due to the increasing interest in smaller and better-quality nanostructures, molecular-level understanding of ion-beam-induced interactions is becoming more and more vital. Few studies have been focused on understanding the molecular-level ion-induced interactions that lead to deposition in FIBID.[56, 152, 153] The interactions between high energetic ions with the substrate and adsorbed precursor molecules, as well as the interactions with the secondary electrons generated by the impact of high energetic incoming ions on the surface and the precursor molecules, should be considered as ion-induced reactions.

Interactions between high energetic ions and the substrate material can be explained by the collision-cascade model.[56] In this model, energetic atoms are produced within the surface due to the momentum/energy transfer from the energetic primary ions to the surface atoms. These generated energetic atoms then transfer their energies to the adsorbed precursor molecules, and thereby initiates the deposition process.

One more effect has been suggested regarding the concept of interaction between energetic ions and the substrate surface, in which the high energy ions might induce a local temperature increase in the near-surface area. Since it has been discussed in the literature that the deposition process in FIBID might be initiated due to the thermal decomposition of adsorbed molecules, this effect is referred to as the thermal spike model.[56] This thermal spike model can be excluded in the case of the FIBID under cryogenic conditions[154] (cryo-FIBID); here, one needs to consider the direct interactions between the primary ions and the adsorbate molecules; in the literature, these direct contributions are called as ion-electronic cloud or ion-molecular nuclei.[152] This direct interaction under cryogenic conditions allows for the observation of ion-induced decomposition and/or ion-induced desorption of adsorbed precursors.[50, 154]

The last ion beam-induced interaction occurs between the secondary electrons generated after the impact of ion beams on the surface and adsorbed precursors (secondary electron model),[153] which then leads to decomposition, desorption, and finally deposition of adsorbed precursors under vacuum conditions.

In Chapters 3.1 and 3.2, the UHV surface science approach was used to elucidate the reactions between $Ru(CO)_4I_2$ and $Fe(CO)_5$ precursor molecules and low-energy argon ions (860 and 1200 eV, respectively).

3 Results

A notable challenge of focused charged particle beam-induced deposition (FEBID/FIBID) processes is that the corresponding deposits often exhibits rather low metal contents due to contamination from residual gases or ligands of the organometallic compounds. A deeper understanding of the interactions between charged particles and the different metal centers respective various types of ligands is pivotal to gain a molecular-level understanding of the deposition process and thus to improve FEBID and FIBID processes accordingly. To do so, a specific UHV surface science approach with a combination of XPS and MS was applied to elucidate the elementary surface reactions initiated by the interaction of low energetic argon ions with the organometallic precursor $Ru(CO)_4I_2$ [P1]. The same experimental approach was utilized to compare the surface reactions triggered by low energetic electros and low energetic argon ions on thin adsorbed $Fe(CO)_5$ layers [P2]. In order to survey new precursor molecules and make them compatible with UHV-based FEBID, the fabrication of ruthenium- and gold-containing deposits have been targeted using $Ru(CO)_4I_2$, and $(CH_3)AuP(CH_3)_3$ as precursors [P3 and P4]. In addition, obtained FEBID results using $(CH_3)AuP(CH_3)_3$ were compared with the isolated gas-phase approach to investigate the reaction pathway of the compound under the impact of the electron beam. Further experimental details can be found in the publications, [P1] – [P4], in the appendix section.

3.1 Surface Reactions of Low-Energy Argon Ions with $Ru(CO)_4I_2$ Precursors [P1]

In order to evaluate the potential of a novel organometallic compound for FIBID, and to understand the corresponding fundamentals of interactions between ions and adsorbed precursor molecules, the low energetic (860 eV) Ar^+ induced reactions with nanometer-thick $Ru(CO)_4I_2$ films using the specified surface science approach were studied. The corresponding results are summarized in this chapter. Here, only $Ru(CO)_4I_2$ precursor is discussed; for the comparison of ion-induced reactions with the other precursor molecules ($Co(CO)_3NO$ and $WN(NMe_2)_3$), please refer to the original paper [P1] in the appendix.

The experiments were performed during a four-month research stay at Johns Hopkins University within the ELENA-ITN Project, under the supervision of Prof. Howard Fairbrother. The $Ru(CO)_4I_2$ precursor was synthesized by our collaborative partner Prof. Lisa McElwee-White from the University of Florida within the ELENA-ITN Project, who also provided IR result for this compound (Appendix 1).

Figure 11 depicts XPS data for C(1s), Ru(3d), O(1s), and I($3d_{5/2}$) regions on the adsorbed $Ru(CO)_4I_2$ films with increasing ion beam doses. There is an overlap between C(1s) and Ru(3d) signals in XPS; therefore, the spectra have been deconvoluted.[155] Before the ion beam exposure, there are four main peaks in the C(1s)/Ru(3d) region, centered at 294.4, 289.2, 287.4 and 283.2 eV. The two higher binding energy peaks (depicted in blue) at 289.2 and 294.4 eV are attributed to the C(1s) peak of the $\underline{C}O$ ligand in $Ru(CO)_4I_2$ and the π-π* shake-up transition of a C(1s) core level electron in a metal carbonyl, respectively.[62, 156] The two lower binding energy peaks at 283.2 and 287.4 eV (depicted in red) are associated with the Ru($3d_{5/2}$:$3d_{3/2}$) doublet of the initial $Ru(CO)_4I_2$ compound.[155, 157] The O(1s) region before the ion beam exposure (0 mC/cm^2, Figure 11b), initially has two main peaks, one of them centered at 535 eV and the other one centered at 541 eV. The largest one at 535 eV is attributed to the $C\underline{O}$ ligands of the $Ru(CO)_4I_2$ molecules, and the smaller peak in this region is a π-π* shake-up feature.[158, 159] Before the ion beam exposure, the I($3d_{5/2}$) region shows one peak at 619.8 eV.[160]

After the ion beam exposure, there is a considerable decrease in the initial Ru species (depicted in red) and the C(1s) peak assigned to the $\underline{C}O$ ligands. In Figure 11a, notably for the low ion beam exposures (≤ 0.0012 mC/cm^2), there is no observable peak for π-π* transition in the C(1s) region anymore, but there is a simultaneous increase in the two new peaks centered at 281.7 and 285.9 eV (depicted in green) assigned to the Ru($3d_{5/2}$) and Ru($3d_{3/2}$) doublet, respectively, of a newly formed species. These new peaks are associated with the species produced by ion bombardment. For the product Ru species, the spectral intensity remains relatively constant on the surface upon ion beam exposure up to 0.036 mC/cm^2 but then decreases in intensity for larger ion doses. The C(1s) peak intensity rapidly decreases, and after an ion exposure of 0.036 mC/cm^2, there is no visible C(1s) peak in the corresponding XPS region. The O(1s) peak in Figure 11b exhibits a rapid decrease upon ion beam exposure and vanishes for ion beam doses higher than 0.036 mC/cm^2. In the I($3d_{5/2}$) region, for low ion doses (< 0.024 mC/cm^2), there is only a very slight change in iodine peak intensity. However, at Ar^+ doses higher than 0.024 mC/cm^2, the iodine

peak decreases, and for ion doses higher than 0.072 mC/cm^2, only very small amount of iodine can be observed in Figure 11c.

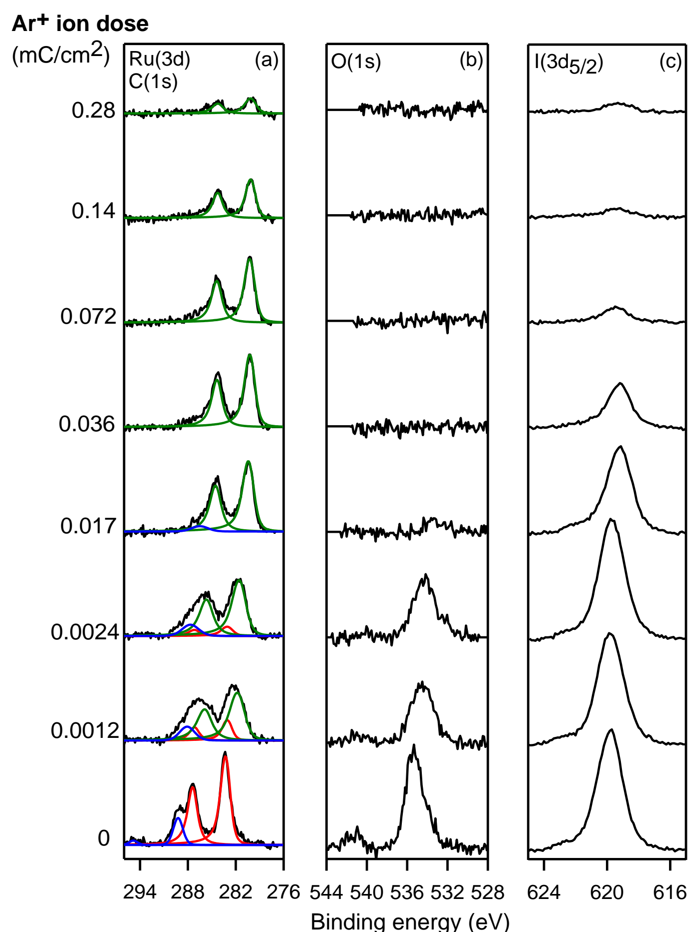

Figure 11. *Evolution of the C(1s)/Ru(3d), O(1s), and I(3d$_{5/2}$) XPS regions for ~ 1.6 – 1.7 nm films of $Ru(CO)_4I_2$ adsorbed onto a Au substrate at 173 K and exposed to increasing dose of Ar^+ ions. The C(1s)/Ru(3d) region is fit to show contributions clearly from the carbonyl carbon (blue), the initial Ru species (red), and the final Ru species (green). (Original image from [P1] with permission from the Journal of Physical Chemistry C.)*

Figure 12 shows the integrated spectral intensities as a function of Ar^+ ion dose, where the data points are normalized to the value measured for the $Ru(CO)_4I_2$ film before the ion beam exposure. The different colored shaded rectangles were added to indicate the sequential steps of ion-induced reactions.

Figure 13 combines the information from XPS (peak position/Ru3d and intensity/O1s) with the corresponding QMS signal referring to m/z = 12, i.e., characteristic for CO, to illustrate the behavior of the latter upon increasing Ar^+ beam exposure. Therefore, MS signal (black line) is

plotted for the normalized mass-charge ratio of 12 (m/z = 12 for C^+) together with the corresponding fractional CO coverage indicated by the O(1s) intensity and the peak position of the Ru($3d_{5/2}$) signal. The data presented in Figure 13 yields a consistent picture such that the amount of released CO (MS signal, black line) is in line with the decrease of the O(1s) signal (dark-red squares), i.e., the amount of CO on the surface, and both are correlated to a shift of the Ru($3d_{5/2}$) (green triangles) peak toward lower binding energies in XPS. The inset in Figure 13 depicts an exemplary MS spectrum of the adsorbed $Ru(CO)_4I_2$ molecule under the ion beam bombardment. When the adsorbed molecule is irradiated by 0.00008 mC/cm^2 exposure of ion beams, the only significant MS peaks detected are those correlated with Ar^+ (m/z = 40), Ar^{++} (m/z = 20) and CO (m/z = 28, 16, and 12). Ru^+ (m/z = 102) and I^+ (m/z = 126) peaks were not observed in the MS during ion beam stimulated desorption of $Ru(CO)_4I_2$ molecule.

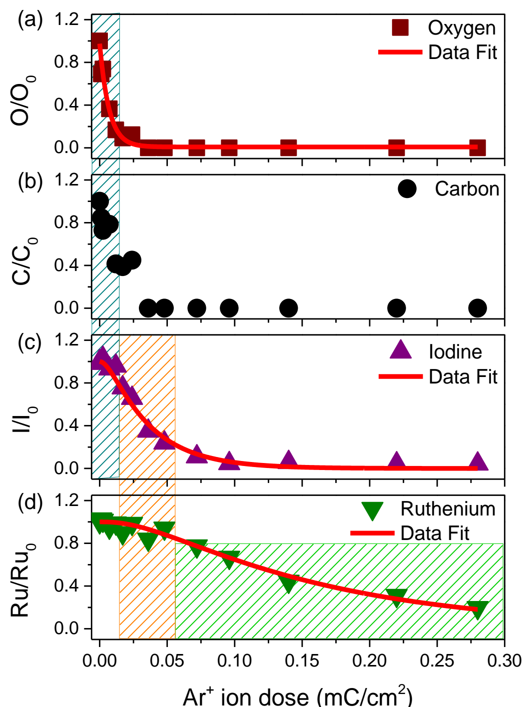

Figure 12. *Change in fractional coverage of O, C, I, and Ru atoms as a function of increasing Ar^+ dose. The blue-colored (σ_1; $Ru(CO)_4I_2$ decomposition), orange-colored (σ_2; iodine sputtering), and green-colored (σ_3; ruthenium sputtering) shaded rectangles depicted reaction steps in sequential order. The graphs (a), (c), and (d) were fit by the integrated rate functions shown in Eq. 7, Eq. 8, and Eq. 9, respectively (Adapted figure from [P1]).*

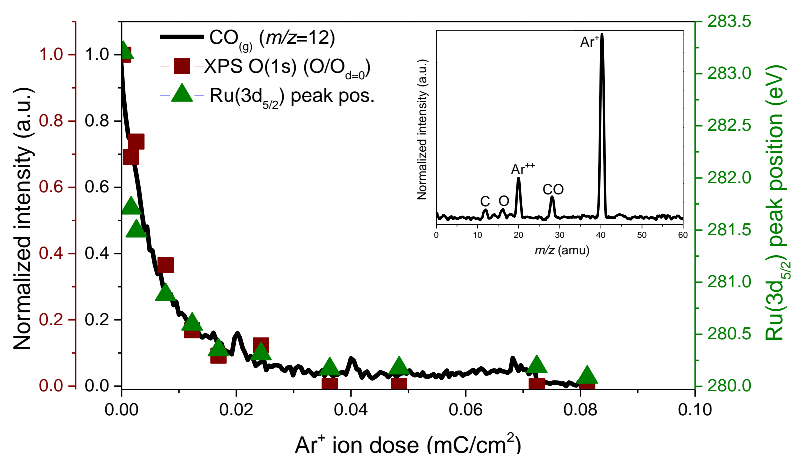

Figure 13. *Kinetics of CO (m/z = 12 amu, C^+) desorption from an adsorbed $Ru(CO)_4I_2$ film and its correlation with the fractional coverage of O atoms and the decrease in binding energies for the $Ru(3d_{5/2})$ peak position. MS and XPS signals were both normalized to their values at the onset of ion bombardment. The inset shows the mass spectrum of species desorbing from the $Ru(CO)_4I_2$ film after 0.00008 mC/cm^2 of ion beam bombardment (Adapted figure from [P1]).*

The discussed data yields the interpretation that exposure with the low Ar^+ doses (< 0.036 mC/cm^2), the decomposition of $Ru(CO)_4I_2$ is the first Ar^+-induced process which is then followed by the dissociation and complete desorption of 4 CO ligands (Figure 12a and 12b, blue dashed area), and finally remaining $RuI_{2(ads)}$ species on the surface. According to Figure 13, the claim that all 4 CO ligands desorb intact is well supported by the correlation between the desorption of CO and the loss of all oxygen atoms from the surface. For Ar^+ ion bombardments between ~ 0.036 and 0.072 mC/cm^2, all CO ligands have desorbed, and sputtering of iodine is the dominant process, as can be seen in Figure 11 and Figure 12 (orange dashed area). Accordingly, for the Ar^+ exposures higher than 0.072 mC/cm^2 (Figure 12d, green shaded square), Ru is the only variety remaining on the surface (~ 90 at.% Ru). The consecutive reaction steps of $Ru(CO)_4I_2$ under the exposure of low energetic Ar^+ is expressed in Eq. 6. It is necessary to note that since the volatile ruthenium and iodine fragments have not been assigned in MS (c.f. Figure 13), they have been excluded, and thus, the reaction chain (Eq. 6) is not balanced.

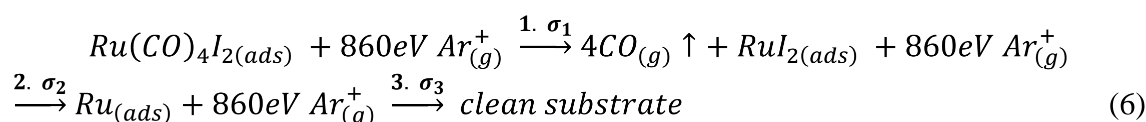

$$Ru(CO)_4I_{2(ads)} + 860eV\ Ar^+_{(g)} \xrightarrow{\mathbf{1.}\ \sigma_1} 4CO_{(g)} \uparrow + RuI_{2(ads)} + 860eV\ Ar^+_{(g)} \xrightarrow{\mathbf{2.}\ \sigma_2} Ru_{(ads)} + 860eV\ Ar^+_{(g)} \xrightarrow{\mathbf{3.}\ \sigma_3} clean\ substrate \quad (6)$$

The cross-section of ion-induced $Ru(CO)_4I_2$ decomposition (σ_1, Eq. 6) can best be determined by fitting the loss of oxygen signal to a first-order decay function:

$$\frac{O_d}{O_0} = e^{-\sigma_1 d} \tag{7}$$

Here, σ_1 is the decomposition cross-section, d is the ion dose, O_d is the oxygen coverage at dose d, and O_0 is the oxygen coverage at d = 0 mC/cm^2. This equation was fitted to the O(1s) coverage, as shown in Figure 12a (red-line), and the cross-section (σ_1) was found to be 2.3×10^{-15} cm^2 ($R^2 = 0.99$; the result of the fitting procedure).

Based on equations (6) and (7), and Figure 12c (orange dashed area), the decrease in iodine atom coverage occurs only after the formation of RuI_2; thus, the loss of iodine may be described by the following equation:

$$\frac{I_d}{I_0} = \frac{\sigma_2 e^{-\sigma_1 d} - \sigma_1 e^{-\sigma_2 d}}{\sigma_2 - \sigma_1} \tag{8}$$

where I_d is the iodine coverage at dose d, I_0 is the iodine coverage at d = 0 mC/cm^2, σ_1 is the decomposition cross-section for the first step of the reaction chain (228.8×10^{-17} cm^2), σ_2 is the decomposition cross-section for the second step of the consecutive reaction (Eq. 6), and d is the Ar^+ dose.

Results of the data analysis using this fitting procedure are shown as the solid red line in the iodine region of Figure 12c, wherein σ_2 was determined to be 50.1×10^{-17} cm^2 ($R^2 = 0.99$; the result of the fitting procedure). It is worth mentioning that this fitting process considers for the delay in the loss of iodine for small Ar^+ exposures lower than 0.010 mC/cm^2, due to the formation of RuI_2.

For higher Ar^+ exposures (≥ 0.072 mC/cm^2), after all of the CO ligands have been desorbed, and most of the iodine has been sputtered, sputtering of ruthenium starts (Figure 11a and Figure 12d).

Therefore, the rate function for coverage of Ru atoms can be written as:

$$\frac{Ru_d}{Ru_0} = \left(\frac{\sigma_1\sigma_2}{(\sigma_2-\sigma_1)(\sigma_3-\sigma_1)}\right) e^{-\sigma_1 d} + \left(\frac{\sigma_1\sigma_2}{(\sigma_1-\sigma_2)(\sigma_3-\sigma_2)}\right) e^{-\sigma_2 d} + \left(\frac{\sigma_1\sigma_2}{(\sigma_1-\sigma_3)(\sigma_2-\sigma_3)}\right) e^{-\sigma_3 d} + \left(\frac{\sigma_2 e^{-\sigma_1 d}-\sigma_1 e^{-\sigma_2 d}}{\sigma_2-\sigma_1}\right) \quad (9)$$

Here, Ru_d is the ruthenium coverage at dose d, Ru_0 is the ruthenium coverage at d = 0 mC/cm^2 dose, σ_1 is the cross-section for Eq. 7 (228.8×10^{-17} cm^2), σ_2 is the cross-section for Eq. 8 (50.1×10^{-17} cm^2), σ_3 is the cross-section for Eq. 9, and d is the Ar^+ dose. This function (Eq. 9) was fitted to the Ru coverage data in Figure 12d, and the results are shown as a solid red line, giving a cross-section (σ_3) of 1.2×10^{-16} cm^2 ($R^2 = 0.98$; the result of the fitting procedure). The calculated cross-sections from the derived kinetic models indicate that the rate of the ion-induced decomposition of the $Ru(CO)_4I_2$ precursor leading to CO loss is approximately 5 times faster than the sputtering of I from RuI_2. In addition, the rate of iodine sputtering is also ~5 times faster than the rate of Ru sputtering.

As outlined above, the first reaction step in Eq. 6 occurs as a result of energy transfer from the incident argon ions to the adsorbed precursor molecules, which then yields a nonvolatile metal-containing deposit on the substrate. After this first step, preferential sputtering of halogen-based light elements (i.e., iodine) occurs. Thus, the insights provided by this study highlight the capability of a UHV surface science approach to gain molecular-level insights into surface processes relevant to FIBID. In addition, the structure of the $Ru(CO)_4I_2$ molecule found as suitable for the ion beam-induced reactions, and under appropriate ion beam-induced deposition conditions with precisely set parameters, the $Ru(CO)_4I_2$ compound could produce pure Ru deposits.

3.2 Low Energy Electron- and Ion-Induced Reactions of $Fe(CO)_5$ [P2]

For the advancement of FEBID and FIBID techniques as nanofabrication tools, a key aspect is to gain a better understanding of the electron- and ion-induced reactions that accompany deposition, as discussed in Chapters 2.5.3 and 2.5.4.

The experiments presented in this study were performed during a four-month research stay at Johns Hopkins University under the supervision of Prof. Howard Fairbrother. In this chapter,

using *in situ* XPS, the effects of low energy (500 eV) electrons and low energy (1200 eV) Ar^+ ions on thin films of $Fe(CO)_5$, a well-studied organometallic precursor, have been investigated.

Figure 14 shows the evaluation of C(1s), O(1s), and Fe(2p) XPS regions for adsorbed $Fe(CO)_5$ thin films (1.8 – 2.6 nm) held at a temperature of 143 ± 5 K under the irradiation with 500 eV electrons and 1200 eV Ar^+. In Figure 14a and Figure 14b, the C(1s) region of the as-deposited $Fe(CO)_5$ precursor (prior to electron and ion exposures) is described by two peaks, shown as solid red curves: the high intense peak at 287.5 eV and the other peak at 293.1 eV are assigned to binding energies of $\underline{C}O$ ligands and π-π* shake-up peak (i.e., π-π* for metal carbonyls)[158] in the C(1s) region, respectively. The peaks at 287.5 and 293.1 eV in the C(1s) region as shown in Figure 14a decrease in intensity upon 500 eV electrons irradiation. Increasing the electron dose higher than 3.6 mC/cm^2 yields a shift for the peak at 287.5 eV to a lower binding energy of 286.8 eV, and a new lower binding energy peak at approximately 284.1 eV (Figure 14a, blue curve). Upon bombardment with 1200 eV Ar^+ in Figure 14b, the main $\underline{C}O$ peak in C(1s) at 287.7 eV and the π-π* shake-up peak at 293.2 eV (both shown as red curves) decrease in intensity, and concurrently, a new peak at a binding energy of 283.7 eV (blue curves) appears and is indicated to be graphitic carbon (C_{gr}). After Ar^+ irradiation of 0.22 mC/cm^2 of, the CO peaks have vanished, and the C(1s) region is composed solely of C_{gr}. After an Ar^+ dose of 0.99 mC/cm^2, the intensity of C_{gr} peak slowly decreases until almost most of the carbon-containing species have been removed (Figure 14b). However, there is an increase in the intensity of C_{gr} peak at 283.7 eV under prolonged electron doses in Figure 14a.

Before electron and ion exposures, the O(1s) region of the as-deposited film is characterized by three peaks in Figure 14a and Figure 14b. The two peaks at lower binding energies overlap and create an asymmetrical one peak at approximately 533.6 eV, and are assigned to the signal of the $C\underline{O}$ ligands.[161] The third peak at a binding energy of 539.6 eV is attributed to the $C\underline{O}$ π-π* shake-up peak.[158] In Figure 14a, the intensity of the main asymmetric O(1s) peak ($C\underline{O}$ oxygen species) decreases with increasing electron irradiation, and the peak position shifts to a lower binding energy. A new peak begins at a lower binding energy of 530.2 eV, ascribed to an iron oxide species.[162] After an electron dose of about 14 mC/cm^2, this peak becomes noticeable (Figure 14a, O(1s), blue solid curve with a black dashed line). The resolved oxide peak at 529.9 eV in the O(1s) region for the electron doses higher than 650 mC/cm^2 is attributed to the residual CO species.[162]

Upon 1200 eV Ar^+ irradiation, there is only a systematic decrease in the intensity of C<u>O</u> O(1s) peak. In contrast to the electron irradiation, no measurable oxide O(1s) peak is observed.

The Fe(2p) region in Figure 14a and Figure 14b for the as-deposited adsorbed layers is described by two asymmetric peaks at approximately 708.8 and 721.7 eV, corresponding to $Fe(2p_{3/2})$ and $Fe(2p_{1/2})$ transitions, respectively.[161] In the Fe(2p) region, the background is shown as a green curve in each case. In the Fe(2p) region (Figure 14a), electron irradiation leads to the broadening of Fe(2p) peaks and shifts them to lower binding energies. In Figure 14a, the Fe(2p) region is defined by two peaks at 707.8 and 720.7 eV for the electron doses higher than 650 mC/cm^2, as well as a shoulder peak at a higher binding energy of 710.3 eV, the latter being indicative of an iron oxide features.[162, 163] Upon 1200 eV ion exposure, the results obtained from the Fe(2p) region are considerably different than the changes observed upon electron irradiation (compare Figure 14a and Figure 14b). There is no iron oxide-related peak found in Figure 14b, but just an increase in the high binding energy at 720.7 eV of the Fe(2p) peaks and a decrease in the $Fe(2p_{3/2})$ peak position from 708.8 to 707.5 eV, indicative of a metallic Fe.[161] This result is supported by the observation that for argon doses higher than 0.028 mC/cm^2, Figure 14b shows iron atoms are removed from the surface. In contrast to ion exposure, no iron atoms desorb during electron irradiation (Figure 14a and Figure 14b, Fe(2p) regions).

Figure 15a shows the decrease in the fractional coverage of carbon and oxygen atoms as a function of electron doses in mC/cm^2. Both elements (C/C_0 and O/O_0) show a quick decrease to approximately half of their initial coverage value for the electron doses < 20 mC/cm^2, but after that, stay constant. Figure 15b depicts the fractional coverage of graphitic carbon (open squares) and oxide from residual CO (blue squares) upon irradiation with 500 eV electrons. For the electron doses higher than 650 mC/cm^2, the graphitic carbon and oxide species are lost by about 80% compared to the original C(1s) or O(1s) signal, respectively, which is equivalent to ~ 1 carbon or oxygen atom removed from the original 5 CO ligands per $Fe(CO)_5$ molecule.

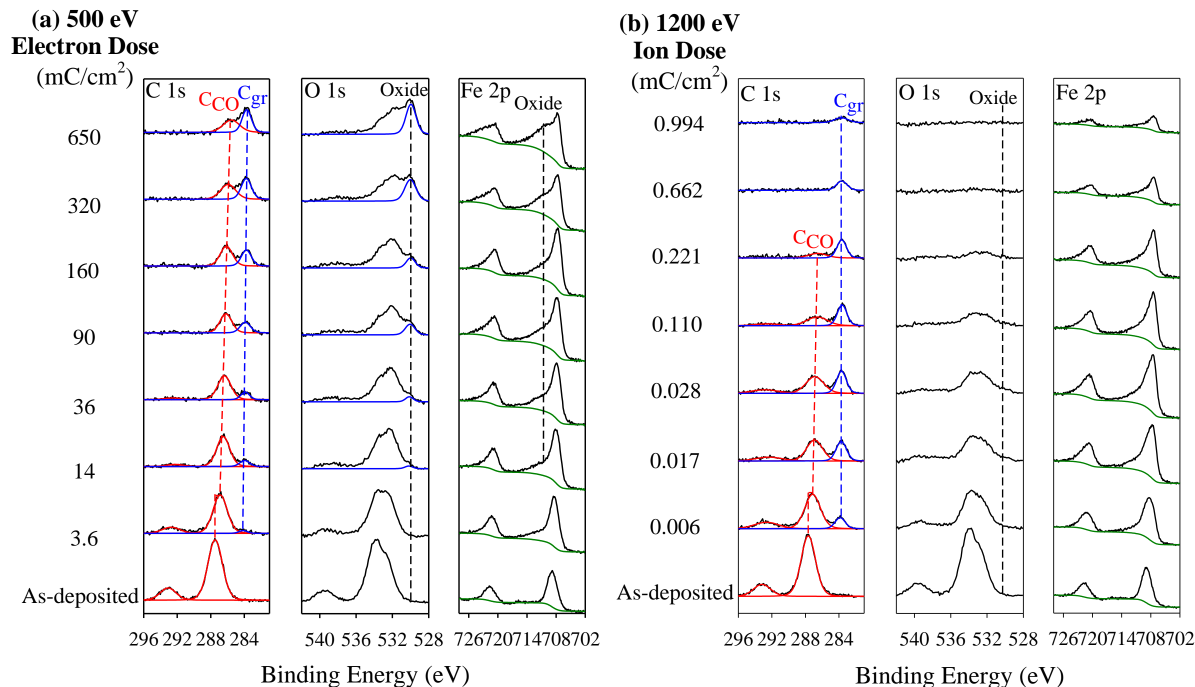

Figure 14. *Evolution of the C(1s), O(1s), and Fe(2p) XPS regions of ~ 1.8 - 2.6 nm thin films of* $Fe(CO)_5$ *upon irradiation with 500 eV electrons (a) and 1200 eV* Ar^+ *ions (b). The bottom spectra represent the as-deposited, un-irradiated film. Speciation is shown in the C(1s) region, where the red line represents the C(1s) peak associated with the precursor carbonyl ligands, while the blue lines represent the C(1s) peak associated with the graphitic carbon species in the deposit. The dashed red and blue lines in these regions show the change in binding energy of these peaks during electron and argon irradiation. The black dashed lines in the O(1s) and Fe(2p) regions indicate oxide growth in (a) and (b). The green curves in the Fe(2p) region show the background. Electron and argon doses are shown in units of* mC/cm^2. *(Adapted figure from [P2])*

Thus, the first regime, for the electron doses < 20 mC/cm^2, is characterized primarily by the loss of CO ligands. This process can be described as:

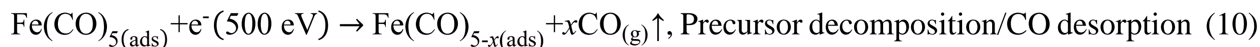

$$Fe(CO)_{5(ads)} + e^-(500\ eV) \rightarrow Fe(CO)_{5\text{-}x(ads)} + xCO_{(g)}\uparrow, \text{ Precursor decomposition/CO desorption} \quad (10)$$

where x is the average number of CO ligands lost in this initial reaction step per $Fe(CO)_5$ molecule in Eq.10.

The second reaction step in the adsorbed $Fe(CO)_5$ films for the electron doses higher than 20 mC/cm^2, is characterized by decomposition of the CO ligands in the partially decarbonylated intermediates. Figure 14a shows no carbon or oxygen removal from the surface in this regime (< 20 mC/cm^2). However, for the electron doses higher than 20 mC/cm^2 (Figure 14a, Figure 15a, and Figure 15b), the residual CO ligands are decomposed into a C_{gr} and a reactive oxygen species

(ROS). The resulting reactive oxygen species oxidize the iron atoms. Hence, the second step of electron-induced reactions can be expressed as:

$$Fe(CO)_{5\text{-}x(ads)} + e^{-}(500\ eV) \rightarrow FeO_{5\text{-}x(ads)} + (5\text{-}x)C_{(graphitic)} \text{ Decomposition of CO ligands} \quad (11)$$

where the oxidized iron product ($FeO_{5\text{-}x(ads)}$) in Eq. 11 represents the adsorbed mixture of iron oxides and unoxidized irons on the surface.

Figure 15c depicts the change in the fractional coverage of carbon (green circles) and oxygen (open circles) atoms as a function of 1200 eV Ar^{+} dose; the fraction change in carbonyl (C̲O) carbon is also shown for carbon (filled red triangles). The trend of fractional change in the total oxygen coverage (open circles) is very similar to the carbonyl carbon atom coverage (filled red triangles). This similar behavior between the fractional change of C̲O and oxygen ($C(CO)/C_0$ vs. O/O_0) indicates that all oxygen-containing species observed during Ar^{+} irradiation are correlated with CO (no oxides, c.f. Figure 14b). Figure 15d demonstrates the fractional coverage of graphitic carbon (open squares) and oxide species (closed light blue squares) and plotted as a function of 1200 eV Ar^{+} dose. Consequent to the ion irradiation, there is a rapid increase in the fractional coverage of graphitic carbon until a maximum value of ~ 0.2 is reached. After an ion dose of 0.028 mC/cm^2, the loss of approximately 60% of the CO groups from the $Fe(CO)_5$ film can be estimated.

Examining Figure 14b, Figure 15c, and Figure 15d together, the ion-induced reactions with adsorbed thin films of $Fe(CO)_5$ might proceed through the two sequential reaction steps:

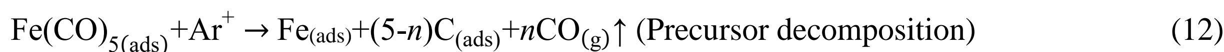

$$Fe(CO)_{5(ads)} + Ar^{+} \rightarrow Fe_{(ads)} + (5\text{-}n)C_{(ads)} + nCO_{(g)}\uparrow \text{ (Precursor decomposition)} \quad (12)$$

$$(5\text{-}n)C_{(ads)} + Fe_{(ads)} + Ar^{+} \rightarrow C_{(g)} + Fe_{(g)} \text{ (Sputtering of deposited atoms)} \quad (13)$$

where n is the average number of CO ligands lost in the initial step. In Eq. 12, an energy transfer from incoming 1200 eV Ar^{+} ions to adsorbed $Fe(CO)_5$ layers leads to complete fragmentation and decomposition of the precursor. Additionally, the desorption of CO and the concurrent loss of peak intensity can be observed in Figure 14b within both the C(1s) and O(1s) signals (carbonyl species). However, some part of the CO ligands undergoes decomposition ($CO_{(ads)} \rightarrow C_{(ads)} + O_{(ads)}$) as opposed to desorption, producing C_{gr}. Regarding the oxygen species

released during ion-induced CO decomposition, these oxygen species desorb and do not oxidize the iron species (Figure 14b).

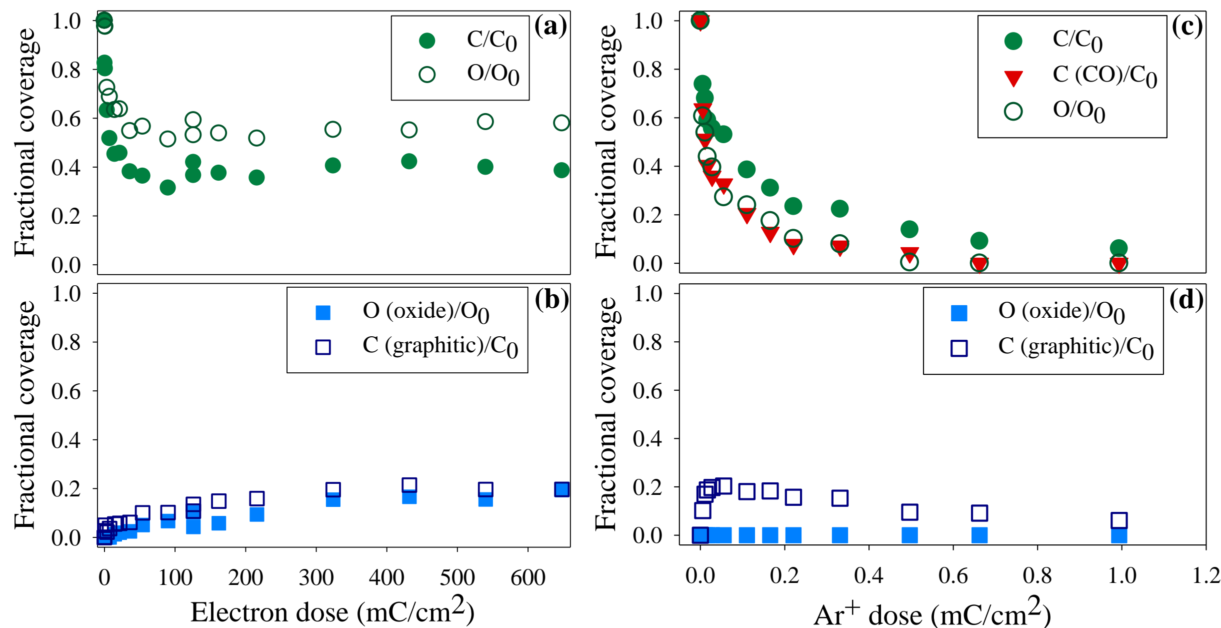

Figure 15. *(a) Fractional coverage of total carbon (light green filled circles) and total oxygen species (dark green open circles), and (b) Change in fractional coverage of graphitic carbon (dark blue open squares) and oxide species (light blue filled squares) for $Fe(CO)_5$ films exposed to 500 eV electrons. (c) Changes in total carbon coverage (green filled circles), carbonyl carbon coverage (filled red triangles) and total oxygen coverage oxygen coverage (green open circles), and (d) fractional coverage of graphitic carbon (dark blue open squares) and oxide species (light blue filled squares) upon exposure of ~ 1.8 nm thin film of $Fe(CO)_5$ to 1200 eV Ar^+. (Adapted figure from [P2])*

The present investigations demonstrate that low energy electron irradiation (500 eV) of $Fe(CO)_5$ films adsorbed at 143 ± 5 K in UHV results in decomposition of precursor and desorption of an average ~2.5 CO ligands per molecule, producing a ~$Fe(CO)_{2.5}$ layer on the substrate. It is worth noting that in the present study, thermal and catalytic reactions of intermediates are hindered by the low (143 ± 5 K) substrate temperature, especially for the comparison with FEBID literature. Contrary to the findings of 500 eV electron irradiation, $Fe(CO)_5$ molecules are subjected to complete fragmentation under low energy (1200 eV) Ar^+ exposure. Ar^+ ion-induced process leads to the desorption of ~4 CO ligands per precursor molecule, wherein one remaining CO ligand undergoes decomposition into the graphitic carbon and reactive oxygen species, which subsequently desorbs for the high ion doses.

3.3 Nanoscale Ruthenium-Containing Deposits from $Ru(CO)_4I_2$ via Simultaneous Focused Electron Beam-Induced Deposition and Etching in Ultrahigh Vacuum: Mask Repair in Extreme Ultraviolet Lithography and Beyond [P3]

One particularly interesting class of precursors are Ru-based organometallic compounds, which gain more and more importance regarding the manufacturing of electronic chips, the building of interconnect wires, and, most importantly for the repair of EUVL masks. Hence, in this chapter, one of the most promising ruthenium-based organometallic compounds has been addressed from literature, $Ru(CO)_4I_2$, using the impact of a tightly focused electron beam from a SEM with the aim of fabricating clean ruthenium nanomaterials in UHV at room temperature without subsequent purification.

The experiments presented in this study were performed at the University of Erlangen-Nürnberg (FAU). The $Ru(CO)_4I_2$ was synthesized by our collaborative partner Prof. Lisa McElwee-White from the University of Florida within the ELENA-ITN Project, who also provided IR results for this compound (Appendix 1).

Using beam parameters of 5 keV and 1.5 nA, 4×4 μm^2 FEBID squares were written. The fabricated FEBID structures were examined with SEM and AES (Figure 16a, Figure 16b, and Figure 16c). The peak at 265 eV and a weak shoulder at 249 eV are attributed to C_{KLL} Auger transitions of carbidic carbon,[164] and the peaks at 468, 483, and 503 eV are assigned to O_{KLL} Auger transitions.[61] After FEBID with 1.56 C/cm^2 electron dose, Auger signals at 200, 231, and 273 eV are analyzed with the Ru_{MNN} transitions,[61] together with the carbidic carbon signal at 249 eV.[164] The characteristic I_{MNN} Auger peaks for iodine are observed at 509 and 519 eV,[61] for the electron doses higher than 1.56 C/cm^2.

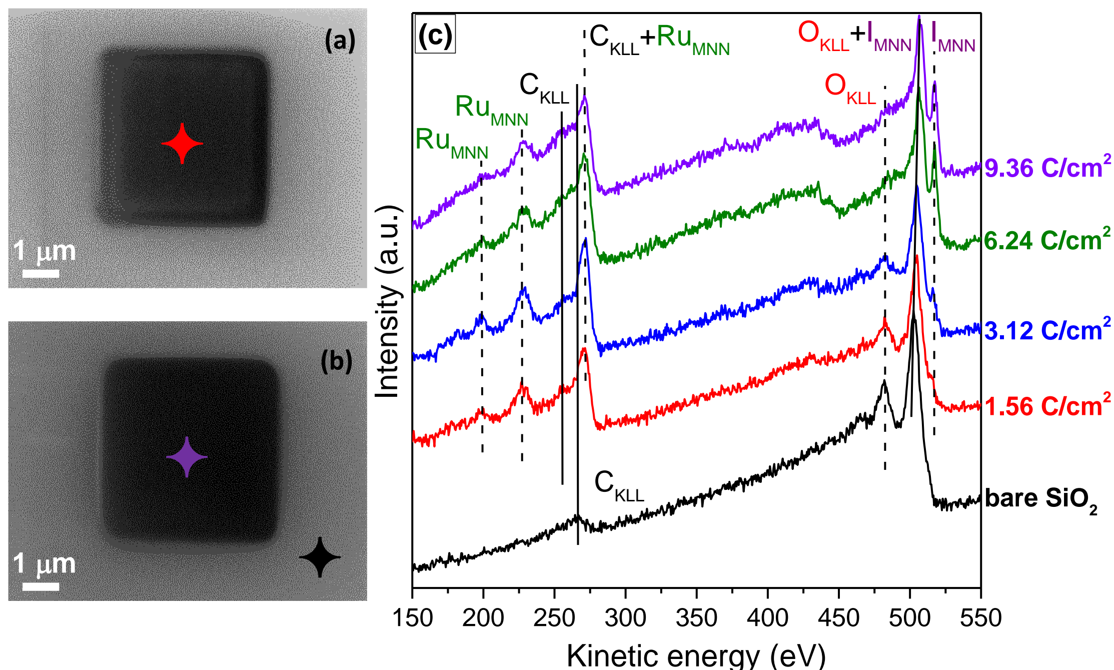

Figure 16. *SEM images of the FEBID structures produced by electron dose of 1.56 C/cm^2 in (a) and electron dose of 9.36 C/cm^2 in (b) at electron beam parameters of 5 keV and 1.5 nA. AES spectra from the bare SiO_2 surface prior to deposition (black line in (c) and black star on the surface) and the results from FEBID structures prepared using electron doses of up to 9.36 C/cm^2. Colored stars in (a) and (b) indicate the positions where the spectra in (c) where acquired. (Original image from [P3] with permission from the ACS Applied Nano Materials.)*

The corresponding AES spectra were plotted “pair-wise” for the Ru/C (Figure 17a) and I/O (Figure 17b) energy regions, due to the obvious overlap of the Ru_{MNN} with the C_{KLL} signals and the I_{MNN} with the O_{KLL} signals (Figure 16c). The C_{KLL} region of the bare SiO_2 surface was fitted using two peaks at 249 and 265 eV (black lines; orange-colored envelope line, $R^2 \geq 0.98$) in Figure 17a. Moreover, the Ru_{MNN} peaks of the FEBID deposits were fitted according to the peak positions at 184, 200, 215, 230, and 273 eV (Figure 17a, green lines).[61]

The O_{KLL} spectrum of the bare SiO_2 substrate was characterized by three peaks at 465, 483, and 503 eV, (Figure 17b, red lines; $R^2 \geq 0.98$). For the FEBID deposits, AES spectra shows a high intensity peak at 503 eV, and an extra small peak at kinetic energy position of 495 eV, which increasing in intensity with increased electron doses. The new peak is assigned to the change from the SiO_2 substrate to O signals related to the dissociation products of RuO_x. Since the Ru signal has already saturated at the highest dose of 9.36 C/cm^2, the spectrum is assumed to compose mainly of the RuO_x signals and partly overlapping iodine signals. The fit results provided the peak

positions for the oxygen contribution at 495, 485, and 472 eV (blue) and for the iodine contribution at 509 and 519 eV (light purple).

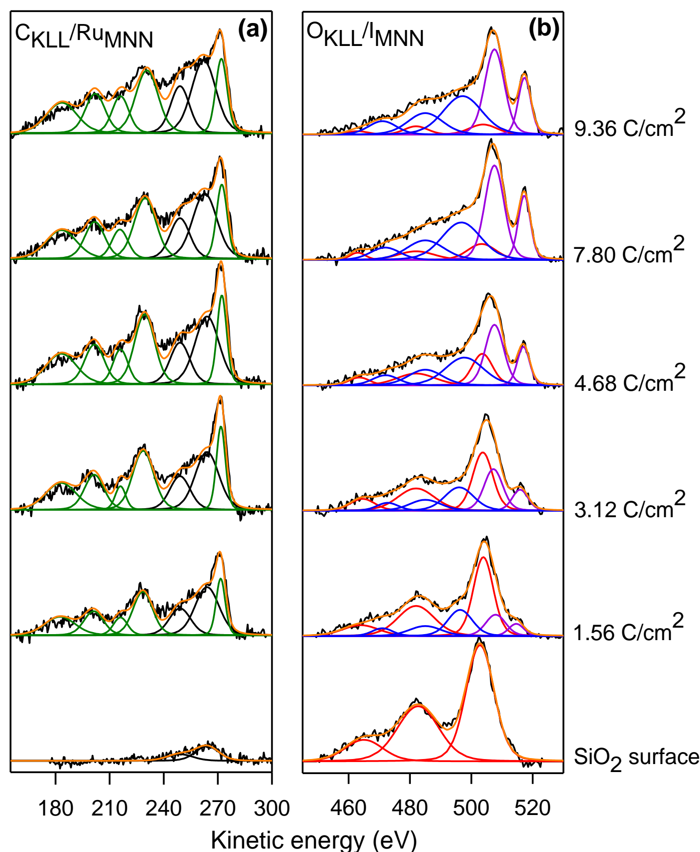

Figure 17. *AES spectra of FEBID structures for selected electron doses (5 keV and 1.5 nA) after subtraction of a linear background. (a)* C_{KLL}/Ru_{MNN} *region, (b)* O_{KLL}/I_{MNN} *region. Deconvoluted peaks are depicted in green for Ru, black for C, red for surface-related O (*SiO_2*), blue for deposition-related O (*RuO_x*), and light purple for I. The fit envelopes are shown in orange, and the raw signals are in black lines. (Original image from [P3] with permission from the ACS Applied Nano Materials.)*

Figure 18 depicts the quantitative analysis of the fit results of the Ru, C, O, and I Auger signals, using the same color code as in Figure 17. Overall, for the electron doses lower than 4.68 C/cm^2, the Ru signals show the most substantial increase, while the iodine signal increases comparably slower than Ru, with the carbon and oxygen signals dropping in between.

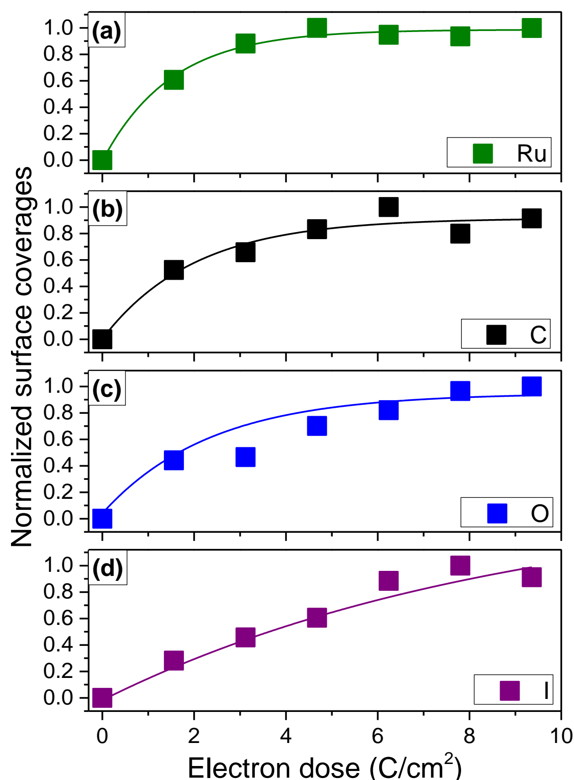

Figure 18. *Quantitative analysis of the relative amounts of deposited (a) ruthenium, (b) carbon, (c) oxygen, and (d) iodine as a function of electron dose (C/cm^2); the lines in the graph serve as a guide to the eye. The signals for each graph are normalized to the signals with the highest intensity. (Original image from [P3] with permission from the ACS Applied Nano Materials.)*

In order to obtain additional information on FEBID and to investigate the reason of iodine behavior depicted in Figure 18, non-contact AFM measurements were performed. Figure 19a, Figure 19b, and Figure 19c depict the 2D AFM images, corresponding height profiles, and 3D AFM images for the FEBID structures for the selected electron doses of 1.56 C/cm^2 (green frames and line), 3.12 C/cm^2 (blue), 4.68 C/cm^2 (pink), 7.80 C/cm^2 (purple), respectively. Surprisingly, the line profiles in Figure 19b for the low electron doses (1.56 and 3.12 C/cm^2) show that the deposit is actually lower than the surface level of the substrate. In Figure 19d, the apparent AFM thickness of the deposits vs. electron dose (orange circles) is plotted; the results prove that up to 6.24 C/cm^{2,} the apparent height is negative, and only for the electron doses higher than 7.80 C/cm^2, a positive apparent height is reached. The detailed analysis of the line profiles in Figure 19b also displays prominent dips/holes at the borders of the deposits, which also indicates the etching process. The depth of the negative dips (etch depths) is plotted in Figure 19d vs. electron dose (open black circles). The holes at the edges might be attributed to the SEII generated by BSEs.[165]

To check this, the radial distribution of BSEs vs. the number of electrons impinging on the SiO_2 substrate is stimulated with the CASINO Monte Carlo Program (V2.42),[129] using the applied beam parameters (5 keV beam with a diameter of 10 nm). In Figure 19e, the radial distribution result is overlaid on top of the blow-up AFM image of Figure 19c (bottom; red-dashed square). The width of the etch dip/hole near the side of the deposited structure agrees very well with the simulated exit radius (~ 0.4 μm) of BSEs.

In Figure 20a, the deposit thicknesses obtained from the AFM (orange circles) and the ones acquired from the attenuation Auger signal of the Si_{MNN} on clean Si (full blue circles) are plotted; the linear relations between the deposit thickness and electron doses are illustrated with blue- and orange-colored lines. Figure 20a also depicts the apparent heights of the FEBID structures on SiO_2 estimated from AFM line scans (open orange circles; same data as in Figure 19d). In Figure 20b, the absolute differences between the heights obtained from expected-heights (AES) and apparent-heights (AFM) were plotted in the same graph (black squares; right vertical scale) with the Ru

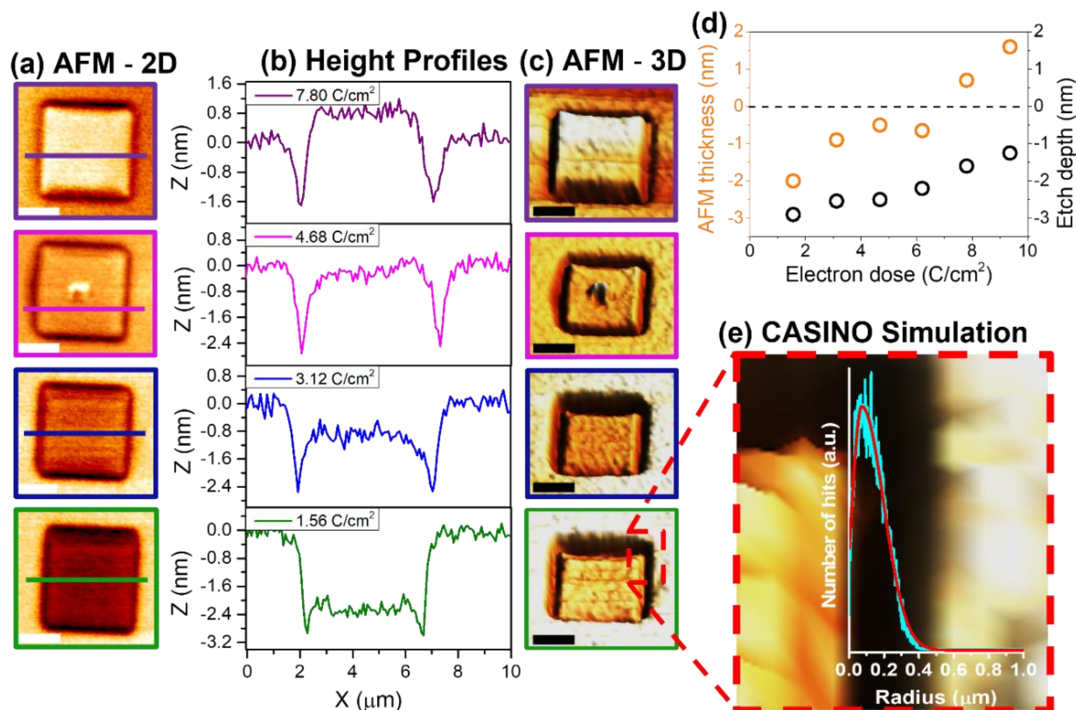

Figure 19. *(a) 2D AFM images, (b) corresponding line profiles, and (c) 3D AFM images for the FEBID structures produced with electron doses of 1.56 C/cm² (green lines and frames), 3.12 C/cm² (blue), 4.68 C/cm² (pink) and 7.80 C/cm² (purple). (d) The thickness of FEBID structures from AFM versus the height of the negative dips. (e) Magnified AFM image superimposed with the simulation of the BSE exit radius (raw data: cyan; fit: red) obtained with the CASINO Monte Carlo Program. (Original image from [P3] with permission from the ACS Applied Nano Materials.)*

surface coverage from Figure 18a (green squares; left vertical scale). From this figure, it is obvious that first, an etching process occurs along with the deposition process, and then the increased amount of Ru surface coverage goes along with reduced etching.

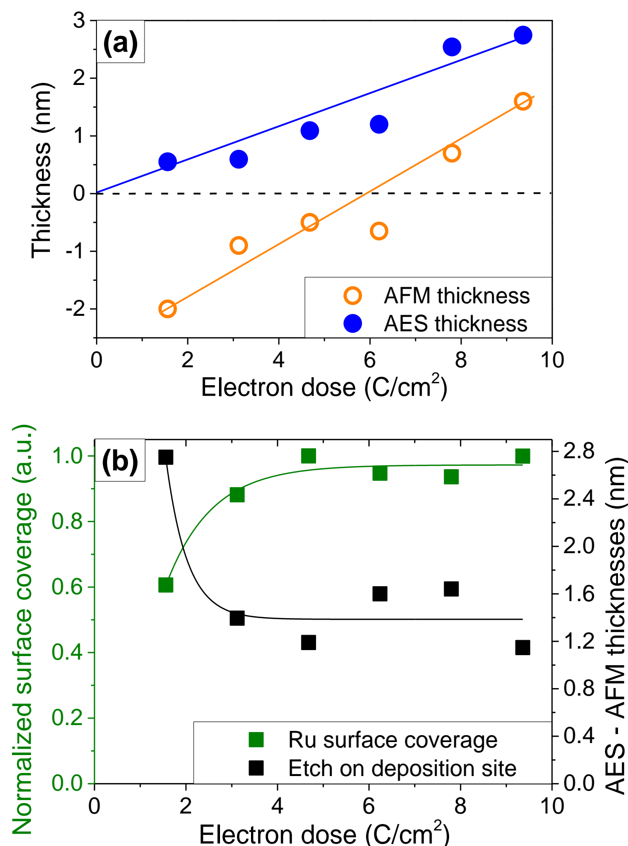

Figure 20. *(a) The expected thickness of the FEBID structures vs electron dose obtained from AES (blue full circles) compared to the apparent thickness obtained from AFM line scans (orange open circles). (b) The difference between expected and apparent heights (black full squares) vs electron dose compared with the Ru surface coverage (green full squares) from Figure 18a. The lines depicted in each graph serve as a guide to the eye. (Original image from [P3] with permission from the ACS Applied Nano Materials.)*

According to the acquired data, the underlying mechanism for simultaneous etching/FEBIE and deposition/FEBID must stay uncertain. Nevertheless, it is suggested that the iodine act as an etchant by forming volatile products (SiI_x) with surface silicon atoms. The electron-induced surface activation of SiO_2 to SiO* or Si* might provide for the formation of the volatile species in this proposed scenario. On the other hand, the remaining Ru and carbonyl species of the precursor molecule are likely to contribute to the electron-induced deposition, which happens simultaneously with the etching process. Therefore, an increased amount of deposited Ru can deactivate the active sites on the surface (SiO* or Si*) and prevents further etching. In this regard, the electron dose

plays an important role, where the Ru coverage increases with increasing electron dose and suppresses the simultaneous etching process for high electron doses.

The compositions of FEBID structures produced with different electron doses on SiO_2 were calculated according to the Eq. 4 described in Chapter 2.1.2. The calculated percentages of atoms for the e^- doses of 1.56 and 3.12 C/cm^2 exhibit around 56 at.% Ru, 16 at.% I, 18 at.% C and 10 at.% O. The Ru content decreases by ~11 at.% for the electron doses lower than 7.80 C/cm^2, and the I content increases by ~11 at.%, while C and O contents stay almost constant. For the low electron doses, higher Ru content and lower I content are attributed to the iodine consumption during the etching process. For the higher electron doses ($\geq$ 7.80 C/cm^2), Ru contents of 45-46 at.% using the deposition parameters of 5 keV and 1.5 nA are obtained, which is significantly higher than reported in the literature (31 at.% Ru) so far.[145] This Ru content can be further improved up to 52 at.% on sputtered clean Si substrate (carbon- and oxygen-free) by lowering the beam energy to 3 keV (all other parameters kept constant, Figure 21). The chemical composition and the thickness of the deposits were determined using Auger spectroscopy (Figure 21b). The SAM image in Figure 21c provides evidence of a selectively deposited structure only in the irradiated region with significant amounts of Ru.

Based on the investigations obtained from this study, the deposits have a negative apparent height due to the competition between FEBID and FEBIE at low electron doses. The peculiarity of the $Ru(CO)_4I_2$ (metal-carbonyl-halide) precursor is that it combines the properties for both etching and deposition. This combined process might open the fabrication pathway to a new type of 3D nanostructured materials, and also using a deposit with a negative apparent height could expend the applications of buried nanostructures and buried contacts.

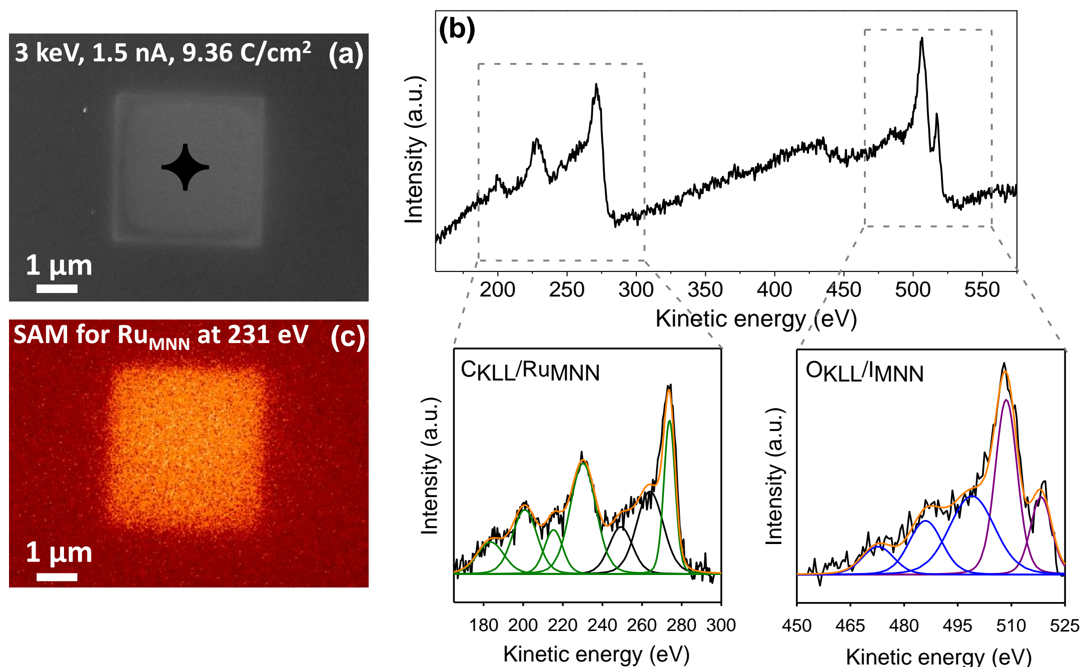

Figure 21. a) SEM image of FEBID structure under an electron dose of 9.36 C/cm^2. The black star represents the point at which spectra were acquired. B) local AES of the deposition from (a) and fitted regions for C_{KLL}/Ru_{MNN} and O_{KLL}/I_{MNN} depicted with dashed grey lines, c) SAM from FEBID structure for the Ru_{MNN} peak at 231 eV. (Original image from [P3] with permission from the ACS Applied Nano Materials.)

3.4 On the electron-induced reactions of $(CH_3)AuP(CH_3)_3$: A combined UHV surface science and gas-phase study [P4]

This study continues to explore the potential of one of the most promising gold precursors reported in literature[166, 167] for our UHV-FEBID setup. Hence, the MS, FEBID, and AES experiments presented in this study were performed at the University of Erlangen-Nürnberg (FAU). The $(CH_3)AuP(CH_3)_3$ precursor was synthesized by the group of Prof. Sjoerd Harder from FAU, who also provided ^{1}H NMR data for this compound (Appendix 2). Gas-phase studies were performed at the University of Iceland through the group of Prof. Oddur Ingólfsson within the framework of the ELENA-ITN project.

To understand the volatility and the stability of the precursor prior to the FEBID experiment, the $(CH_3)AuP(CH_3)_3$ was delivered to the UHV chamber via the gas-injection system (GIS) at

room temperature, and the fragmentations of the compound were monitored via MS (Chapter 2.3.4).

The $(CH_3)AuP(CH_3)_3$ precursor dosage was adjusted for deposition such that a chamber pressure of 1.3×10^{-7} mbar was achieved (local pressure at the sample: ~ 4.0×10^{-6} mbar; see Chapter 2.2.1). Using the acceleration voltage of 5 keV and a comparably high beam current of 3 nA, 4×4 μm^2 FEBID squares were written. Figure 22a and Figure 22b depict SEM images of the FEBID deposits created with electron exposures of 4.68 and 7.80 C/cm^2, respectively. The centers of these rectangles are marked by green- and blue-colored stars in the corresponding SEM image (Figure 22a and Figure 22b, respectively). On the pristine SiO_2 surface (black spectrum), only two AES elements are noticeable, oxygen and carbon. The low intensity peak at 272 eV is attributed to C_{KLL} Auger transitions of carbon,[164] and the pronounced peaks at 468, 483, and 503 eV are assigned to O_{KLL} Auger transitions of SiO_2.[61] After deposition with 4.68 C/cm^2 electron dose, the O_{KLL} Auger transitions of SiO_2 vanishes and AES signals appear at kinetic energies of 69, 120, and 265 eV, and are assigned to Au_{NOO}, P_{LMM}, and C_{KLL} transitions,[61] respectively (Figure 22c, green and blue spectra). The atomic concentrations of the FEBID structures shown in Figure 22a and Figure 22b are calculated (c.f. Eq. 4) as to be 31 at.% Au, 67 at.% C, (green spectrum) and 2 at.% P, and 34 at.% Au, 65 at.% C, and 1 at.% P, (blue spectrum), respectively. These results were compared with a previously published HV-FEBID study investigating the same precursor ($(CH_3)AuP(CH_3)_3$), which suggested that the removal of one single CH_3 ligand as a reaction pathway, resulting in 19-25 at.% Au, 54-62 at.% C, 12-16 at.% P and 2−7 at.% O from $CH_3AuP(CH_3)_3$ characterized by EDX spectroscopy.[167] However, according to the calculated AES results in our study, the effective removal of $P(CH_3)_3$ ligand during the deposition is evident from the low phosphorus content, and a ratio of the 1:2 Au:C composition suggests a dissociation of dimethyl-phosphine group from the precursor.

Dissociation step of dimethyl-phosphine group may proceed further with the decomposition and co-deposition of carbon from dissociating $P(CH_3)_3$ ligands or in an electron-induced rearrangement reaction such as: (Note: This is a suggested reaction mechanism; therefore, it is not meant to be balanced.)

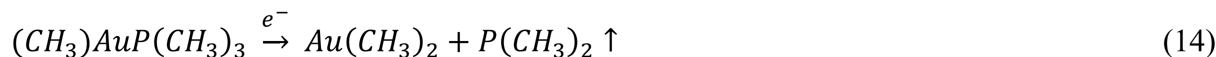

$$(CH_3)AuP(CH_3)_3 \xrightarrow{e^-} Au(CH_3)_2 + P(CH_3)_2 \uparrow \quad (14)$$

where $Au(CH_3)_2$ is the deposited species in Eq. 14, and $P(CH_3)_2$ is the volatile part that is pumped away from the system.

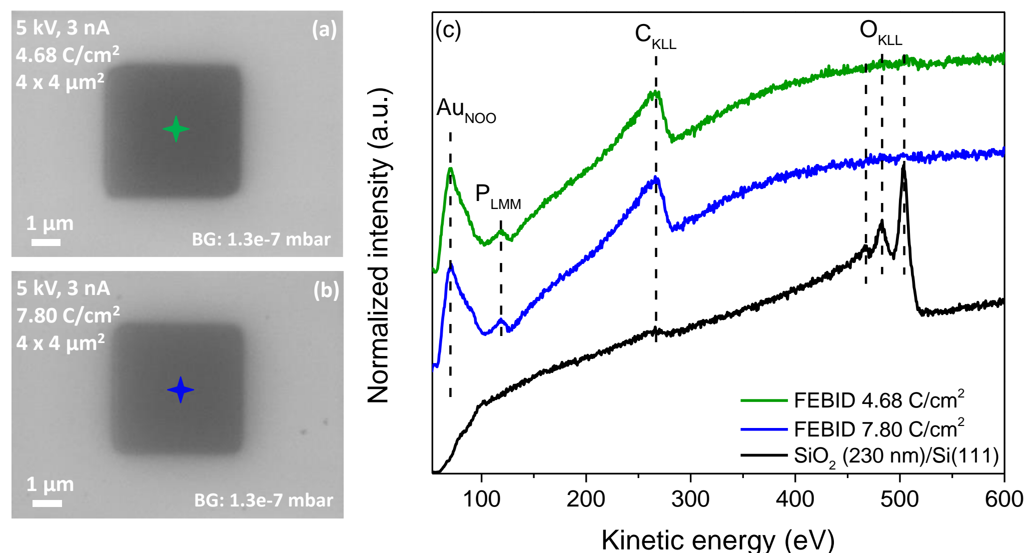

Figure 22. *a) SEM image of the 4 x 4 µm² FEBID structures deposited on SiO_2 from $CH_3AuP(CH_3)_3$ by electron doses of 4.68 C/cm² and 7.80 C/cm² at electron beam parameters of 5 keV and 3 nA, and b) AES from the SiO_2 substrate prior to deposition (black line) and the result from FEBID structures (green and blue lines). The colored stars in (a) and (b) indicate the position where the spectra were acquired. (Original image from [P4], published by Nanomaterials under the terms and conditions of open access CC BY license.)*

In the FEBID experiments, the deposit is formed mostly by the interactions of the adsorbed precursor molecules with the primary-, backscattered-, and secondary-electrons. To further explore these electron-matter interactions, a comprehensive gas phase study was conducted, in which the average carbon and phosphor loss per DI incident were compared. This was realized in a cooperative effort with the University of Iceland (Prof. Dr. Oddur Ingólfsson) within the ELENA-ITN Project, i.e., the fragmentations of isolated $(CH_3)AuP(CH_3)_3$ precursor molecules under low energetic electrons were studied further.

The results obtained from the isolated gas-phase study (Refer [P4]) indicate that the average carbon loss observed in the gas phase DI experiments agrees well with the current UHV FEBID experiments, where it is also found to be close to 1:2 with respect to Au:C. Considering the

complete loss of phosphor in UHV-FEBID, the average phosphor loss per DI in the gas phase experiments is found to be 0.8; hence in 20% of the DI incidents, the Au-P bond stays intact. This is principally ascribed to the stability of the $AuP(CH_3)_3^+$ ion in the gas phase, i.e., loss of the methyl group directly attached to the central gold atom. Furthermore, the close to 1:2 Au:C ratio of the deposit reveals that the neutral $(CH_3)_2Au$ fragmentation characteristic for the $P(CH_n)_2^+$ loss channels in DI are dominating in the electron-induced decomposition of $(CH_3)AuP(CH_3)_3$ at the SiO_2 surface. Overall, the potential deposition mechanism pictured by the gas-phase study is found to be in good agreement with the proposed reaction mechanism depicted in Eq. 14.

4 Summary

The thesis at hand focuses on the fundamental reactions initiated by low energetic electrons and ions on different organometallic precursors adsorbed on surfaces and the search for highly promising precursors for FEBIP. In order to gain a fundamental understanding of the corresponding surface reactions, *in situ* XPS, MS, electron flood gun, and argon sputter gun were used under UHV conditions in the first and second part of the result section. In the third and fourth parts of the result section, new and promising precursors were tested and used to create FEBID deposits. Detailed characterization of the fabricated structures and the processes were performed using SEM, AES, MS, SAM, and AFM.

The first part of the result section focuses on the primary ion-induced reactions triggered by low energetic argon ions on a thin adsorbed $Ru(CO)_4I_2$ layer to comprehend the fundamental steps in FIBID. During the FIBID experiment, the deposition can be described by complex reactions due to both inelastic and elastic collisions between energetic ions with the atoms and electrons in the solid. The collisions can result in different processes such as backscattering, sputtering, ion-implantation, and ion-induced deposition. This study, using a very thin adsorbed $Ru(CO)_4I_2$ layer, provides information mainly from the ion-induced decomposition and from the physical sputtering process. The type of ion (Ar^+) and the ion energy (860 eV) were held constant while the Ar^+ dose was varied. The subsequent steps due to the ion-induced reactions in terms of decomposition and sputtering processes were identified using XPS. First, the adsorbed molecular precursor is decomposed into a metal-containing deposit layer. Thereafter, the decomposition step is accompanied by the desorption of all the CO ligands with the production of RuI_2. For the ions doses between 0.036 and 0.072 mC/cm^2, sputtering of iodine is initiated, leading to reduced Ru metal. Due to the highly sequential nature of ion-induced reactions with $Ru(CO)_4I_2$, a kinetic model could be derived and applied to understand the reaction rates for each step. The latter revealed that the desorption step occurs as five times faster than the sputtering step. The reported results provide valuable insights into the possible reaction mechanism, which plays an essential role in ion beam-induced deposition.

After gaining deeper insights into the ion-induced reactions, the ion-induced and electron-induced reactions were compared using a well-investigated organometallic complex, $Fe(CO)_5$, in the second part of the result section (Chapter 3.2). The results obtained using low energy (500 eV) electrons evidenced that very thin adsorbed $Fe(CO)_5$ layers (1.8-2.6 nm) first decompose, followed

by both desorption of ~2.5 CO ligands in average and partial decarbonylation (formation of C_{gr}) in the film. At higher electron doses (> 20 mC/cm^2), where the decarbonylated deposits undergo CO decomposition, iron oxides in a graphitic carbon film were formed. However, during the Ar^+ irradiation, due to the energy transfer from the incoming ions, $Fe(CO)_5$ molecules dissociate and result in the desorption of approximately 4 CO ligands. The remaining single CO undergoes cleavage of the carbon-oxygen bond, producing adsorbed carbon and volatile oxygen species. The reason why oxygen is defined here as volatile is that the formation of iron oxide was not observed. At higher Ar^+ doses, the remaining iron and carbon atoms are exposed to physical Ar^+ ion sputtering. The implications of 1200 eV Ar^+- and 500 eV electron-induced reactions for FIBID and FEBID with $Fe(CO)_5$ are also expected to provide insights into a possible reaction mechanism.

The $Ru(CO)_4I_2$ complex investigated in Chapter 3.2 was never used for a FEBID approach prior to the study at hand. However, in literature, the latter Ru-complex yielded promising results using a non-focused electron beam (EDX; 32 at.% Ru) and isolated gas-phase study.[145] In the study at hand, the precursor was heated to 340-345 K, and FEBID experiments were performed in the precursor-limited regime on SiO_2 and sputtered clean Si substrates. AES along with extensive fitting procedures not only revealed the elemental composition but also enabled the estimation of the thickness of the produced deposits. It was demonstrated that at low electron doses (< 4.68 C/cm^2), up to 56% Ru content can be obtained; however, at higher electron doses, the ruthenium content drops to 45%, and the iodine content increases simultaneously. The initial low iodine content was attributed to the simultaneous etching process (FEBIE), which was found to compete with the deposition. The etching process was observed by atomic force microscopy, where the deposits displayed a negative apparent height for low electron doses (< 6.24 C/cm^2). At higher electron doses, the deposits have a positive apparent height. Therefore, the etching process becomes less pronounced as the ruthenium surface coverage increases at higher electron doses. Given the high Ru content and the correlation between electron-induced deposition and etching, this study has the potential to expand the engineering possibilities of nanostructured materials significantly. In future work, it would be very interesting to see whether etching also occurs on Si and compare the obtained results.

In the final part of the results section (Chapter 3.4), the analysis of FEBID deposits using $(CH_3)AuP(CH_3)_3$, one of the new precursors tested for UHV-based FEBID device, indicates that this complex is suitable for UHV-FEBID experiments at room temperature. Based on the UHV-

FEBID experiments and corresponding AES analysis (31-34 at.% Au, 67-65 at.% C, and 2-1 at.% P), the reaction mechanism was proposed as dissociation of $[HP(CH_2)(CH_3)]^+$ fragment and the deposition of $(CH_3)_2Au$ on the substrate surface. The exact ratios between Au/C and Au/P from UHV-FEBID experiments were then calculated as 1/2.16 and 1/0.06, respectively, where one might assume the complete loss of phosphor ligand. The gas-phase study results also indicate the atomic ratios of 1/2.1 for Au/C and 1/0.2 for Au/P in the precursor molecule, respectively, per dissociation incident. The Au/C ratios are found to be comparably similar in both UHV-FEBID and gas-phase studies, which suggests that the neutral $(CH_3)_2Au$ fragmentation characteristic for the $P(CH_n)_2^+$ loss channels in per dissociative ionization (DI) incident are dominating in the electron-induced decomposition of $(CH_3)AuP(CH_3)_3$ at the SiO_2 surface. However, the P-based atomic concentration obtained from the UHV-FEBID study is roughly three times lower than that obtained in the gas phase. Therefore, the remaining phosphor per DI incident in the gas phase can be attributed to the loss of the CH_3—Au methyl group and the formation of $AuP(CH_3)_2^+$. This reaction channel is found to be not active in the UHV-FEBID of $(CH_3)AuP(CH_3)_3$ on SiO_2.

In summary, the present study advances the nanostructuring techniques FEBID, FEBIE and FIBID by yielding novel detailed insights into the interactions of energetic charged particles with precursor molecules and the identification of novel high potential precursors.

5 Zusammenfassung

In der vorliegenden Arbeit werden Reaktionen von oberflächenadsorbierten metallorganischen Precursoren mit niederenergetische Elektronen und Ionen detailliert untersucht. Ein wichtiges Ziel ist dabei die Suche nach potenten Precusoren für FEBID-Prozesse. Um ein grundlegendes Verständnis der entsprechenden Oberflächenreaktionen zu erlangen, wurden im ersten und zweiten Ergebnisteil *in situ* XPS, MS, Elektronenflutkanone und Argon-Ionenbeschuss unter UHV-Bedingungen eingesetzt. Im dritten und vierten Teil des Ergebnisteils wurden neue und vielversprechende Precursoren getestet und zur Erzeugung von FEBID-Abscheidungen verwendet. Die erzielten Ergebnisse wurden mittels SEM, AES, MS, SAM und AFM charakterisiert.

Der erste Teil des Ergebnisteils konzentriert sich auf die primären ioneninduzierten Reaktionen, die durch niederenergetische Argon-Ionen auf einer dünnen adsorbierten $Ru(CO)_4I_2$ Schicht ausgelöst werden, um die grundlegenden Schritte bei FIBID zu verstehen. Während des FIBID-Experiments kann die Abscheidung durch komplexe Reaktionen beschrieben werden, die durch inelastische und elastische Stöße zwischen energetischen Ionen und den Atomen und Elektronen im Festkörper ausgelöst werden. Die Kollisionen können zu verschiedenen Prozessen wie Rückstreuung, Sputtern, Ionenimplantation und ioneninduzierter Abscheidung führen. Diese Untersuchung, bei der eine sehr dünne, adsorbierte $Ru(CO)_4I_2$ Schicht verwendet wird, liefert Informationen über die ioneninduzierte Zersetzung und über den physikalischen Sputterprozess. Die Art des Ions (Ar^+) und die Ionenenergie (860 eV) wurden konstant gehalten, während die Dosis von Ar^+ variiert wurde. Die aufeinanderfolgenden Schritte, die auf die ioneninduzierten Reaktionen in Form von Zersetzungs- und Sputterprozessen zurückzuführen sind, wurden mithilfe von XPS ermittelt. Zunächst wird der adsorbierte molekulare Precursor chemisch modifiziert/dissoziiert und in einer metallhaltigen Schicht abgeschieden. Es folgt die Desorption aller CO-Liganden und die Bildung von RuI_2. Bei Ionendosen zwischen 0.036 und 0.072 mC/cm^2 wird der Abtragungsprozess (Sputtering) von Jod beobachtet, welcher ein reduziertes Ru-Metall zurücklässt. Da die ioneninduzierten Reaktionen mit $Ru(CO)_4I_2$ in sequentiell ablaufen, konnte ein kinetisches Modell abgeleitet und angewandt werden, um die Reaktionsraten für jeden Schritt zu ermitteln. Es zeigte sich, dass der Desorptionsschritt fünfmal schneller abläuft als der Sputtering-Schritt. Diese Ergebnisse liefern wertvolle Einblicke in den möglichen Reaktionsmechanismus, der bei der ionenstrahlinduzierten Abscheidung eine wesentliche Rolle spielt.

Nachdem wichtige Erkenntnisse über die ioneninduzierten Reaktionen gewonnen wurden, werden in Kapitel 3.2 die ionen- und elektroneninduzierten Reaktionen anhand des bekannten metallorganischen Komplexes $Fe(CO)_5$ untersucht. Die mit niederenergetischen (500 eV) Elektronen erzielten Ergebnisse zeigten, dass sich sehr dünne adsorbierte $Fe(CO)_5$ Schichten (1.8-2.6 nm) zuerst zersetzen, gefolgt von der Desorption von ~2.5 CO-Liganden und einer teilweisen Decarbonylierung (Bildung von C_{gr}) im Film. Bei höheren Elektronendosen (> 20 mC/cm^2) zersetzen sich die dekarbonylierten Ablagerungen in CO und bilden Eisenoxide in einem graphitischen Kohlenstofffilm. Während der Ar^+-Bestrahlung dissoziieren aufgrund des Energietransfers der einfallenden Ionen die $Fe(CO)_5$ -Moleküle und führen zur Desorption von etwa 4 CO-Liganden. Der verbleibende einzelne CO Ligand wird im weiteren in Kohlen- und Sauerstoff dissoziiert, wodurch adsorbierter Kohlenstoff und flüchtige Sauerstoffspezies entstehen. Sauerstoff wird hier als flüchtig angesehen, da keine Bildung von Eisenoxid beobachtet wurde. Bei den hohen Ar^+ Dosen sind die verbleibenden Eisen- und Kohlenstoffatome des physikalischen Ar^+ Sputterns ausgesetzt. Die Implikationen von 1200 eV Ar^+- und 500 eV elektroneninduzierten Reaktionen für FIBID und FEBID mit $Fe(CO)_5$ sollen auch Einblicke in einen möglichen Reaktionsmechanismus geben.

Der Komplex $Ru(CO)_4I_2$ wurde in der in Kapitel 3.2 beschriebenen Studie erstmals für FEBID verwendet. In der Literatur wurde ein vielversprechendes Ergebnis mit EBID unter Verwendung eines nicht fokussierten Elektronenstrahls (EDX; 32 at.% Ru) und einer isolierten Gasphasenstudie gezeigt.[145] In der vorliegenden Untersuchung wurde der Precursor auf 340-345 K erhitzt, und FEBID-Experimente wurden im Precursor-begrenzten Bereich auf SiO_2 und gesputterten sauberen Si-Substraten durchgeführt. Mit Hilfe von AES mit umfangreichen Fit-Prozeduren konnte nicht nur die Elementzusammensetzung, sondern auch die Dicke der erzeugten Ablagerungen bestimmt werden. Es zeigte sich, dass bei niedrigen Elektronendosen (< 4.68 C/cm^2) ein Ru-Gehalt von bis zu 56% erreicht werden kann; bei höheren Elektronendosen sinkt der Ruthenium-Gehalt jedoch auf 45%, während der Jod-Gehalt gleichzeitig steigt. Der anfänglich niedrige Jodgehalt wurde auf den gleichzeitigen Ätzprozess (FEBIE) zurückgeführt, der mit der Abscheidung konkurriert. Der Ätzprozess wurde mittels Rasterkraftmikroskopie beobachtet, wobei die „Ablagerungen“ bei niedrigen Elektronendosen (< 6.24 C/cm^2) eine negative scheinbare Höhe aufwiesen. Bei höheren Elektronendosen sind die Ablagerungen dann, wie für FEBID zu erwarten, erhaben, weisen alo eine positive Höhe auf. Der Ätzprozess ist damit weniger

ausgeprägt, wenn die Ruthenium-Oberflächenbedeckung bei höheren Elektronendosen zunimmt. Angesichts des hohen Ru-Gehalts und des Zusammenhangs zwischen elektroneninduzierter Abscheidung und Ätzung hat diese Studie das Potenzial, die technischen Möglichkeiten zur Erzeugung nanostrukturierter Materialien erheblich zu erweitern. In zukünftigen Arbeiten wäre es sehr interessant zu sehen, ob das Ätzen auch auf Si auftritt und die erhaltenen Ergebnisse zu vergleichen.

Im letzten Teil der vorliegenden Arbeit (Kapitel 3.4) zeigt die Analyse von FEBID-Abscheidungen aus dem neuen Precursor $(CH_3)AuP(CH_3)_3$, dass dieser Komplex für UHV-FEBID-Experimente bei Raumtemperatur sehr geeignet ist. Ausgehend von den UHV-FEBID-Experimenten und den daraus resultierenden AES-Ergebnissen (31-34 at.% Au, 67-65 at.% C und 2-1 at.% P) wird der FEBID-Reaktionsmechanismus dieses Precursors als Dissoziation des Fragments $[HP(CH_2)(CH_3)]^+$ und Abscheidung von $(CH_3)_2$ Au auf der Substratoberfläche vorgeschlagen. Die genauen Verhältnisse zwischen Au/C und Au/P aus UHV-FEBID-Experimenten wurden dann als 1/2.16 bzw. 1/0.06 berechnet, wobei man von einem vollständigen Verlust des Phosphor-Liganden ausgehen kann. Die Ergebnisse der Gasphasenuntersuchung deuten ebenfalls auf das Vorhandensein eines Atomverhältnisses von 1/2.1 bzw. 1/0.2 für Au/C und Au/P im Precursormolekül pro Dissoziationsereignis hin. Die Au/C-Verhältnisse sind sowohl in UHV-FEBID- als auch in Gasphasenstudien ähnlich, was darauf hindeutet, dass die neutrale $(CH_3)_2$ Au-Fragmentierung, die für die $P(CH_n)_2^+$ Verlustkanäle pro dissoziativem Ionisierungsereignis (DI) charakteristisch ist, bei der elektroneninduzierten Zersetzung von $(CH_3)AuP(CH_3)_3$ an der SiO_2 Oberfläche dominiert. Die in der UHV-FEBID-Studie ermittelte P-Atomkonzentration ist etwa dreimal geringer als die in der Gasphase ermittelte. Daher kann der verbleibende Phosphor pro DI in der Gasphase auf den Verlust der CH_3-Au-Methylgruppe und die Bildung von $AuP(CH_3)_2^+$ zurückgeführt werden. Dieser Reaktionskanal ist im UHV-FEBID von $(CH_3)AuP(CH_3)_3$ auf SiO_2 nicht aktiv.

Zusammenfassend kann festgestellt werden, dass die vorliegende Arbeit wesentliche Erkenntisse bzgl. Wechselwirkungen zwischen geladenen Teilchen und Precursomolekülen liefert und neue Precursoren mit hohem Anwendungspotential identifiziert wurden. Damit sind die Erkenntnisse geeignet die Entwicklung der Nanostrukturierungstechniken FEBID, FEBIE und FIBID voranzutreiben.

6 Literature

1. Feynman, R., There's Plenty of Room at the Bottom. In *Feynman and Computation*, CRC Press: 2018; pp 63-76.

2. Newman, T.; Williams, K. E.; Pease, R., High Resolution Patterning System with a Single Bore Objective Lens. *J. Vac. Sci. Technol., B: Microelectron. Process. Phenom.* **1987,** *5* (1), 88-91.

3. Everhart, T. E.; Thornley, R., Wide-Band Detector for Micro-Microampere Low-Energy Electron Currents. *J. Sci. Instrum.* **1960,** *37* (7), 246.

4. Binnig, G.; Rohrer, H.; Gerber, C.; Weibel, E., Surface Studies by Scanning Tunneling Microscopy. *Phys. Rev. Lett.* **1982,** *49* (1), 57.

5. Antognozzi, M.; Bermingham, C.; Harniman, R.; Simpson, S.; Senior, J.; Hayward, R.; Hoerber, H.; Dennis, M.; Bekshaev, A.; Bliokh, K., Direct Measurements of the Extraordinary Optical Momentum and Transverse Spin-Dependent Force Using a Nano-Cantilever. *Nat. Phys.* **2016,** *12* (8), 731-735.

6. Cvelbar, U.; Ostrikov, K.; Drenik, A.; Mozetic, M., Nanowire Sensor Response to Reactive Gas Environment. *Appl. Phys. Lett.* **2008,** *92* (13), 133505.

7. Low, J.; Yu, J.; Ho, W., Graphene-Based Photocatalysts for CO_2 Reduction to Solar Fuel. *J. Phys. Chem. Lett* **2015,** *6* (21), 4244-4251.

8. Hashim, D. P.; Narayanan, N. T.; Romo-Herrera, J. M.; Cullen, D. A.; Hahm, M. G.; Lezzi, P.; Suttle, J. R.; Kelkhoff, D.; Munoz-Sandoval, E.; Ganguli, S., Covalently Bonded Three-Dimensional Carbon Nanotube Solids via Boron Induced Nanojunctions. *Sci. Rep.* **2012,** *2* (1), 1-8.

9. Freitas Jr, R. A., What is Nanomedicine? *Nanomed.: Nanotechnol. Biol. Med.* **2005,** *1* (1), 2-9.

10. Sekhon, B. S., Food Nanotechnology–An Overview. *Nanotechnol. Sci. Appl.* **2010,** *3*, 1.

11. Tiwari, J. N.; Tiwari, R. N.; Kim, K. S., Zero-Dimensional, One-Dimensional, Two-Dimensional and Three-Dimensional Nanostructured Materials for Advanced Electrochemical Energy Devices. *Prog. Mater. Sci.* **2012,** *57* (4), 724-803.

12. Thompson, L. F., An Introduction to Lithography. ACS Publications: 1983; pp 1-13.

13. Sreenivasan, S., Nanoimprint Lithography Steppers for Volume Fabrication of Leading-Edge Semiconductor Integrated Circuits. *Microsyst. Nanoeng.* **2017,** *3* (1), 1-19.

14. Garner, C. M., Lithography for Enabling Advances in Integrated Circuits and Devices. *Philos. Trans. R. Soc., A* **2012,** *370* (1973), 4015-4041.

15. Worschech, L.; Hartmann, D.; Reitzenstein, S.; Forchel, A., Nonlinear Properties of Ballistic Nanoelectronic Devices. *J. Phys. Condens. Matter* **2005,** *17* (29), R775.

16. Chen, Y., Nanofabrication by Electron Beam Lithography and Its Applications: A Review. *Microelectron. Eng.* **2015,** *135*, 57-72.

17. Hudek, P.; Beyer, D., Exposure Optimization in High-Resolution E-Beam Lithography. *Microelectron. Eng.* **2006,** *83* (4-9), 780-783.

18. Tseng, A. A.; Chen, K.; Chen, C. D.; Ma, K. J., Electron Beam Lithography in Nanoscale Fabrication: Recent Development. *IEEE Trans. Compon. Packaging Manuf. Technol.* **2003,** *26* (2), 141-149.

19. Hu, W.; Sarveswaran, K.; Lieberman, M.; Bernstein, G. H., Sub-10 nm electron beam lithography using cold development of poly (methylmethacrylate). *Journal of Vacuum Science & Technology B: Microelectronics and Nanometer Structures Processing, Measurement, and Phenomena* **2004,** *22* (4), 1711-1716.

20. Manfrinato, V. R.; Zhang, L.; Su, D.; Duan, H.; Hobbs, R. G.; Stach, E. A.; Berggren, K. K., Resolution Limits of Electron-Beam Lithography Toward the Atomic Scale. *Nano Lett.* **2013,** *13* (4), 1555-1558.

21. Cord, B.; Yang, J.; Duan, H.; Joy, D. C.; Klingfus, J.; Berggren, K. K., Limiting Factors in Sub-10 nm Scanning-Electron-Beam Lithography. *J. Vac. Sci. Technol., B: Microelectron. Nanometer Struct.--Process., Meas., Phenom.* **2009,** *27* (6), 2616-2621.

22. Rishton, S.; Kern, D., Point Exposure Distribution Measurements for Proximity Correction in Electron Beam Lithography on a Sub-100 nm Scale. *J. Vac. Sci. Technol., B: Microelectron. Process. Phenom.* **1987,** *5* (1), 135-141.

23. Kyser, D.; Viswanathan, N., Monte Carlo Simulation of Spatially Distributed Beams in Electron-Beam Lithography. *J. Vac. Sci. Technol.* **1975,** *12* (6), 1305-1308.

24. Clerico, V.; Amado, M.; Diez, E., Electron Beam Lithography and Its Use on 2D Materials. In *Nanofabrication Nanolithography Techniques and Their Applications*, Teresa, J. M. D., Ed. IOP Publishing: 2020; Vol. 3, pp 3-49.

25. Sun, Q.; Wang, Y. A.; Li, L. S.; Wang, D.; Zhu, T.; Xu, J.; Yang, C.; Li, Y., Bright, Multicoloured Light-Emitting Diodes Based on Quantum Dots. *Nat. Photonics* **2007,** *1* (12), 717-722.

26. Dai, X.; Zhang, Z.; Jin, Y.; Niu, Y.; Cao, H.; Liang, X.; Chen, L.; Wang, J.; Peng, X., Solution-Processed, High-Performance Light-Emitting Diodes Based on Quantum Dots. *Nature* **2014,** *515* (7525), 96-99.

27. Xin, S.; You, Y.; Wang, S.; Gao, H.-C.; Yin, Y.-X.; Guo, Y.-G., Solid-State Lithium Metal Batteries Promoted by Nanotechnology: Progress and Prospects. *ACS Energy Lett.* **2017,** *2* (6), 1385-1394.

28. Hu, C.-C.; Chang, K.-H.; Lin, M.-C.; Wu, Y.-T., Design and Tailoring of the Nanotubular Arrayed Architecture of Hydrous RuO_2 for Next Generation Supercapacitors. *Nano Lett.* **2006,** *6* (12), 2690-2695.

29. Munoz, R.; Gómez-Aleixandre, C., Review of CVD Synthesis of Graphene. *Chem. Vap. Depos.* **2013,** *19* (10-11-12), 297-322.

30. Terranova, M. L.; Sessa, V.; Rossi, M., The World of Carbon Nanotubes: An Overview of CVD Growth Methodologies. *Chem. Vap. Depos.* **2006,** *12* (6), 315-325.

31. Shi, J.; Zhou, Y.; Lu, Y.; Yi, K. In *Aligned Synthesis of Carbon Nanotubes by Laser-Assisted Chemical Vapor Deposition*, ICALEO, 2006; p M1106.

32. Sagiv, J., Organized Monolayers by Adsorption. 1. Formation and Structure of Oleophobic Mixed Monolayers on Solid Surfaces. *J. Am. Chem. Soc.* **1980,** *102* (1), 92-98.

33. Sautter, K. E.; Vallejo, K. D.; Simmonds, P. J., Strain-Driven Quantum Dot Self-Assembly by Molecular Beam Epitaxy. *J. Appl. Phys.* **2020,** *128* (3), 031101.

34. Dubrovskii, V. G., Theory of MBE Growth of Nanowires on Reflecting Substrates. *Nanomaterials* **2022,** *12* (2), 253.

35. Melngailis, J., Focused Ion Beam Technology and Applications. *J. Vac. Sci. Technol., B: Microelectron. Process. Phenom.* **1987,** *5* (2), 469-495.

36. Utke, I.; Hoffmann, P.; Melngailis, J., Gas-Assisted Focused Electron Beam and Ion Beam Processing and Fabrication. *J. Vac. Sci. Technol., B: Microelectron. Nanometer Struct.--Process., Meas., Phenom.* **2008,** *26* (4), 1197-1276.

37. Huth, M.; Porrati, F.; Schwalb, C.; Winhold, M.; Sachser, R.; Dukic, M.; Adams, J.; Fantner, G., Focused Electron Beam Induced Deposition: A Perspective. *Beilstein J. Nanotechnol.* **2012,** *3* (1), 597-619.

38. Van Dorp, W.; Hagen, C. W., A Critical Literature Review of Focused Electron Beam Induced Deposition. *J. Appl. Phys.* **2008,** *104* (8), 10.

39. Porrati, F.; Barth, S.; Sachser, R.; Dobrovolskiy, O. V.; Seybert, A.; Frangakis, A. S.; Huth, M., Crystalline Niobium Carbide Superconducting Nanowires Prepared by Focused Ion Beam Direct Writing. *ACS Nano* **2019,** *13* (6), 6287-6296.

40. De Teresa, J.; Córdoba, R.; Fernández-Pacheco, A.; Montero, O.; Strichovanec, P.; Ibarra, M., Origin of the Difference in the Resistivity of As-Grown Focused-Ion-and Focused-Electron-Beam-Induced Pt Nanodeposits. *J. Nanomater.* **2009,** *2009* (Article ID 936863).

41. Van Dorp, W. F.; Van Someren, B.; Hagen, C. W.; Kruit, P.; Crozier, P. A., Approaching the Resolution Limit of Nanometer-Scale Electron Beam-Induced Deposition. *Nano Lett.* **2005,** *5* (7), 1303-1307.

42. Fowlkes, J. D.; Winkler, R.; Lewis, B. B.; Stanford, M. G.; Plank, H.; Rack, P. D., Simulation-Guided 3D Nanomanufacturing via Focused Electron Beam Induced Deposition. *ACS Nano* **2016,** *10* (6), 6163-6172.

43. Belianinov, A.; Burch, M. J.; Ievlev, A.; Kim, S.; Stanford, M. G.; Mahady, K.; Lewis, B. B.; Fowlkes, J. D.; Rack, P. D.; Ovchinnikova, O. S., Direct Write of 3D Nanoscale Mesh Objects with Platinum Precursor via Focused Helium Ion Beam Induced Deposition. *Micromachines* **2020,** *11* (5), 527.

44. Utke, I.; Michler, J.; Winkler, R.; Plank, H., Mechanical Properties of 3D Nanostructures Obtained by Focused Electron/Ion Beam-Induced Deposition: A Review. *Micromachines* **2020,** *11* (4), 397.

45. Jones, A. C.; O'Brien, P., *CVD of Compound Semiconductors: Precursor Synthesis, Developmeny and Applications*. John Wiley & Sons: 2008.

46. Utke, I.; Swiderek, P.; Höflich, K.; Madajska, K.; Jurczyk, J.; Martinović, P.; Szymańska, I., Coordination and Organometallic Precursors of Group 10 and 11: Focused Electron Beam Induced Deposition of Metals and Insight Gained from Chemical Vapour Deposition, Atomic Layer Deposition, and Fundamental Surface and Gas Phase Studies. *Coord. Chem. Rev.* **2022**, 213851.

47. Botman, A.; Hesselberth, M.; Mulders, J., Investigation of Morphological Changes in Platinum-Containing Nanostructures Created by Electron-Beam-Induced Deposition. *J. Vac. Sci. Technol., B: Microelectron. Nanometer Struct.--Process., Meas., Phenom.* **2008,** *26* (6), 2464-2467.

48. Carden, W. G.; Lu, H.; Spencer, J. A.; Fairbrother, D. H.; McElwee-White, L., Mechanism-Based Design of Precursors for Focused Electron Beam-Induced Deposition. *MRS Commun.* **2018,** *8* (2), 343-357.

49. Barth, S.; Huth, M.; Jungwirth, F., Precursors for Direct-Write Nanofabrication with Electrons. *J. Mater. Chem. C* **2020,** *8* (45), 15884-15919.

50. De Teresa, J. M.; Orús, P.; Córdoba, R.; Philipp, P., Comparison Between Focused Electron/Ion Beam-Induced Deposition at Room Temperature and Under Cryogenic Conditions. *Micromachines* **2019,** *10* (12), 799.

51. Thorman, R. M.; TP, R. K.; Fairbrother, D. H.; Ingólfsson, O., The Role of Low-Energy Electrons in Focused Electron Beam Induced Deposition: Four Case Studies of Representative Precursors. *Beilstein J. Nanotechnol.* **2015,** *6* (1), 1904-1926.

52. Böhler, E.; Warneke, J.; Swiderek, P., Control of Chemical Reactions and Synthesis by Low-Energy Electrons. *Chem. Soc. Rev.* **2013,** *42* (24), 9219-9231.

53. Unlu, I.; Spencer, J. A.; Johnson, K. R.; Thorman, R. M.; Ingólfsson, O.; McElwee-White, L.; Fairbrother, D. H., Electron Induced Surface Reactions of (η^5-C_5H_5)$Fe(CO)_2Mn(CO)_5$, a Potential Heterobimetallic Precursor for Focused Electron Beam Induced Deposition (FEBID). *Phys. Chem. Chem. Phys.* **2018,** *20* (11), 7862-7874.

54. Rosenberg, S. G.; Barclay, M.; Fairbrother, D. H., Electron Induced Reactions of Surface Adsorbed Tungsten Hexacarbonyl ($W(CO)_6$). *Phys. Chem. Chem. Phys.* **2013,** *15* (11), 4002-4015.

55. Rosenberg, S. G.; Barclay, M.; Fairbrother, D. H., Electron Beam Induced Reactions of Adsorbed Cobalt Tricarbonyl Nitrosyl ($Co(CO)_3NO$) Molecules. *J. Phys. Chem. C* **2013,** *117* (31), 16053-16064.

56. Dubner, A.; Wagner, A.; Melngailis, J.; Thompson, C., The Role of the Ion-Solid Interaction in Ion-Beam-Induced Deposition of Gold. *J. Appl. Phys.* **1991,** *70* (2), 665-673.

57. Chen, P.; Salemink, H. W.; Alkemade, P. F., Roles of Secondary Electrons and Sputtered Atoms in Ion-Beam-Induced Deposition. *J. Vac. Sci. Technol., B: Microelectron. Nanometer Struct.--Process., Meas., Phenom.* **2009,** *27* (6), 2718-2721.

58. Zhou, W.; Apkarian, R.; Wang, Z. L.; Joy, D., Fundamentals of Scanning Electron Microscopy (SEM). In *Scanning microscopy for nanotechnology*, Springer: 2006; pp 1-40.

59. Brundle, C.; Watts, J.; Wolstenholme, J., X-Ray Photoelectron and Auger Electron Spectroscopy. In *Ewing's Analytical Instrumentation Handbook, Fourth Edition*, CRC Press: 2019; pp 381-408.

60. Cumpson, P. J.; Seah, M. P., Elastic Scattering Corrections in AES and XPS. II. Estimating Attenuation Lengths and Conditions Required for Their Valid Use in Overlayer/Substrate Experiments. *Surf. Interface Anal.* **1997,** *25* (6), 430-446.

61. Davis, L. E., *Handbook of Auger Electron Spectroscopy*. Physical Electronics Division: 1978.

62. Chastain, J.; King Jr, R. C., Handbook of X-Ray Photoelectron Spectroscopy. *Perkin-Elmer Corporation* **1992,** *40*, 221.

63. Johnstone, R. A.; Johnstone, R. A. W.; Johnstone, R. A.; Rose, M. E., *Mass Spectrometry for Chemists and Biochemists*. Cambridge University Press: 1996.

64. Dawson, P. H., *Quadrupole Mass Spectrometry and Its Applications*. Elsevier: 2013.

65. Binnig, G.; Quate, C. F.; Gerber, C., Atomic Force Microscope. *Phys. Rev. Lett.* **1986,** *56* (9), 930.

66. Leite, F. L.; Bueno, C. C.; Da Róz, A. L.; Ziemath, E. C.; Oliveira, O. N., Theoretical Models for Surface Forces and Adhesion and Their Measurement Using Atomic Force Microscopy. *Int. J. Mol. Sci.* **2012,** *13* (10), 12773-12856.

67. Mironov, V. L., Fundamentals of Scanning Probe Microscopy. *Nizhniy Novgorod* **2004**, 5.

68. Bilgilisoy, E.; Thorman, R. M.; Yu, J.-C.; Dunn, T. B.; Marbach, H.; McElwee-White, L.; Fairbrother, D. H., Surface Reactions of Low-Energy Argon Ions with Organometallic Precursors. *J. Phys. Chem. C.* **2020,** *124* (45), 24795-24808.

69. Wnuk, J. D.; Gorham, J. M.; Rosenberg, S. G.; van Dorp, W. F.; Madey, T. E.; Hagen, C. W.; Fairbrother, D. H., Electron Induced Surface Reactions of the Organometallic Precursor Trimethyl(methylcyclopentadienyl)platinum (IV). *J. Phys. Chem. C.* **2009,** *113* (6), 2487-2496.

70. Friedli, V.; Utke, I., Optimized Molecule Supply from Nozzle-Based Gas Injection Systems for Focused Electron-and Ion-Beam Induced Deposition and Etching: Simulation and Experiment. *J. Phys. D: Appl. Phys.* **2009,** *42* (12), 125305.

71. Lukasczyk, T. Generation of Pure Iron Nanostructures via Electron-Beam Induced Deposition in UHV. Friedrich-Alexander-Universitaet Erlangen-Nuernberg (Germany), 2010.

72. Banaszak Holl, M. M.; Seidler, P. F.; Kowalczyk, S. P.; McFeely, F. R., Surface Reactivity of Alkylgold(I) Complexes: Substrate-Selective Chemical Vapor Deposition of Gold from $RAuP(CH_3)_3$ ($R=CH_2CH_3$, CH_3) at Remarkably Low Temperatures. *Inorg. Chem.* **1994,** *33* (3), 510-517.

73. Calderazzo, F.; l'Eplattenier, F., Pentacarbonyls of Ruthenium and Osmium. I. Infrared Spectra and Reactivity. *Inorg. Chem.* **1967,** *6* (6), 1220-1224.

74. Johnson, B.; Johnston, R.; Lewis, J., Chemistry of Polynuclear Compounds. Part XV. Halogenocarbonylruthenium Compounds. *J. Chem. Soc. A* **1969**, 792-797.

75. Saha, S.; Captain, B., Synthesis and Structural Characterization of Ruthenium Carbonyl Cluster Complexes Containing Platinum with a Bulky N-Heterocyclic Carbene Ligand. *Inorg. Chem.* **2014,** *53* (2), 1210-1216.

76. Schmidbaur, H.; Shiotani, A., Organogold-Chemie, VI Darstellung komplexer Organogold-Verbindungen durch Liganden-Substitutionsreaktionen. *Chem. Ber.* **1971,** *104* (9), 2821-2830.

77. Vollnhals, F. R. Exploring Electron Beam Induced Surface Activation for the Fabrication of well-defined Nanostructures: On the Role of Catalytic Processes, Substrates and Precursors. Friedrich-Alexander-Universitaet Erlangen-Nuernberg (Germany), 2015.

78. Mehendale, S.; Mulders, J.; Trompenaars, P., A New Sequential EBID Process for the Creation of Pure Pt Structures From $MeCpPtMe_3$. *Nanotechnology* **2013,** *24* (14), 145303.

79. Shimojo, M.; Mitsuishi, K.; Tameike, A.; Furuya, K., Electron Induced Nanodeposition of Tungsten Using Field Emission Scanning and Transmission Electron Microscopes. *J. Vac. Sci. Technol., B: Microelectron. Nanometer Struct.--Process., Meas., Phenom.* **2004,** *22* (2), 742-746.

80. Lukasczyk, T.; Schirmer, M.; Steinrück, H. P.; Marbach, H., Electron-Beam-Induced Deposition in Ultrahigh Vacuum: Lithographic Fabrication of Clean Iron Nanostructures. *Small* **2008,** *4* (6), 841-846.

81. Lau, Y.; Chee, P.; Thong, J.; Ng, V., Properties and Applications of Cobalt-Based Material Produced by Electron-Beam-Induced Deposition. *J. Vac. Sci. Technol., A* **2002,** *20* (4), 1295-1302.

82. Vollnhals, F.; Drost, M.; Tu, F.; Carrasco, E.; Späth, A.; Fink, R. H.; Steinrück, H.-P.; Marbach, H., Electron-Beam Induced Deposition and Autocatalytic Decomposition of $Co(CO)_3NO$. *Beilstein J. Nanotechnol.* **2014,** *5* (1), 1175-1185.

83. Edinger, K.; Becht, H.; Bihr, J.; Boegli, V.; Budach, M.; Hofmann, T.; Koops, H. W.; Kuschnerus, P.; Oster, J.; Spies, P., Electron-Beam-Based Photomask Repair. *J. Vac. Sci. Technol., B: Microelectron. Nanometer Struct.--Process., Meas., Phenom.* **2004,** *22* (6), 2902-2906.

84. Liang, T.; Frendberg, E.; Lieberman, B.; Stivers, A., Advanced Photolithographic Mask Repair Using Electron Beams. *J. Vac. Sci. Technol., B: Microelectron. Nanometer Struct.--Process., Meas., Phenom.* **2005,** *23* (6), 3101-3105.

85. Di Prima, G.; Sachser, R.; Trompenaars, P.; Mulders, H.; Huth, M., Direct-Write Single Electron Transistors by Focused Electron Beam Induced Deposition. *Nano Futures* **2019,** *3* (2), 025001.

86. Fernández-Pacheco, A.; Serrano-Ramón, L.; Tyliszczak, T.; Chou, K.; Córdoba, R.; Szkudlarek, A.; O'Brien, L.; Kapusta, C.; Ibarra, M.; De Teresa, J., Correlation Between the Magnetic Imaging of Cobalt Nanoconstrictions and Their Magnetoresistance Response. *Nanotechnology* **2012,** *23* (10), 105703.

87. Winkler, R.; Schmidt, F.-P.; Haselmann, U.; Fowlkes, J. D.; Lewis, B. B.; Kothleitner, G.; Rack, P. D.; Plank, H., Direct-Write 3D Nanoprinting of Plasmonic Structures. *ACS Appl. Mater. Interfaces* **2017,** *9* (9), 8233-8240.

88. Walz, M.-M.; Vollnhals, F.; Rietzler, F.; Schirmer, M.; Steinrück, H.-P.; Marbach, H., Investigation of Proximity Effects in Electron Microscopy and Lithography. *Appl. Phys. Lett.* **2012,** *100* (5), 053118.

89. Plank, H.; Smith, D. A.; Haber, T.; Rack, P. D.; Hofer, F., Fundamental Proximity Effects in Focused Electron Beam Induced Deposition. *ACS Nano* **2012,** *6* (1), 286-294.

90. Shimojo, M.; Takeguchi, M.; Tanaka, M.; Mitsuishi, K.; Furuya, K., Electron Beam-Induced Deposition Using Iron Carbonyl and the Effects of Heat Treatment on Nanostructure. *Appl. Phys. A* **2004,** *79* (8), 1869-1872.

91. Mitsuishi, K.; Liu, Z.; Shimojo, M.; Han, M.; Furuya, K., Dynamic Profile Calculation of Deposition Resolution by High-Energy Electrons in Electron-Beam-Induced Deposition. *Ultramicroscopy* **2005,** *103* (1), 17-22.

92. De Teresa, J.; Fernández-Pacheco, A.; Córdoba, R.; Serrano-Ramón, L.; Sangiao, S.; Ibarra, M. R., Review of Magnetic Nanostructures Grown by Focused Electron Beam Induced Deposition (FEBID). *J. Phys. D: Appl. Phys.* **2016,** *49* (24), 243003.

93. Koops, H.; Weiel, R.; Kern, D.; Baum, T., High-Resolution Electron-Beam Induced Deposition. *J. Vac. Sci. Technol., B: Microelectron. Process. Phenom.* **1988,** *6* (1), 477-481.

94. Höflich, K.; Jurczyk, J. M.; Madajska, K.; Götz, M.; Berger, L.; Guerra-Nuñez, C.; Haverkamp, C.; Szymanska, I.; Utke, I., Towards the Third Dimension in Direct Electron Beam Writing of Silver. *Beilstein J. Nanotechnol.* **2018,** *9* (1), 842-849.

95. Botman, A.; Mulders, J.; Hagen, C., Creating Pure Nanostructures From Electron-Beam-Induced Deposition Using Purification Techniques: A Technology Perspective. *Nanotechnology* **2009,** *20* (37), 372001.

96. Ahlenhoff, K.; Preischl, C.; Swiderek, P.; Marbach, H., Electron Beam-Induced Surface Activation of Metal–Organic Framework HKUST-1: Unraveling the Underlying Chemistry. *J. Phys. Chem. C.* **2018,** *122* (46), 26658-26670.

97. Preischl, C.; Rohdenburg, M.; Bilgilisoy, E.; Cartaya, R.; Swiderek, P.; Marbach, H., Ultrathin Carbon Nanomembranes from 5, 10, 15, 20-Tetraphenylporphyrin: Electron Beam Induced Fabrication and Functionalization via Focused Electron Beam Induced Processing. *J. Phys. Chem. C* **2020,** *124* (51), 28335-28344.

98. Preischl, C.; Le, L. H.; Bilgilisoy, E.; Vollnhals, F.; Gölzhäuser, A.; Marbach, H., Controlled Electron-Induced Fabrication of Metallic Nanostructures on 1 nm Thick Membranes. *Small* **2020,** *16* (45), 2003947.

99. van Dorp, W. F.; Lazić, I.; Beyer, A.; Gölzhäuser, A.; Wagner, J. B.; Hansen, T. W.; Hagen, C. W., Ultrahigh Resolution Focused Electron Beam Induced Processing: The Effect of Substrate Thickness. *Nanotechnology* **2011,** *22* (11), 115303.

100. Drost, M.; Tu, F.; Berger, L.; Preischl, C.; Zhou, W.; Gliemann, H.; Wöll, C.; Marbach, H., Surface-Anchored Metal–Organic Frameworks as Versatile Resists for Gas-Assisted E-Beam Lithography: Fabrication of Sub-10 Nanometer Structures. *ACS Nano* **2018,** *12* (4), 3825-3835.

101. Van Dorp, W., Sub-10 nm Writing: Focused Electron Beam-Induced Deposition in Perspective. *Appl. Phys. A* **2014,** *117* (4), 1615-1622.

102. Preischl, C.; Le, L. H.; Bilgilisoy, E.; Gölzhäuser, A.; Marbach, H., Exploring the Fabrication and Transfer Mechanism of Metallic Nanostructures on Carbon Nanomembranes via Focused Electron Beam Induced Processing. *Beilstein J. Nanotechnol.* **2021,** *12* (1), 319-329.

103. Noh, J.-H.; Stanford, M. G.; Lewis, B. B.; Fowlkes, J. D.; Plank, H.; Rack, P., Nanoscale Electron Beam-Induced Deposition and Purification of Ruthenium for Extreme Ultraviolet Lithography Mask Repair. *Appl. Phys. A* **2014,** *117* (4), 1705-1713.

104. Rohdenburg, M.; Winkler, R.; Kuhness, D.; Plank, H.; Swiderek, P., Water-Assisted Process for Purification of Ruthenium Nanomaterial Fabricated by Electron Beam Induced Deposition. *ACS Appl. Nano Mater.* **2020,** *3* (8), 8352-8364.

105. Jurczyk, J.; Brewer, C. R.; Hawkins, O. M.; Polyakov, M. N.; Kapusta, C.; McElwee-White, L.; Utke, I., Focused Electron Beam-Induced Deposition and Post-Growth Purification Using the Heteroleptic Ru Complex $(\eta^3C_3H_5)Ru(CO)_3Br$. *ACS Appl. Mater. Interfaces* **2019,** *11* (31), 28164-28171.

106. Shawrav, M. M.; Taus, P.; Wanzenboeck, H. D.; Schinnerl, M.; Stöger-Pollach, M.; Schwarz, S.; Steiger-Thirsfeld, A.; Bertagnolli, E., Highly Conductive and Pure Gold Nanostructures Grown by Electron Beam Induced Deposition. *Sci. Rep.* **2016,** *6* (1), 1-10.

107. Hari, S.; Trompenaars, P.; Mulders, J.; Kruit, P.; Hagen, C., Combined Focused Electron Beam-Induced Deposition and Etching for the Patterning of Dense Lines Without Interconnecting Material. *Micromachines* **2020,** *12* (1), 8.

108. Shawrav, M.; Gökdeniz, Z.; Wanzenboeck, H.; Taus, P.; Mika, J.; Waid, S.; Bertagnolli, E., Chlorine Based Focused Electron Beam Induced Etching: A Novel Way to Pattern Germanium. *Mater. Sci. Semicond. Process.* **2016,** *42*, 170-173.

109. Toth, M.; Lobo, C. J.; Knowles, W. R.; Phillips, M. R.; Postek, M. T.; Vladár, A. E., Nanostructure Fabrication by Ultra-High-Resolution Environmental Scanning Electron Microscopy. *Nano Lett.* **2007,** *7* (2), 525-530.

110. Coburn, J. W.; Winters, H. F., Ion-and Electron-Assisted Gas-Surface Chemistry—An Important Effect in Plasma Etching. *J. Appl. Phys.* **1979,** *50* (5), 3189-3196.

111. Heil, T.; Waldow, M.; Capelli, R.; Schneider, H.; Ahmels, L.; Tu, F.; Schöneberg, J.; Marbach, H., Pushing the Limits of EUV Mask Repair: Addressing Sub-10 nm Defects with the Next Generation E-Beam-Based Mask Repair Tool. *J. Micro/Nanopatterning, Mater., Metrol.* **2021,** *20* (3), 031013.

112. Liang, T.; Stivers, A. R. In *Damage-Free Mask Repair Using Electron-Beam-Induced Chemical Reactions*, Emerging Lithographic Technologies VI, SPIE: 2002; pp 375-384.

113. Randolph, S.; Fowlkes, J.; Rack, P., Focused, Nanoscale Electron-Beam-Induced Deposition and Etching. *Crit. Rev. Solid State Mater. Sci* **2006,** *31* (3), 55-89.

114. Martin, A. A.; McCredie, G.; Toth, M., Electron Beam Induced Etching of Carbon. *Appl. Phys. Lett.* **2015,** *107* (4), 041603.

115. Randolph, S.; Toth, M.; Cullen, J.; Chandler, C.; Lobo, C., Kinetics of Gas Mediated Electron Beam Induced Etching. *Appl. Phys. Lett.* **2011,** *99* (21), 213103.

116. Toth, M.; Lobo, C. J.; Hartigan, G.; Ralph Knowles, W., Electron Flux Controlled Switching Between Electron Beam Induced Etching and Deposition. *J. Appl. Phys.* **2007,** *101* (5), 054309.

117. Randolph, S.; Fowlkes, J.; Rack, P., Focused Electron-Beam-Induced Etching of Silicon Dioxide. *J. Appl. Phys.* **2005,** *98* (3), 034902.

118. Matsui, S.; Ichihashi, T.; Mito, M., Electron Beam Induced Selective Etching and Deposition Technology. *J. Vac. Sci. Technol., B: Microelectron. Process. Phenom.* **1989,** *7* (5), 1182-1190.

119. Taniguchi, J. T. J.; Miyamoto, I. M. I.; Ohno, N. O. N.; Kantani, K. i. K. K. i.; Komuro, M. K. M.; Hiroshima, H. H. H., Electron Beam Assisted Chemical Etching of Single-Crystal Diamond Substrates with Hydrogen Gas. *Jpn. J. Appl. Phys.* **1997,** *36* (12S), 7691.

120. Hoffmann, P.; Utke, I.; Perentes, A.; Bret, T.; Santschi, C.; Apostolopoulos, V. In *Comparison of Fabrication Methods of Sub-100nm Nano-Optical Structures and Devices*, Nanophotonic Materials and Systems II, International Society for Optics and Photonics: 2005; p 592506.

121. Lobo, C. J.; Martin, A.; Phillips, M. R.; Toth, M., Electron Beam Induced Chemical Dry Etching and Imaging in Gaseous NH_3 Environments. *Nanotechnology* **2012,** *23* (37), 375302.

122. Toth, M.; Lobo, C.; Friedli, V.; Szkudlarek, A.; Utke, I., Continuum Models of Focused Electron Beam Induced Processing. *Beilstein J. Nanotechnol.* **2015,** *6* (1), 1518-1540.

123. Bernau, L.; Gabureac, M.; Erni, R.; Utke, I., Tunable Nanosynthesis of Composite Materials by Electron-Impact Reaction. *Angew. Chem.* **2010,** *122* (47), 9064-9068.

124. Lassiter, M. G.; Rack, P. D., Nanoscale Electron Beam Induced Etching: A Continuum Model that Correlates the Etch Profile to the Experimental Parameters. *Nanotechnology* **2008,** *19* (45), 455306.

125. Bilgilisoy, E.; Yu, J.-C.; Preischl, C.; McElwee-White, L.; Steinrück, H.-P.; Marbach, H., Nanoscale Ruthenium-Containing Deposits from $Ru(CO)_4I_2$ via Simultaneous Focused Electron Beam-Induced Deposition and Etching in Ultrahigh Vacuum: Mask Repair in Extreme Ultraviolet Lithography and Beyond. *ACS Appl. Nano Mater.* **2022,** *5* (3), 3855-3865.

126. Martin, A. A.; Phillips, M. R.; Toth, M., Dynamic Surface Site Activation: A Rate Limiting Process in Electron Beam Induced Etching. *ACS Appl. Mater. Interfaces* **2013,** *5* (16), 8002-8007.

127. Walz, M. M.; Schirmer, M.; Vollnhals, F.; Lukasczyk, T.; Steinrück, H. P.; Marbach, H., Electrons as “Invisible Ink”: Fabrication of Nanostructures by Local Electron Beam Induced Activation of SiOx. *Angew. Chem. Int. Ed.* **2010,** *49* (27), 4669-4673.

128. Schirmer, M.; Walz, M.; Vollnhals, F.; Lukasczyk, T.; Sandmann, A.; Chen, C.; Steinrück, H.; Marbach, H., Electron-Beam-Induced Deposition and Post-Treatment Processes to Locally Generate Clean Titanium Oxide Nanostructures on Si (100). *Nanotechnology* **2011,** *22* (8), 085301.

129. Drouin, D.; Couture, A. R.; Joly, D.; Tastet, X.; Aimez, V.; Gauvin, R., CASINO V2. 42—A Fast and Easy-To-Use Modeling Tool for Scanning Electron Microscopy and Microanalysis Users. *Scanning: The Journal of Scanning Microscopies* **2007,** *29* (3), 92-101.

130. Walz, M.-M. Fabrication of Clean Iron Nanostructures on Silicon Oxide via Focused Electron Beam Induced Processing in UHV. Doctoral thesis, Lehrstuhl für Physikalische Chemie II, Friedrich-Alexander, 2012.

131. Jesse, S.; Borisevich, A. Y.; Fowlkes, J. D.; Lupini, A. R.; Rack, P. D.; Unocic, R. R.; Sumpter, B. G.; Kalinin, S. V.; Belianinov, A.; Ovchinnikova, O. S., Directing Matter: Toward Atomic-Scale 3D Nanofabrication. *ACS Nano* **2016,** *10* (6), 5600-5618.

132. Schmied, R.; Fowlkes, J. D.; Winkler, R.; Rack, P. D.; Plank, H., Fundamental Edge Broadening Effects During Focused Electron Beam Induced Nanosynthesis. *Beilstein J. Nanotechnol.* **2015,** *6* (1), 462-471.

133. Plank, H.; Winkler, R.; Schwalb, C. H.; Hütner, J.; Fowlkes, J. D.; Rack, P. D.; Utke, I.; Huth, M., Focused Electron Beam-Based 3D Nanoprinting for Scanning Probe Microscopy: A Review. *Micromachines* **2019,** *11* (1), 48.

134. Smith, D.; Fowlkes, J.; Rack, P., A Nanoscale Three-Dimensional Monte Carlo Simulation of Electron-Beam-Induced Deposition with Gas Dynamics. *Nanotechnology* **2007,** *18* (26), 265308.

135. Engmann, S.; Stano, M.; Matejčík, Š.; Ingólfsson, O., Gas Phase Low Energy Electron Induced Decomposition of the Focused Electron Beam Induced Deposition (FEBID) Precursor Trimethyl (Methylcyclopentadienyl) Platinum(IV)($MeCpPtMe_3$). *Phys. Chem. Chem. Phys.* **2012,** *14* (42), 14611-14618.

136. Engmann, S.; Stano, M.; Papp, P.; Brunger, M. J.; Matejčík, Š.; Ingólfsson, O., Absolute Cross Sections for Dissociative Electron Attachment and Dissociative Ionization of Cobalt tricarbonyl Nitrosyl in the Energy Range From 0 eV to 140 eV. *Chem. Phys.* **2013,** *138* (4), 044305.

137. May, O.; Kubala, D.; Allan, M., Dissociative Electron Attachment to $Pt(PF_3)_4$—A Precursor for Focused Electron Beam Induced Processing (FEBIP). *Phys. Chem. Chem. Phys.* **2012,** *14* (9), 2979-2982.

138. Thorman, R. M.; Brannaka, J. A.; McElwee-White, L.; Ingólfsson, O., Low Energy Electron-Induced Decomposition of $(\eta^3\text{-}C_3H_5)Ru(CO)_3Br$, A Potential Focused Electron Beam Induced Deposition Precursor with a Heteroleptic Ligand Set. *Phys. Chem. Chem. Phys.* **2017,** *19* (20), 13264-13271.

139. TP, R. K.; Unlu, I.; Barth, S.; Ingólfsson, O.; Fairbrother, D. H., Electron Induced Surface Reactions of $HFeCo_3(CO)_{12}$, a Bimetallic Precursor for Focused Electron Beam Induced Deposition (FEBID). *J. Phys. Chem. C.* **2018,** *122* (5), 2648-2660.

140. Botman, A.; De Winter, D.; Mulders, J., Electron-Beam-Induced Deposition of Platinum at Low Landing Energies. *J. Vac. Sci. Technol., B: Microelectron. Nanometer Struct.--Process., Meas., Phenom.* **2008,** *26* (6), 2460-2463.

141. Ingólfsson, O.; Weik, F.; Illenberger, E., The Reactivity of Slow Electrons with Molecules at Different Degrees of Aggregation: Gas Phase, Clusters and Condensed Phase. *Int. J. Mass Spectrom. Ion Processes* **1996,** *155* (1-2), 1-68.

142. Bald, I.; Langer, J.; Tegeder, P.; Ingólfsson, O., From Isolated Molecules Through Clusters and Condensates to the Building Blocks of Life. *Int. J. Mass Spectrom.* **2008,** *277* (1-3), 4-25.

143. Arumainayagam, C. R.; Lee, H.-L.; Nelson, R. B.; Haines, D. R.; Gunawardane, R. P., Low-Energy Electron-Induced Reactions in Condensed Matter. *Surf. Sci. Rep.* **2010,** *65* (1), 1-44.

144. Ingólfsson, O., *Low-Energy Electrons: Fundamentals and Applications*. CRC Press: 2019.

145. Thorman, R. M.; Jensen, P. A.; Yu, J.-C.; Matsuda, S. J.; McElwee-White, L.; Ingólfsson, O.; Fairbrother, D. H., Electron-Induced Reactions of $Ru(CO)_4I_2$: Gas Phase, Surface, and Electron Beam-Induced Deposition. *J. Phys. Chem. C.* **2020,** *124* (19), 10593-10604.

146. Wnorowski, K.; Stano, M.; Matias, C.; Denifl, S.; Barszczewska, W.; Matejčík, Š., Low-Energy Electron Interactions with Tungsten Hexacarbonyl–$W(CO)_6$. *Rapid Commun. Mass Spectrom.* **2012,** *26* (17), 2093-2098.

147. Balog, R.; Langer, J.; Gohlke, S.; Stano, M.; Abdoul-Carime, H.; Illenberger, E., Low Energy Electron Driven Reactions in Free and Bound Molecules: From Unimolecular Processes in the Gas Phase to Complex Reactions in a Condensed Environment. *Int. J. Mass Spectrom.* **2004,** *233* (1-3), 267-291.

148. Menzel, D., Electronically Induced Surface Chemistry: Localised Bond Breaking Versus Delocalisation. *Surf. Interface Anal.* **2006,** *38* (12-13), 1702-1711.

149. Swiderek, P.; Jäggle, C.; Bankmann, D.; Burean, E., Fate of Reactive Intermediates Formed in Acetaldehyde Under Exposure to Low-Energy Electrons. *J. Phys. Chem. C* . **2007,** *111* (1), 303-311.

150. Deshpande, P.; Vilayurganapathy, S.; Bhat, K.; Ghosh, A., Study of Ga^+ Implantation in Si Diodes: Effect on Optoelectronic Properties Using Micro-Spectroscopy. *Appl. Phys. A* **2019,** *125* (3), 1-6.

151. Tan, S.; Livengood, R.; Shima, D.; Notte, J.; McVey, S., Gas Field Ion Source and Liquid Metal Ion Source Charged Particle Material Interaction Study for Semiconductor Nanomachining Applications. *J. Vac. Sci. Technol. B:Nanotechnol. Microelectron.* **2010,** *28* (6), C6F15-C6F21.

152. Indrajith, S.; Rousseau, P.; Huber, B. A.; Nicolafrancesco, C.; Domaracka, A.; Grygoryeva, K.; Nag, P.; Sedmidubská, B.; Fedor, J.; Kocisek, J., Decomposition of Iron Pentacarbonyl Induced by Singly and Multiply Charged Ions and Implications for Focused Ion Beam-Induced Deposition. *J. Phys. Chem. C* **2019,** *123* (16), 10639-10645.

153. Thorman, R. M.; Matsuda, S. J.; McElwee-White, L.; Fairbrother, D. H., Identifying and Rationalizing the Differing Surface Reactions of Low-Energy Electrons and Ions with an Organometallic Precursor. *J. Phys. Chem. Lett.* **2020,** *11* (6), 2006-2013.

154. Córdoba, R.; Orús, P.; Strohauer, S.; Torres, T. E.; De Teresa, J. M., Ultra-Fast Direct Growth of Metallic Micro-and Nano-Structures by Focused Ion Beam Irradiation. *Sci. Rep.* **2019,** *9* (1), 1-10.

155. Morgan, D. J., Resolving Ruthenium: XPS Studies of Common Ruthenium Materials. *Surf. Interface Anal.* **2015,** *47* (11), 1072-1079.

156. Estrade-Szwarckopf, H., XPS Photoemission in Carbonaceous Materials: A "Defect" Peak Beside the Graphitic Asymmetric Peak. *Carbon* **2004,** *42* (8-9), 1713-1721.

157. Bianchi, C.; Ragaini, V.; Cattania, M., An XPS Study on Ruthenium Compounds and Catalysts. *Mater. Chem. Phys.* **1991,** *29* (1-4), 297-306.

158. Plummer, E.; Salaneck, W.; Miller, J., Photoelectron Spectra of Transition-Metal Carbonyl Complexes: Comparison with the Spectra of Adsorbed CO. *Phys. Rev. B* **1978,** *18* (4), 1673.

159. Chen, H.; Jolly, W. L., An XPS Study of the Relative pi-Acceptor Abilities of the Nitrosyl and Carbonyl Ligands. *Inorg. Chem.* **1979,** *18* (9), 2548-2551.

160. Sherwood, P. M., X-Ray Photoelectron Spectroscopic Studies of Some Iodine Compounds. *J. Chem. Soc., Faraday Trans. 2* **1976,** *72*, 1805-1820.

161. Zaera, F., A Thermal Desorption and X-Ray Photoelectron Spectroscopy Study of the Surface Chemistry of Iron Pentacarbonyl. *J. Vac. Sci. Technol., A* **1989,** *7* (3), 640-645.

162. Mansour, A.; Brizzolara, R. A., Characterization of the Surface of FeO Powder by XPS. *Surf. Sci. Spectra* **1996,** *4* (4), 345-350.

163. Fujii, T.; De Groot, F.; Sawatzky, G.; Voogt, F.; Hibma, T.; Okada, K., In Situ XPS Analysis of Various Iron Oxide Films Grown by NO_2-Assisted Molecular-Beam Epitaxy. *Phys. Rev. B* **1999,** *59* (4), 3195.

164. Van Staden, M.; Roux, J., The Superposition of Carbon and Ruthenium Auger Spectra. *Appl. Surf. Sci.* **1990,** *44*, 259-262.

165. Mulders, J.; Veerhoek, J.; Bosch, E.; Trompenaars, P., Fabrication of Pure Gold Nanostructures by Electron Beam Induced Deposition with Au(CO)Cl Precursor: Deposition Characteristics and Primary Beam Scattering Effects. *J. Phys. D: Appl. Phys.* **2012,** *45* (47), 475301.

166. Marashdeh, A.; Tiesma, T.; van Velzen, N. J.; Harder, S.; Havenith, R. W.; De Hosson, J. T.; van Dorp, W. F., The Rational Design of a Au(I) Precursor for Focused Electron Beam Induced Deposition. *Beilstein J. Nanotechnol.* **2017,** *8*, 2753-2765.

167. Van Dorp, W.; Wu, X.; Mulders, J.; Harder, S.; Rudolf, P.; De Hosson, J., Gold Complexes for Focused-Electron-Beam-Induced Deposition. *Langmuir* **2014,** *30*, 12097-12105.

7 Abbreviations

SEM	Scanning Electron Microscopy
STM	Scanning Tunnelling Microscopy
EBL	Electron Beam Lithography
CVD	Chemical Vapor Deposition
MBE	Molecular Beam Epitaxy
FEBID/FEBIP	Focused Electron Beam Induced Deposition/Processing
FIBID	Focused Ion Beam Induced Deposition
GIS	Gas Injection System
HV / UHV	High-/Ultrahigh Vacuum
XPS	X-ray Photoelectron Spectroscopy
QMS/MS	Quadrupole Mass Spectrometry / Mass Spectrometry
AES	Auger Electron Spectroscopy
AFM	Atomic Force Microscopy
ELENA-ITN	Low energy ELEctron driven chemistry for the advantage of emerging NAno- fabrication methods-Innovative Training Network
CD	Critical Dimension
NA	Numerical Aperture
PE	Primary Electrons
BSE	Back Scattered Electrons
SE	Secondary Electrons
FSE	Forward Scattered Electrons
EDX	Energy Dispersive X-ray Spectroscopy
IMFP	Inelastic Mean Free Path
DC	Direct Current
RF	Radiofrequency

ESEM	Environmental Scanning Electron Microscope
EBID	Electron Beam Induced Deposition
EBISA	Electron Beam Induced Surface Activation
AG	Autocatalytic Growth
EBIE	Electron Beam Induced Etching
LEEs	Low Energy Electrons
DEA	Dissociative Electron Attachment
DI	Dissociative Ionization
ND	Neutral Dissociative
DD	Dipolar Dissociation
SAM	Scanning Auger Microscopy

8 Acknowledgement

There are many people who supported me during my PhD journey, and I am glad to have the opportunity to thank everyone who contributed to this PhD thesis.

I am grateful to Prof. Hans-Peter Steinrück for giving me the opportunity to work at the chair of PC II, for his valuable input regarding this thesis and the studies that construct this thesis, and for being a true mentor for me. I would like to thank PD Dr. Hubertus Marbach for offering me this PhD opportunity, for supervising my thesis, for all his help regarding the experimental and theoretical aspects of this work, and for his endless support with the challenges I faced during my PhD.

I would like to thank former EBID team members; Dr. Florian Vollnhals and Dr. Christian Preischl, for the very nice working atmosphere, for the fruitful discussions, for all the help with the experiments, and for their great friendship. I would also like to thank Alexander Wolfram for his contribution in the framework of his master thesis and for his friendship. I would also like to thank shared lab members; Jan Brox and Rajan Adhikari, for keeping an eye on the EBID device when I was not in the lab and for their enjoyable chats between the experiments. Furthermore, I owe a special thanks to the secretariat office members; Andrea Meixner-Wolf and Susanna Kreß, for their patience and help especially in getting through all the paperwork during the PhD. Other special thanks must also go to Hans-Peter Bäumler, Bernd Kreß, Friedhold Wölfel, and the members of the mechanical workshop for their outstanding support and help with repairing and/or modifying the device.

I would like to thank Prof. Sjoerd Harder for being on my PhD committee. Prof. Sjoerd Harder and his former students, Dr. Thomas Gentner and Dr. Gerd Ballmann, also deserve special thanks for the synthesis of gold precursors and for letting me use their glove box whenever I needed it.

I would like to thank ELENA-ITN Project for funding, providing a perfect collaborative environment and for all the personal/scientific skill training opportunities. I would also like to thank our collaborators within the ELENA-ITN framework; particularly Prof. Howard Fairbrother at Johns Hopkins University for welcoming me during a four-month research stay in his lab and for teaching me everything I know about XPS. Prof. Howard Fairbrother and his former student Dr. Rachel Thorman deserve special thanks for giving support and feedback on my results and for editing all my writing. I would also like to thank Prof. Lisa McElwee-White and her student Dr.

Jo-Chi Yu at the University of Florida for the fruitful collaboration. Additionally, I would like to thank Prof. Oddur Ingólfsson at the University of Iceland, and his student Ali Kamali for their great collaboration. I would also like to thank Dr. Jaroslav Jiruše, Dr. Zsolt Radi, Dr. Miroslav Rudolf, Dr. Nagavalli Kiran, and Dominik Markó for their help during my two-months research stay at TESCAN-Brno. Finally, I would like to thank my fellow ESRs of ELENA-ITN project for their extraordinary friendship.

Finally, I would like to thank my friends and family for their endless love and support. Thank you to my parents; Zeliha and Sedat Bilgilisoy, for their encouragement and support despite the distances between us. I would also like to thank my sister and brother-in-law; Evren and Cem Ozbağ, for the fun phone conversations when I was overwhelmed. Finally, I would not have been able to accomplish this journey without the constant love, and support of my husband, Oğuzhan Alperen. I am very lucky to have him with me and always by my side!

9 Appendix

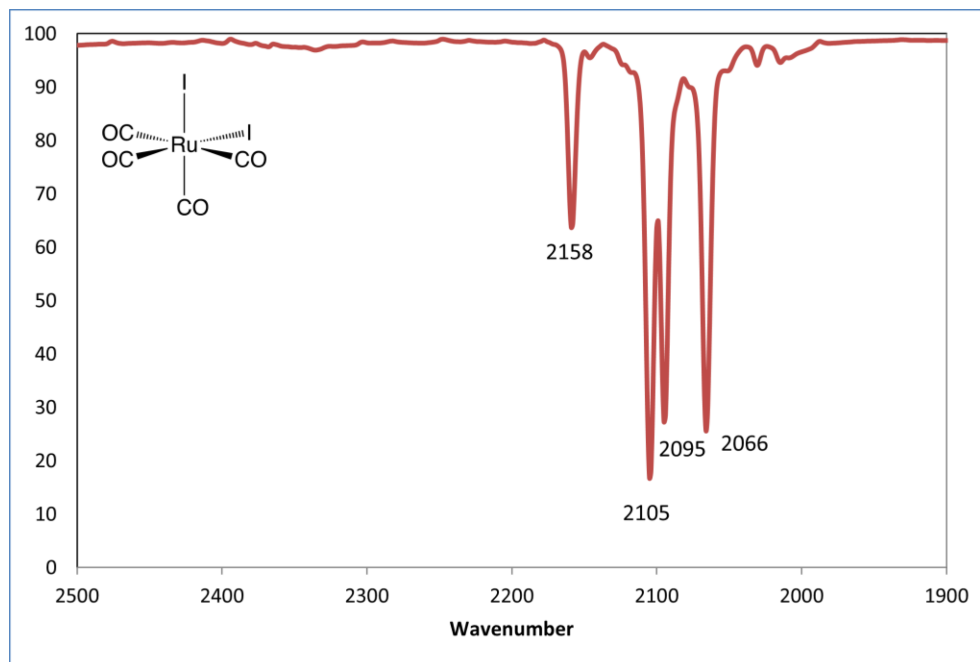

Appendix 1. *IR for $Ru(CO)_4I_2$; 2158 (m), 2105 (vs), 2095 (s), 2066 (s) cm^{-1}.*

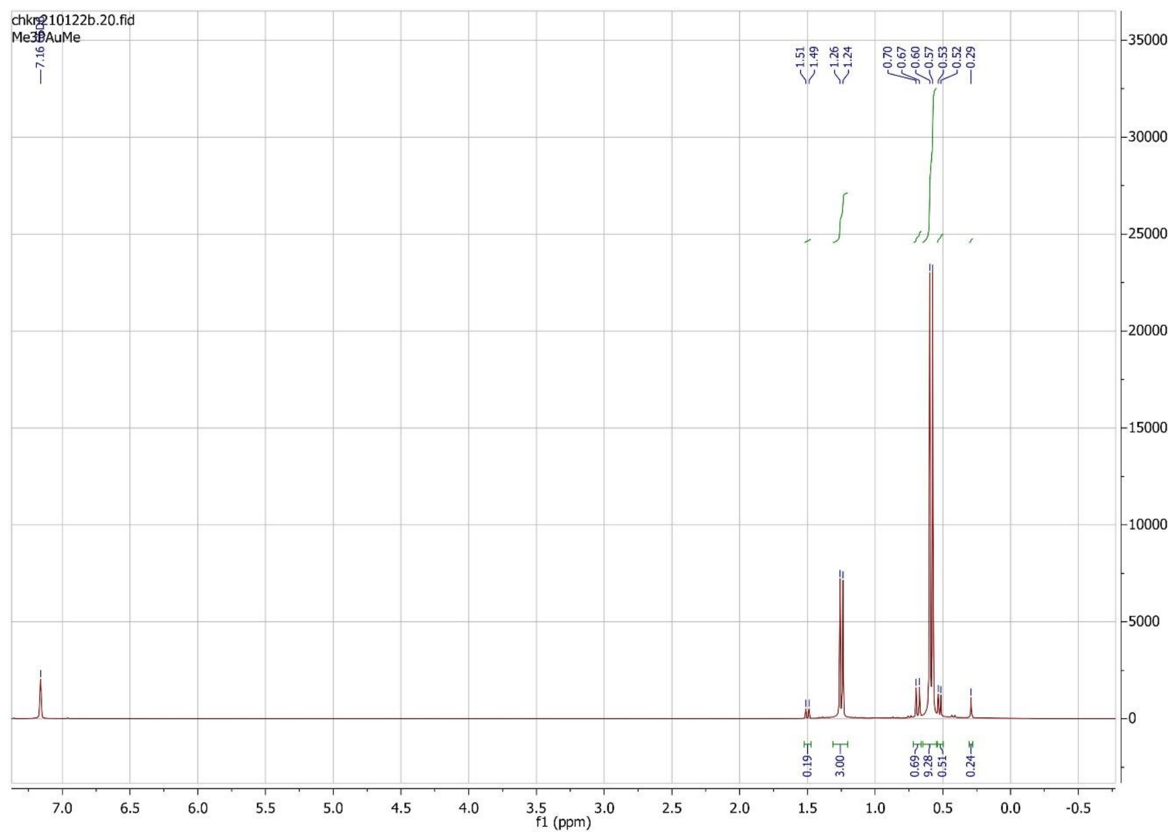

Appendix 2. *The first part of ¹H NMR spectra for* $(CH_3)AuP(CH_3)_3$.

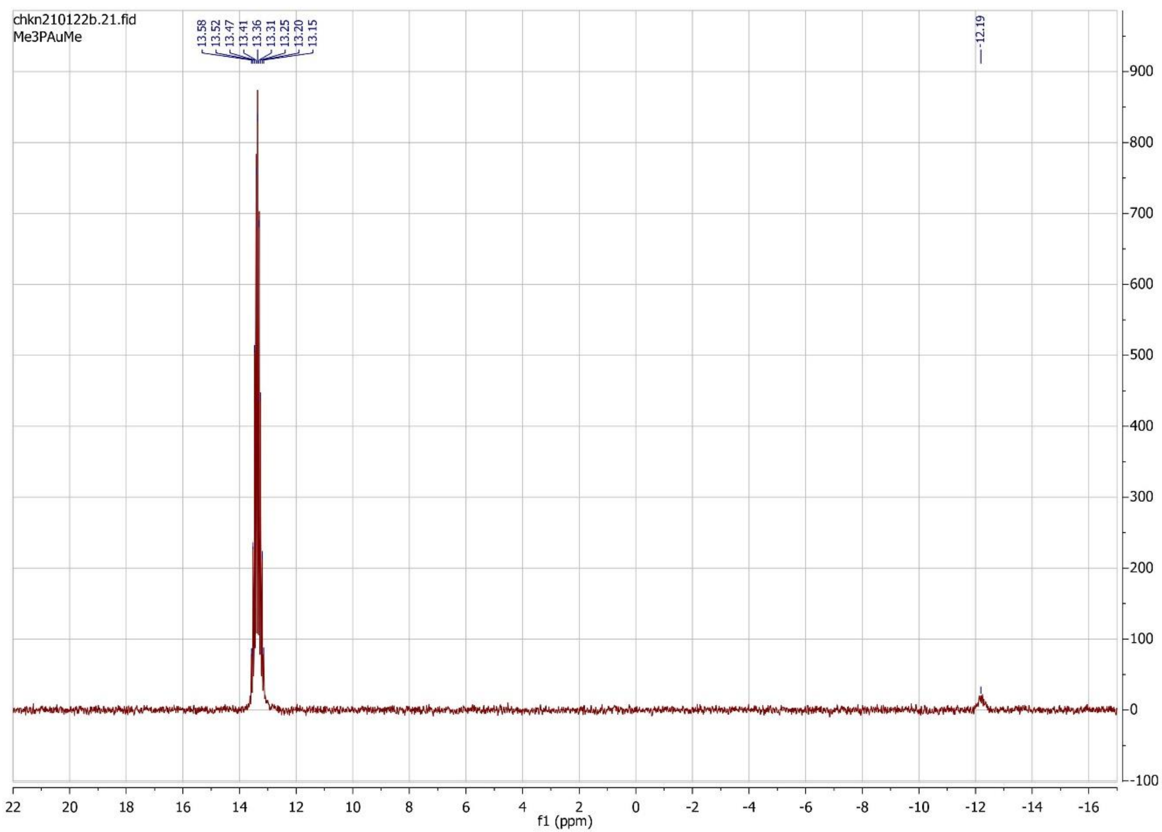

Appendix 3. *The second part of* ^{1}H *NMR spectra for* $(CH_3)AuP(CH_3)_3$.

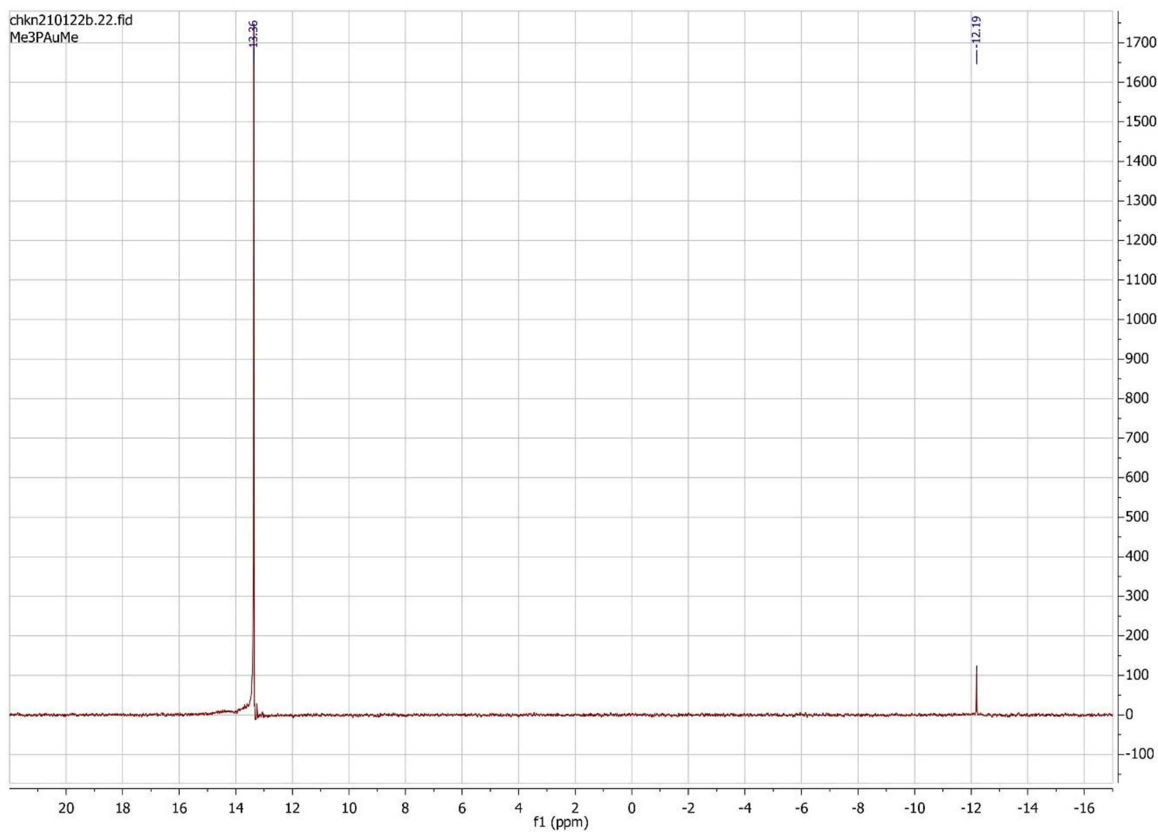

Appendix 4. *The third part of ^{1}H NMR spectra for* $(CH_3)AuP(CH_3)_3$.

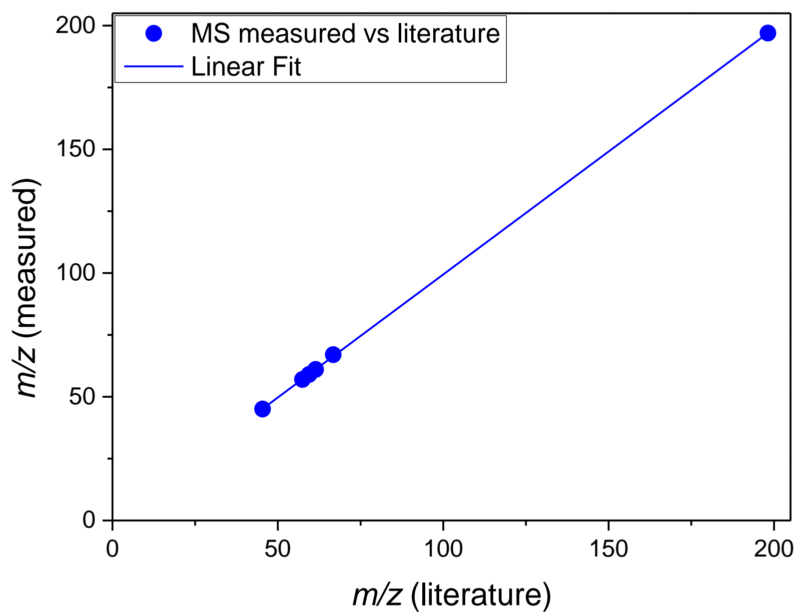

Appendix 5. *The mass shift in QMS as a result of calibration error.*

9.1 Publications [P1] – [P4]

[P1] **Surface Reactions of Low-Energy Argon Ions with Organometallic Precursors**

E. Bilgilisoy, R. M. Thorman, J. C. Yu, T. B. Dunn, H. Marbach, L. McElwee-White, D. H. Fairbrother

J. Phys. Chem. C, **2020,** *124*, 24795-24808

DOI: 10.1021/acs.jpcc.0c07269

Reprinted with permission from "The Journal of Physical Chemistry C". Copyright © 2020, American Chemical Society. Further permissions related to this article should be directed to the American Chemical Society.

[P2] **Low Energy Electron- and Ion-Induced Reactions of $Fe(CO)_5$**

E. Bilgilisoy, R. M. Thorman, M. S. Barclay, H. Marbach, D. H. Fairbrother

J. Phys. Chem. C, **2021,** *125*, 17749-17760

DOI: 10.1021/acs.jpcc.1c05826

Reprinted with permission from "The Journal of Physical Chemistry C". Copyright © 2021, American Chemical Society. Further permissions related to this article should be directed to the American Chemical Society.

[P3] **Nanoscale Ruthenium-Containing Deposits from $Ru(CO)_4I_2$ via Simultaneous Focused Electron Beam-Induced Deposition and Etching in Ultrahigh Vacuum: Mask Repair in Extreme Ultraviolet Lithography and Beyond**

E. Bilgilisoy, J. C. Yu, C. Preischl, L. McElwee-White, H.P. Steinrück, H. Marbach

ACS Appl. Nano Mater., **2022**, *5*, 3855-3865

DOI: 10.1021/acsanm.1c04481

Reprinted with permission from "ACS Applied Nano Materials". Copyright © 2022, American Chemical Society. Further permissions related to this article should be directed to the American Chemical Society.

[P4] On the Electron-Induced Reactions of $(CH_3)AuP(CH_3)_3$: A Combined UHV Surface Science and Gas-Phase Study

A. Kamali, E. Bilgilisoy, A. Wolfram, T. Gentner, G. Ballmann, S. Harder, H. Marbach, O. Ingólfsson

Nanomaterials, **2022**, *12*, 2727

DOI: 10.3390/nano12152727

This article is licensed under the terms and conditions of the Creative Commons Attribution (CC BY) license, visit: https://creativecommons.org/licenses/by/4.0/. Copyright © 2022 by the authors. Published by MDPI, Basel, Switzerland.